**ASDEX Contributions to the 19th European Conference on Controlled Fusion and Plasma Heating**
(Innsbruck, June 29 to July 3, 1992)

**ASDEX Contributions to the 10th PSI Conference,**
(Monterey, USA, March 30 to April 3, 1992)

IPP III/185

July 1992


**MAX-PLANCK-INSTITUT FÜR PLASMAPHYSIK**

**8046 GARCHING BEI MÜNCHEN**

**ASDEX Contributions to the 19th European Conference on Controlled Fusion and Plasma Heating**
(Innsbruck, June 29 to July 3)

**ASDEX Contributions to the 10th PSI Conference,**
(Monterey, USA, 30.3.-3.4.92)

CONTENTS

# CHARACTERISTIC FEATURES OF DENSITY FLUCTUATIONS ASSOCIATED WITH THE L-H-TRANSITION IN THE ASDEX TOKAMAK.

G. Dodel, E. Holzhauer, and the ASDEX-Team*

Institut für Plasmaforschung, Universität Stuttgart, Germany

*MPI für Plasmaphysik, EURATOM Association, Garching, Germany

## 1. INTRODUCTION

A far-infrared laser system was used to scatter from electron density fluctuations in the ASDEX tokamak [1]. Particular emphasis was placed on the L-H transition which is characterized by the establishment of a transport barrier close to the separatrix [2]. The difference in the behaviour of the fluctuations inside and outside this barrier was investigated. Another topic was the determination of plama rotation from the measured frequency and wavenumber spectra. A number of diagnostics measuring macroscopic plasma parameters was recorded with sampling rates up to 5 MHz to investigate a possible relationship with the density fluctuations.

## 2. CHANGES IN PLASMA PARAMETERS AT THE L-H-TRANSITION

To investigate the dependence of density flucutations on macroscopic plasma parameters we evaluated Li-beam measurements for the electron density profiles and ECE for the electron temperature. The transition into the H-phase usually occurs on a time scale of 100 μs. The sharp transition of the shoulder of the electron density profile to a steep gradient which marks the transport barrier is situated within a few mm at the separatrix position as determined from magnetic signals. There is experimental evidence that the true separatrix position is up to 1 cm further outwards. Outside the barrier both electron temperature and density drop to values comparable to or below those in the ohmic phase. The decay time of ≤ 100 μs for the parameters after the establishment of the transport barrier can be explained by diffusion radially and along open field lines to the walls of the vessel. A further build-up and broadening of the barrier region manifests itself by a rise in temperature and density on a ms timescale inside the separatrix. In many cases an oscillatory transition between the L- and H-mode is observed, the so-called "dithering H-mode".

Fig.1 shows the behaviour of the plasma density at two radial positions as obtained with the Li-beam for an L-H-transition and an ELM demonstrating the fast drop outside the transport barrier and the gradual increase inside [3].

Fig.2 shows the behaviour of the electron temperature as obtained from ECE for a position about 4 cm inside the separatrix for a sequence of two short H-modes demonstrating the continuous increase in $T_e$ inside the barrier after an H-transition.

## 3. FLUCTUATIONS IN THE BULK PLASMA AT THE TRANSITION

With the onset of NI the plasma in the L-phase starts to rotate in the toroidal direction. The corresponding frequency shift of the scattering signals is in the ion-diamagnetic direction for co-injection. In the dominant wavenumber range $k < 4$ cm$^{-1}$ these changes occur on the global momentum confinement timescale of several 10 ms. An attempt was made to measure the plasma velocity. In the bulk of the plasma drift waves are the most probable candidate for an instability. Linear theory predicts a decrease of the phase velocity with increasing wavenumber due to polarization drift and finite Larmour radius effects. Hence, for sufficiently high wavenumbers the propagation velocity of the fluctuations as measured in the laboratory frame should be dominated by the plasma velocity. Measurements were made in the equatorial channel at wavenumbers up to 10 cm$^{-1}$. The frequency shifts observed are as expected from the toroidal plasma rotation measured by spectroscopy [4]. Information on the radial position of the fluctuations could be inferred from temporal correlation with other diagnostics. For instance ELM precursor oscillations which are assumed to exist inside the transport barrier lead to a strong reduction of this frequency shift even if they do not trigger an ELM [5]. This supports the assumption that fluctuations with frequency spectra shifted towards the ion-diamagnetic side occur in the bulk of the plasma.

## 4. FLUCTUATIONS IN THE PLASMA BOUNDARY AT THE TRANSITION

Fluctuations coming from the separatrix region were localised in two ways:

- Using the outer vertical channel (which sees primarily radially propagating fluctuations).
- Using the equatorial channel (which sees primarily poloidally propagating fluctuations) and correlating the time dependence with macroscopic plasma parameters.

Contributions to the frequency spectra corresponding to the electron-diamagnetic drift direction which come from a region close to or outside the separatrix drop to a level comparable to or below the level in the ohmic phase. This drop occurs simultanously with the drop in density within the minimum time resolution determined by signal-to-noise considerations.

By shifting the plasma position inwards fluctuations outside of the separatrix could be measured using the outer vertical channel. Fig.3 shows the temporal development of the scattering signal power $P_S$ for a dithering H-transition together with the $D_\alpha$-monitor. One can see, that the level of fluctuations repeatedly drops back to "zero" (i.e. the noise level of the detection system) indicating the return of the barrier to an H-mode like state.

## 5. FLUCTUATIONS IN THE PLASMA BOUNDARY AFTER THE TRANSITION

A few ms after the transition a narrowband instability is observed to grow, which comes from the region at or outside the barrier and yields scattering signal powers above those in the L-phase. By suitable numerical filtering it can be also detected on a SX-channel (with the same distance from the plasma center as the vertical FIR channel), microwave reflectometry and the $D_\alpha$ signal in the divertor. It propagates in the electron diamagnetic direction. Its poloidal wavelength is estimated to be ≥10cm resulting in a propagation velocity in the laboratory frame of ≥ 6000 m/s for a frequency of 60 kHz. This instability does not lead to a dramatic increase of the $D_\alpha$ signal in the divertor. Taking into account the local electron pressure gradient (which yields the electron diamagnetic drift) and the toroidal plasma velocity the resulting frequency shift into the electron diamagnetic direction can only be explained by a poloidal rotation of the plasma due to a radial **E**-field as measured by spectroscopic methods [6]. Fig.4 shows the scattered power in the frequency band 55-65 kHz (electron diamagnetic direction). One can see a low power contribution in the L-mode, which disappears at the transition. For comparison, the scattered power in the frequency band 600 - 1000 kHz (ion diamagnetic direction) shows the continuous increase of the frequency shift after the L-H transition in the bulk plasma.

## 6. CONCLUSIONS

With the L-H transition a transport barrier is established inside the separatrix. We have separated the contributions to the scattering spectra coming from inside and outside this transport barrier. Outside the barrier the total fluctuation level as well as $T_e$ and $n_e$ drop to values comparable to or below the ohmic level on a 100 μs timescale whereas inside the barrier they change on a ms timescale. This behaviour is similar to observations reported on Doublet D-III-D. Evidence for poloidal plasma rotation close to the separatrix after the L-H-transition has been found from an instability with narrowband frequency spectra propagating in the electron-diamagnetic direction. In the bulk of the plasma the frequency shift is mainly in the ion diamagnetic direction due to toroidal plasma rotation.

## REFERENCES


[1] E. Holzhauer et al., Rev.Sci.Instrum. **61**, 2117 (1990)

[2] ASDEX-Team, "The H-mode of ASDEX", Nucl.Fus. **29**, 1959 (1989)

[3] K. McCormick et al., this conference

[4] A. Kallenbach et al., Nucl.Fus. **30**, 645 (1990)

[5] H. Zohm et al., Nucl.Fus. **32**, 489 (1992)

[6] A. Field et al., to be published in Nucl.Fus.

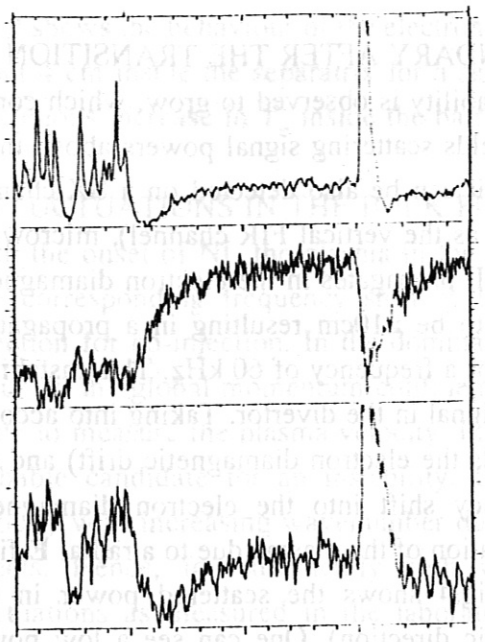

time window 20 ms

Fig.1: Top: $D_\alpha$ - monitor in the divertor chamber Middle: $n_e$ (Li-beam) inside barrier Bottom: $n_e$ (Li-beam) outside barrier

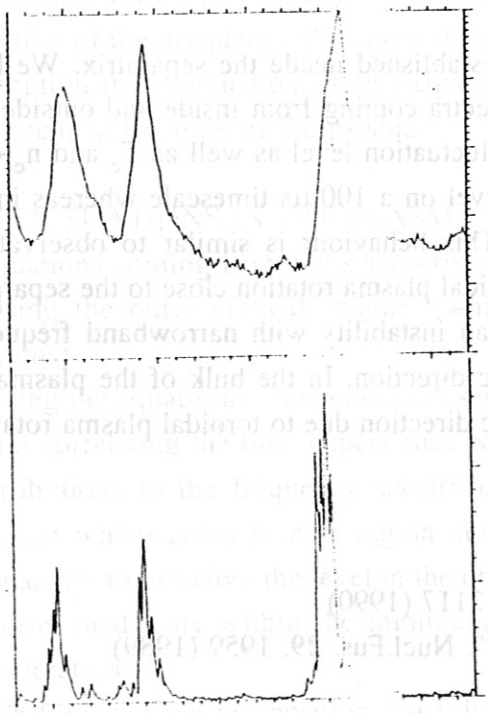

time window 2.5 ms

Fig.3: Top: $D_\alpha$ - monitor in the divertor chamber Bottom: $P_S$ outside separatrix (vertical channel, $\Delta B$=10-60 kHz)

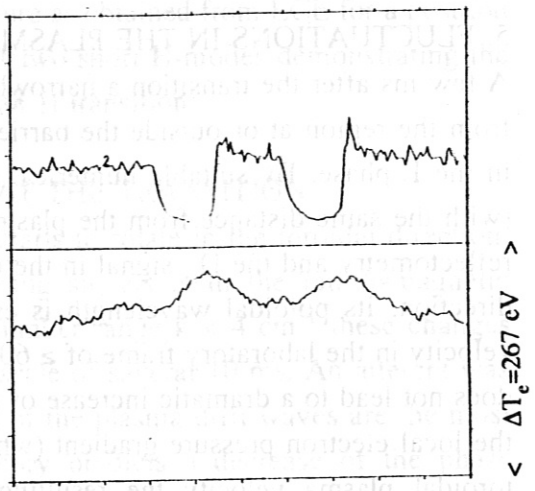


time window 10 ms

Fig.2: Top: $D_\alpha$ - monitor in the divertor chamber Bottom: $T_e$(ECE) inside barrier(sequence L-H-L-H-L)

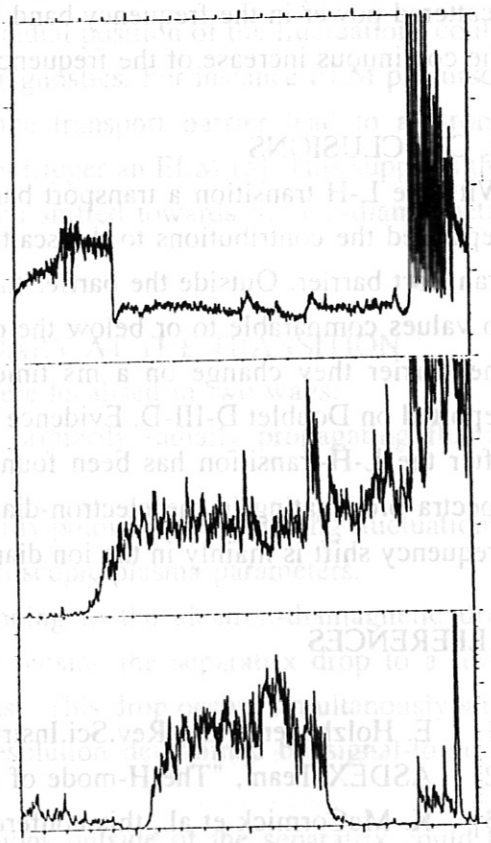

time window 200 ms

Fig.4: Top: $D_\alpha$ - monitor Middle: $P_S$ in the bulk plasma ($\Delta B$=600-1000 kHz, ion diamagnetic direction) Bottom: $P_S$ in the separatrix region ($\Delta B$=55-65 kHz,electron diamagnetic direction)

# CHANGE OF INTERNAL INDUCTANCE AND ANISOTROPY DURING LOWER HYBRID CURRENT DRIVE IN ASDEX

F. Leuterer, F.X. Söldner
Max-Planck Institut für Plasmaphysik, D-8046 Garching, Germany
R. Bartiromo
ENEA, Frascati, Italy
S. Bernabei
Plasma Physics Laboratory, Princeton, USA

## 1) Introduction

In lower hybrid experiments we observe sawtooth stabilisation, change in the MHD-modes etc., indicating a varying current profile j(r), /1,2/. The internal inductance $l_i$ gives an integral information about j(r) and is usually obtained from magnetic measurements, /3,4,5/, by subtracting $\beta_{dia}$ from ($\Lambda$ + 1), resulting in

$$D = (\Lambda + 1) - \beta_{dia} = (\beta_{par} - \beta_{perp}) + l_i/2. \qquad (1)$$

During low density current drive the anisotropy term ($\beta_{par} - \beta_{perp}$) is nonzero and positive. A change in the internal inductance is then very difficult to discriminate against the anisotropy term.

In experiments with feedback controlled constant plasma current $I_p$, the evaluation of the primary current rate of change, $d/dt(I_{oh})$, provides an independent method to determine changes in $l_i$. Any cause for a possible change of $I_p$, like noninductive current drive $I_{rf}$ or release of magnetic energy due to a change in $l_i$, leads to a variation of $d/dt(I_{oh})$ according to the circuit equation

$$M_{oh,p}\, d/dt(I_{oh}) = (I_p - I_{rf})\, R_p + 0.5\, I_p\, d/dtL_p. \qquad (2)$$

Here $M_{oh,p}$ is the mutual inductance between transformer coil and plasma, $R_p$ and $L_p$ are resistance and inductance of the plasma.

The results reported here were obtained with the ASDEX 2.45 GHz lower hybrid system /6/.

## 2) Example

In fig.1 we show a shot ($B_t$=2.8 T, $\overline{n_e}$=1.35 $10^{13}$ $cm^{-3}$, $I_p$=0.42 MA) where current drive with a low $N_{||}$ spectrum ($\Delta\phi$=75°, $N_{||}$=+1.8, $P_{75°}$ =0.695 MW) was applied from 1.0-1.8 sec, and from 1.4-1.8 sec additionally a symmetric high $N_{||}$ spectrum ($\Delta\phi$=180°, $N_{||}$=±4.4, $P_{180°}$ =0.23 MW). In the time interval 1.4-1.8 sec D is decreasing, indicating a decreasing $l_i$. Assuming that the high $N_{||}$ waves do not further change the anisotropy, i.e. $\Delta D = \Delta l_i$, we can calculate the related $d/dt(I_{oh})$. Its contribution to $U_{loop}$ is $M_{oh,u}\, d/dt(I_{oh})$ and is compared in fig.1(dashed line) with the experimental result (solid line). Unfortunately $I_{oh}$ was recorded only with a sampling rate of 5 msec, so we had to integrate over 15 msec for the calculation of $d/dt(I_{oh})$. But we still find good agreement.

The positive $\Delta D$ during 1.0-1.4 sec, however, is not due to an increasing $l_i$. It is caused by increasing anisotropy ($\beta_{par} - \beta_{perp}$) because of the high energy electrons resonant with the low $N_{||}$ waves. To show this, we compare the time variations of D and of $M_{oh,u}\, d/dt(I_{oh})$. In fig.1 we have $U_{loop} \approx 0$, thus a change in $R_p$ does not contribute to equ.2. The variation of

$M_{oh,u}$ d/dt($I_{oh}$) then reflects a change of $l_i$ only. The experimental $M_{oh,u}$ d/dt($I_{oh}$) indicates a small drop in $l_i$ although $\Delta D$ is positive. If the $\Delta D$ would correspond to a positive $\Delta l_i$, then $M_{oh,u}$ d/dt($I_{oh}$) should follow the dashed-dotted line in fig.1, which is not the case. This means that the positive $\Delta D$ in the first time interval is mostly due to anisotropy. Estimating the small drop in $l_i$ from $M_{oh,u}$ d/dt($I_{oh}$), $\Delta l_{i,75°} \approx -0.07$, we can calculate the anisotropy, which is about 30% larger than $\Delta D$ (dotted line in fig.1).

3) $L_i$-variations with combined spectra

The deposition of low $N_{||}$ current drive power is shifted radially by the additional high $N_{||}$ power,/1/. The related drop in $l_i$, $\Delta l_{i,180°} \approx \Delta D$, depends on the high $N_{||}$ power level $P_{180°}$ as shown in fig.2 ($B_t$=2.8 T, $\overline{n_e}$=1.35 $10^{13}$ $cm^{-3}$, $I_p$=0.42 MA). Note that this $\Delta l_{i,180°}$ is additional to the small $\Delta l_{i,75°}$ occuring already during the first time interval where only low $N_{||}$ power is applied as described in fig.1.

We also get a change of $\Delta l_i$ varying the high $N_{||}$ at constant high $N_{||}$ power, as shown in fig.3 ($B_t$=2.2 T, $\overline{n_e}$=1.35 $10^{13}$ $cm^{-3}$, $I_p$=0.42 MA). Here high $N_{||}$ power, $P_{\Delta\phi}$ =180 kW (different $\Delta\phi$), is applied from t = 1.2-2.2 sec, while low $N_{||}$ power, $P_{90°}$ =780 kW, is applied from 1.7-2.7 sec. Initially the low $P_{\Delta\phi}$ produces only a negligable change in $l_i$ as seen in the $M_{oh,u}$ d/dt($I_{oh}$) curves. However, as soon as the 90° power is added, we see a remarkable drop in $l_i$, which is stronger for higher values of $N_{||}$ of the high $N_{||}$ spectrum. At t=2.2 sec $P_{\Delta\phi}$ is switched off and the strong drop in $l_i$, occuring at t=1.7 sec, is now reversed as seen in the $M_{oh,u}$ d/dt($I_{oh}$) curves. The magnitude of $\Delta D$, however, is quite different in the time intervals 1.7-2.2 sec and 2.2-2.7 sec, the reason being the anisotropy part of $\Delta D$. From 2.2-2.7 sec we find $\Delta D \approx \Delta l_i$ as determined from $M_{oh,u}$ d/dt($I_{oh}$), i.e. the anisotropy does not change. But from 1.7-2.2 sec, the anisotropy is changed by switching on $P_{90°}$. Calculating $\Delta l_i$ from $M_{oh,u}$ d/dt($I_{oh}$) and adding it to $\Delta D$, we get the anisotropy as shown in the dotted line of the 180° curve in fig.3. We note that the time constant for establishing the anisotropy is comparable to that for $l_i$ changes. When $P_{90°}$ is also switched off at t=2.7 sec we see no further change in $l_i$ in the $M_{oh,u}$ d/dt($I_{oh}$) curves, indicating that the $l_i$ during 90° current drive at this power level is the same as during inductive current drive. The anisotropy part in $\Delta D$, however, is dieing away.

4) $L_i$ variations with narrow spectra

A single narrow spectrum can also lead to a change in $l_i$, depending on $N_{||}$. In fig.4 ($B_t$=2.2 T, $\overline{n_e}$=1.35 $10^{13}$$cm^{-3}$, $I_p$=0.32 MA) we show a series of shots with different $\Delta\phi$, but constant incident power P=900 kW. The D signals give positive $\Delta D$ for $\Delta\phi$=90°-120°, and only for $\Delta\phi$=135°-180° we get negative $\Delta D$, indicating a drop of $l_i$. The curves $M_{oh,u}$ d/dt($I_{oh}$) show that $\Delta l_i \approx 0$ for $\Delta\phi$=90°-120°, so that the positive $\Delta D$´s indicate primarily a change in anisotropy, as in the example described in fig.1. Only for the phase settings $\Delta\phi$=135°-180° we find from the $M_{oh,u}$ d/dt($I_{oh}$) curves a negative $\Delta l_i$ , compatible with the negative $\Delta D$. We conclude that at this power level spectra with $\Delta\phi$>120° have a power deposition, which is shifted radially outward, the shift increasing with $N_{||}$.

The changes in anisotropy and in inductance depend also on the rf power. Two extreme cases, high $N_{||}$ ($\Delta\phi$=180°) symmetric spectrum and low $N_{||}$ ($\Delta\phi$=75°) current drive spectrum, are

shown in figs.5 and 6, where we plot $\Delta\beta_{dia}$ and $\Delta(\Lambda+1)$. In the high $N_{||}$ case we find both $\Delta\beta_{dia}$ and $\Delta(\Lambda+1)$ about proportional to $P_{rf}$, although with different sign. The change in $l_i$, estimated from $M_{oh,u}\ d/dt(I_{oh})$ and shown as crosses in the figures, is found compatible with $\Delta D = \Delta(\Lambda+1-\beta_{dia}) \approx \Delta l_i$, suggesting negligable anisotropy in the high $N_{||}$ case. The low $N_{||}$ case is quite different. Contrary to $\Delta\beta_{dia}$, we find $\Delta(\Lambda+1)$ not proportional to $P_{rf}$,/7/. Even at low power $\Delta(\Lambda+1)$ is already quite large due to the anisotropy, which is strong in the low $N_{||}$ case, and which is further enhanced at low power by the still appreciable electric field, leading eventually to runaway production /6/. In addition $M_{oh,u}\ d/dt(I_{oh})$ indicates that at low power $\Delta l_i$ might be slightly positive, whereas at high power it becomes negative,/8/. Thus the anisotropy is somewhat lower than $\Delta D$ at low power, but higher than $\Delta D$ at high power.

This experiment was performed in collaboration between IPP-Garching, ENEA-Frascati and PPPL-Princeton.

References

/1/ F.X. Söldner et al., 13. IAEA-Conf. on Plasma Physics and Contr. Nuclear Fusion Research, Washington 1990, Vol.1, 613, (1990)

/ 2 / K. McCormick et al., Phys. Rev. Lett. 58, 491, ( 1987 )

/ 3 / D. Van Houtte et al., Nucl. Fusion 24, 1485, (1994)

/ 4 / K. Ushigusa et al., Nucl. Fusion 29, 1052, (1989)

/ 5 / F. Leuterer et al., 13. Europ. Conf. Contr. Fusion + Plasma Physics, Schliersee 1986, Europhys. Conf. Abstr., Vol.10C/II, 409, (1986)

/ 6 / F. Leuterer et al., Nucl. Fusion 31, 2315, (1991)

/ 7 / R. Bartiromo et al.,17. Europ. Conf. Contr. Fusion + Plasma Physics, Amsterdam1990, Europhys. Conf. Abstr., Vol.14B/III, 1092, (1990)

/ 8 / F.X. Söldner et al.,14. Europ. Conf. Contr. Fusion + Plasma Physics, Madrid 1987, Europhys. Conf. Abstr., Vol.11D/III, 831, (1987)

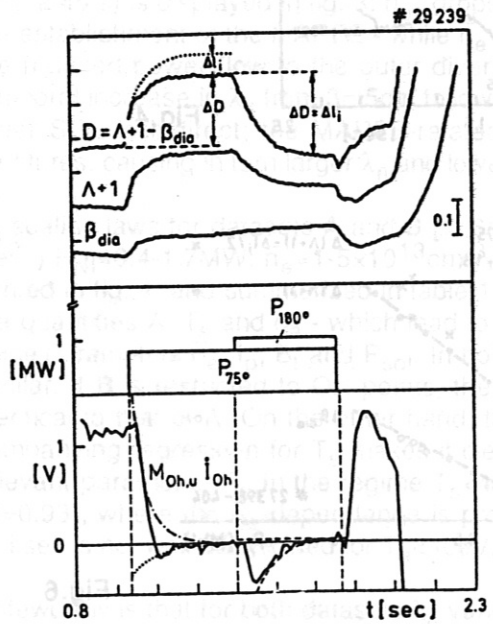


Fig.1

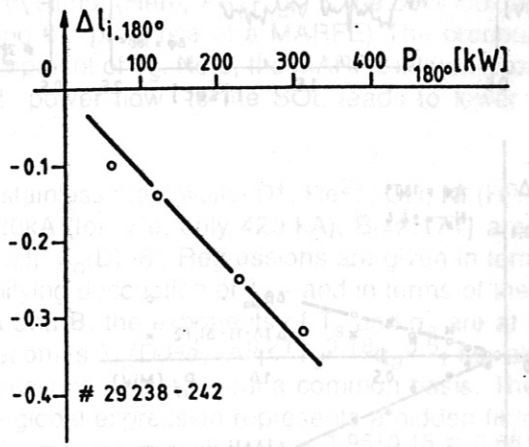


Fig.2

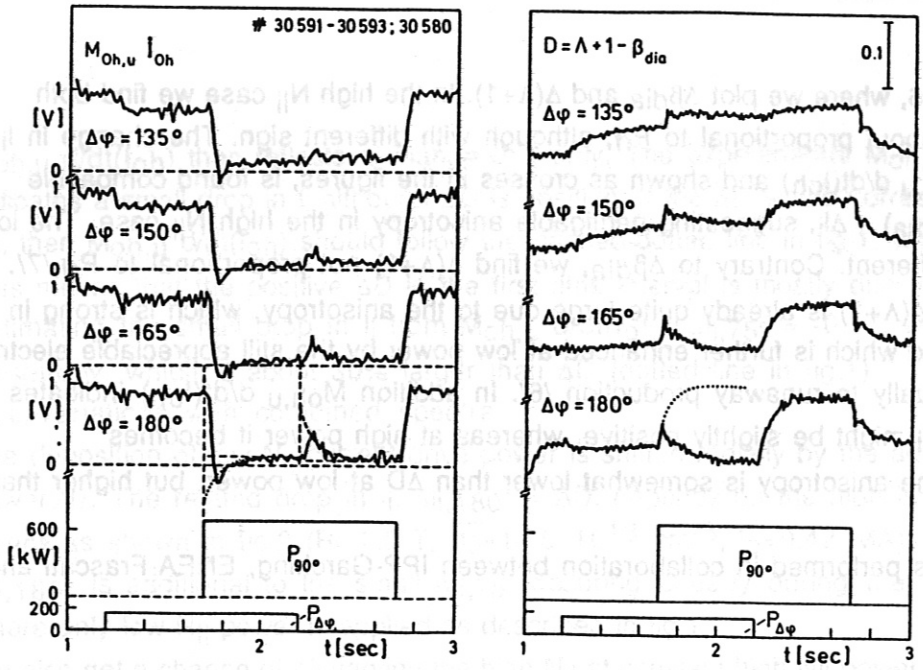


Fig.3

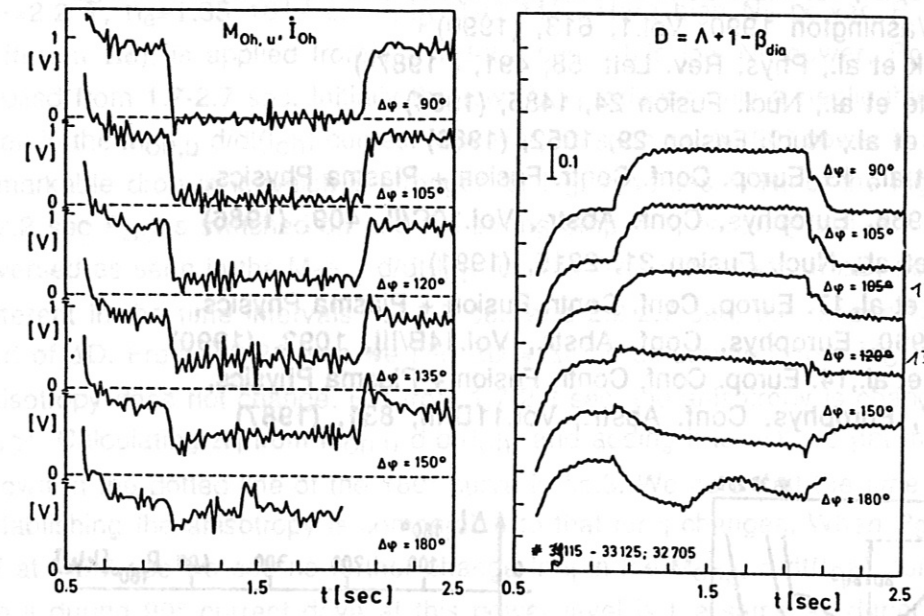


Fig.4

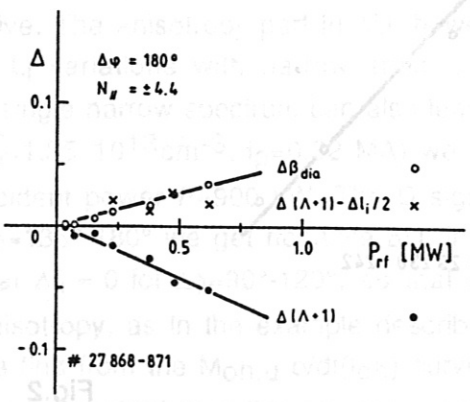


Fig.5

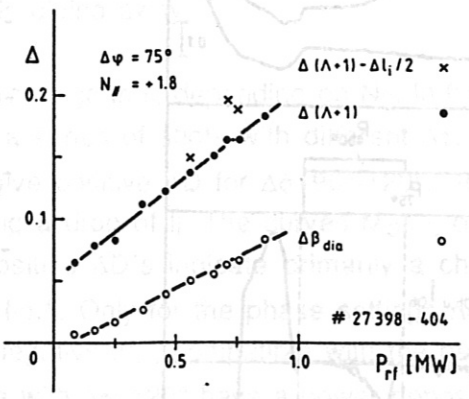


Fig.6

# A Study of the SOL Density Profile Behavior in ASDEX

**K. McCormick, J. Schweinzer, and Z.A. Pietrzyk***
**Max-Planck-Institut für Plasmaphysik, 8046 Garching, Germany**
***CRPP, Lausanne, Switzerland**

**Introduction:** Scrape-off layer (SOL) density profiles measured in the outer midplane of ASDEX by the lithium beam probe diagnostic have been presented in the past /1-8/. This work places these results on a common basis for OH and NI-heated discharges (L-mode), and suggests a scaling for the particle diffusion coefficient $D_p$ which is derived using $\lambda_n$, the exponential fall-off length in the SOL near the separatrix. Density profiles for the H-mode have now also been extended to inside the separatrix.

**Characterization of the SOL Density Profile:** Only data from the steady-state phase of double-null (DN), diverted discharges fueled by gas puffing are discussed in detail. While no systematic evaluation of the single-null (SN) configuration has been carried out to date, the indications are there is little difference between DN and SN. Pellet-fueled discharges, as well as discharges exhibiting Improved Ohmic Confinement (IOC) /6,7/ influence the separatrix density $n_{es}$, but $\lambda_n$ is essentially not affected.

Fig. 1 depicts $\lambda_n$ values vs. electron temperature slightly inside the separatrix $T_s$ /8/ for dataset **A** (divertor configuration DV II /7/, both divertor bypasses open /7/, carbonized walls; $H^+$, $D^+$; OH; $\bar{n}_{e13}$= 0.8-5.5×$10^{13}$cm$^{-3}$, $I_p$=150-420kA, $B_t$=1.9-2.55T /6/. For $T_s$>40eV, the points scatter about a line roughly given by $\lambda_n$~1.9cm, but for $T_s$<40eV there is a dramatic increase in $\lambda_n$ with decreasing $T_s$. This is in the regime (low $T_s$, $q_a \geq 5$) favorable to the formation of MARFES. Early $\lambda_n$-scalings for ASDEX indicated a $q_a$-dependence /4/, but for dataset **A** as an entity this approach was not appropriate /6/ due to the presence of the two different regimes. The behavior of $\lambda_n$ as a function of $q_a$ for a small density window, $\bar{n}_{e13}$=1.5-1.75, is illustrated in fig. 2: As $q_a$ is increased through variation of $I_p$ and $B_t$, the power flow $P_{sol}$ into the SOL falls with $I_p$, as does the edge temperature $T_s$ and density $n_{es}$ /7/. (Note, the high colinearity of $T_s$ with $I_p$, and thus $q_a$, makes it impossible to derive any scaling involving both $T_s$ and $q_a$ for this subset - in marked contrast to the entire dataset.) Of interest is that $D_p$ (discussed below) initially falls with $q_a$ and then increases for $q_a \geq 5$, directly mirroring the behavior of $T_s$ and $q_a$.

The dynamic evolution of $\lambda_n$, $T_s$ and $n_{es}$ as a MARFE is provoked by ramping $\bar{n}_e$ until disruption occurs (at t~2.45 s) is displayed in fig. 3: $n_{es}$ drops by 30% and then stabilizes on a time scale correlated with the establishment of the MARFE - while $\bar{n}_e$ continues to climb. (Here, $P_{RAD,div}$ is the best indicator of the reduced power flow to the outer divertor, signaling the presence of a MARFE) The pronounced temporal increase in $\lambda_n$ from 3→5cm follows the development of $T_s$. Note, the MARFE influence on the outer SOL is indirect: the MARFE-related, reduced power flow to the SOL leads to lower temperatures, causing in turn larger $\lambda_n$ and lower $n_{es}$.

$\lambda_n$ scaling laws for datasets **A** and **B** [/3,6/: DV I /7/, stainless steel walls: $D^+$, $He^{2+}$; OH, NI ($H^o \rightarrow D^+$, $He^{2+}$) $P_{NI}$=0.4-1.7MW; $\bar{n}_e$=1-5×$10^{13}$cm$^{-3}$, $I_p$=270-420kA (for He, only 420 kA), $B_t$=2.17T] are presented in fig. 4, and summarized in table 1. For **A**, $\lambda_n(H) \sim \lambda_n(D)$ /8/. Regressions are given in terms of the quantities A, $T_s$ and $q_a$ - which lead to a more unifying description of $\lambda_n$ - and in terms of the machine parameters $\bar{n}_e$, $I_p$, $B_t$ and $P_{sol}$. In both cases **A** and **B**, the exponents of $T_s$ and $q_a$ are at least similar. If **B** is restricted to OH points, the scaling becomes $\lambda_n(D,He) \sim A^{0.21} T_s^{0.18} q_a^{0.6}$, i.e. almost identical to that of **A.** On the other hand, the global scalings do not reveal a common basis. The accompanying regression for $T_s$ makes it clear that the global expression represents a hidden fit to the relevant parameter $T_s$. In the regime $T_s$<40eV of **A**, $\lambda_n$ may be described as $q_a^{1.96\pm0.16}\, \bar{n}_e^{0.66\pm0.09}$ (R=0.93), where the $\bar{n}_e$-dependence is probably a hidden $T_e$-dependence in the sense $T_e \sim n_e^{-1}$ /7/; $T_s$ itself is not well determined for $T_e$<40eV.

Noteworthy is that for both datasets $\lambda_n$ varies only over the range 1.6-2.7cm, for $T_s$>40eV. The experimental systematic uncertainty associated with $\lambda_n$ is about ±1mm, corresponding closely to the vertical spread of points in fig. 4.

**Diffusion Coefficients:** An estimate of the diffusion coefficient may be attained from $D_p = \lambda_n^2 v_{||}/L_c = \lambda_n^2 f_{||} C_s/L_c = \lambda_n^2 f_{||} (eT_s(\gamma_i + Z_i\gamma_e)/m_i)^{0.5}/L_c$, predicating a source-free SOL, no inward drift, no influence of electric fields, $T_e = T_i$, only one ion species with charge $Z_i$, and a global streaming velocity $v_{||} = f_{||} C_s$ (averaged over the midplane/divertor plate distance of $L_c = q_a L_o$; $L_o = 3.33$m) where $C_s$ is the sound speed. Below, $\gamma_i = \gamma_e = 1$ is taken.

From the approximate relationship $\lambda_n \sim q_a^{0.5} T_s^{0.25}$ of table 1, $D_p$ would be expected to scale as $T_s$. This is confirmed in fig. 5, where $D_p/f_{||}$ is plotted vs. $T_s$, showing a uniformly linear increase of $D_p/f_{||}$ for both datasets. ($D_p/f_{||}$ is taken, since $f_{||}$ may contain dependencies, intermingling with those of $D_p$, to give the regressions in table 1.) In **A** the scaling is $D_p/f_{||} \sim q_a^{-0.18} T_s^{1.00}$, and for **B** we have $D_p/f_{||} \sim A^{0.19} T_s^{1.02} q_a^{0.68} P_{sol}^{0.22}$. In both cases, $T_s$ is the predominant factor as expected from fig. 5, but the $q_a$ exponents are substantially different. One might speculate that this represents different $f_{||}$-regressions coming about as a result of NI, or simply that some aspect of the model is not being fulfilled.

The $T_e$-dependence of $D_p/f_{||}$ is reminiscent of Bohm diffusion since $D_{Bohm} = T_e/16B_t$. Code calculations carried out over a wide range of ASDEX conditions (not $q_a$) and calibrated against experimentally observable quantities gave $f_{||} = 0.3$ as a good description /9/. Assuming $f_{||} = 0.3$ for these datasets yields $D_p \sim 1/3 - 1/2\ D_{Bohm}$ for the range $T_s > 40$eV.

**H-Mode Density Profiles:** The behavior of the SOL $n_e(r)$ profile during the H-mode has been addressed previously /1,5/, but now the data have been extended to inside the separatrix by virtue of an improved algorithm for reconstructing the density profile from the lithium beam probe data /10,11/. Fig. 6(a) illustrates that the steep density gradient typical of the H-phase continues for a few mm inside the magnetically-determined separatrix, and only then makes the transition into a much flatter shoulder. Fig. 6b depicts the relaxation of the density profile after an ELM. Important is that the density gradient transition region is again within the separatrix, and has fully restablished itself while the SOL density perturbation associated with the ELM is still relaxing. More on the temporal processes during the L-H transition is contained in /12/.

**Discussion and Conclusions:** $\lambda_n$ has been shown to vary about as $T_s^{0.25} q_a^{0.5}$ for OH discharges, when $T_s > 40$eV. This is in accordance with that expected from connection length arguments within the framework of a simple 1-D SOL model where $D_p$ scales as $T_s$. The emergence of a stronger $q_a$-scaling, along with a weak $P_{sol}$-scaling for the NI-heated dataset **B** might be a direct consequence of variations of $f_{||}$ with these parameters. Presently, there is no indication that $D_p$ exhibits a toroidal field component, and hence is not Bohm-like even though $D_p \sim D_{Bohm}$. Nevertheless, the possibility cannot be excluded, until further code work has been performed, that $f_{||}$ scales such as to nullify an explicit $B_t$ dependence of $D_p/f_{||}$. Then again, the fact that $D_p(D^+)$ varies in a more-or-less continuous fashion from one dataset to another, where the divertor configuration and wall conditioning techniques were changed, indirectly supports the code result /9/ that $f_{||}$ does not underlie strong modifications.

The implied scaling of $D_p$ with $T_s$ is not meant to be taken locally; rather, $T_s$ is to be regarded as a temperature which characterizes the entire SOL. A local variation of $D_p$ with $T_e$ would lead to profile forms inconsistent with those observed. In particular, for $R\text{-}R_s > 2$cm a shoulder in the $n_e(r)$ profile often appears /5,6,8/, suggesting an augmentation of $D_p$ (if $f_{||}$=const.) instead of a reduction as would be predicted by a $D_p \sim T_e(r)$ scaling (since $T_e$ decreases strongly with r). Phenomenologically, the density profile behavior for $R\text{-}R_s > 2$cm bears resemblence to the region $T_s < 40$ev of fig.1, leading one to speculate if the underlying physics is of the same nature.

For the H-mode the transition region from a steep to a flat gradient is found to be slightly within the separatrix for a very early divertor configuration of ASDEX. Analysis of discharges taken in the last month of ASDEX operation (not shown here) actually determines the break point to lie a few mm to the outside. Considering that experiments to localize the separatrix position (albeit at a toroidal position different from that of the Li-beam) consistently show the true separatrix to lie about one cm outside the separatrix derived by magnetics, it is probable that the density gradient transition point occurs within the separatrix in all cases.

## References

/1/ K. McCormick, H. Murmann, M. El Shaer, J. Nucl. Mater. **121** (1984) 48
/2/ K. McCormick, et al., Rev. Sci. Instrum. **56** (1985) 1063
/3/ K. McCormick, Z.A. Pietrzyk, et al., Proc. 14th EPS Conf. Madrid **11d** (1987) 666
/4/ K. McCormick, Z.A. Pietrzyk, et al., J. Nucl. Mater. **145-147** (1987) 215
/5/ G.K. McCormick, Z.A. Pietrzyk, et al., J. Nucl. Mater. **162-164** (1989) 264
/6/ K. McCormick, Z.A. Pietrzyk, et al., Proc. 16th EPS Conf. Venice **13B** (1989) 895
/7/ K. McCormick, et al., J. Nucl. Mater. **176&177** (1990) 89
/8/ K. McCormick, G. Kyriakakis, et al., 10th PSI Conf., to be pub. in J. of Nucl. Mater.
/9/ W. Schneider, J. Neuhauser, et al., Contrib. Plasma Phys. **28** (1988) 387
/10/ J. Schweinzer, K. McCormick, S. Fiedler, et al., this conference
/11/ J. Schweinzer, E. Wolfrum, F. Aumayr, et al., Plasma Phys. Contr. Fusion (1992) in print
/12/ D. Dodel, H. Holzhauer, et al., "Characteristic Features of Density Fluctuations...", this conf.


| | case | const. | A | | ñe13 | | Ip | | Bt | | Psol | | qa | | Ts | | R |
|---|---|---|---|---|---|---|---|---|---|---|---|---|---|---|---|---|---|
| lam | A | 7.32 | | | | | -0.45 | 0.03 | 0.44 | 0.04 | | | | | 0.23 | 0.02 | 0.88 |
| lam | A | 3.91 | | | -0.15 | 0.01 | -0.15 | 0.02 | 0.42 | 0.04 | | | | | | | 0.9 |
| Ts | A | 0.105 | | | -0.58 | 0.02 | 1.2 | 0.04 | 0 | 0 | | | | | | | 0.96 |
| Dp/fll | A | 0.048 | | | | | | | | | | | -0.18 | 0.04 | 1.01 | 0.04 | 0.95 |
| lam | B | 74.7 | 0.2 | 0.03 | | | -0.83 | 0.08 | | | 0.12 | 0.02 | | | 0.25 | 0.04 | 0.91 |
| lam | B | 50.1 | 0.26 | 0.03 | -0.13 | 0.02 | -0.54 | 0.07 | | | 0.14 | 0.02 | | | | | 0.91 |
| Ts | B | 0.2 | 0.24 | 0.04 | -0.51 | 0.03 | 1.17 | 0.1 | | | 0.1 | 0.03 | | | | | 0.97 |
| Dp/fll | B | 0.018 | 0.19 | 0.06 | | | | | | | 0.22 | 0.05 | 0.68 | 0.15 | 1.02 | 0.08 | 0.97 |

**Table 1** Exponents for regression fits of the form: const.x $A^{\alpha} n_e^{\beta}$... $\lambda_n$[cm], $D_p/f_{ll}$[$m^2$/s], A[ion mass], $\bar{n}_e$[$10^{13}$ $cm^{-3}$], $I_p$[kA], $B_t$[T], $P_{sol}$[MW], $T_s$[eV]. Standard error is in the adjacent column. R is the regression coefficient. Blank spaces indicate that the parameter was not included in the regression.

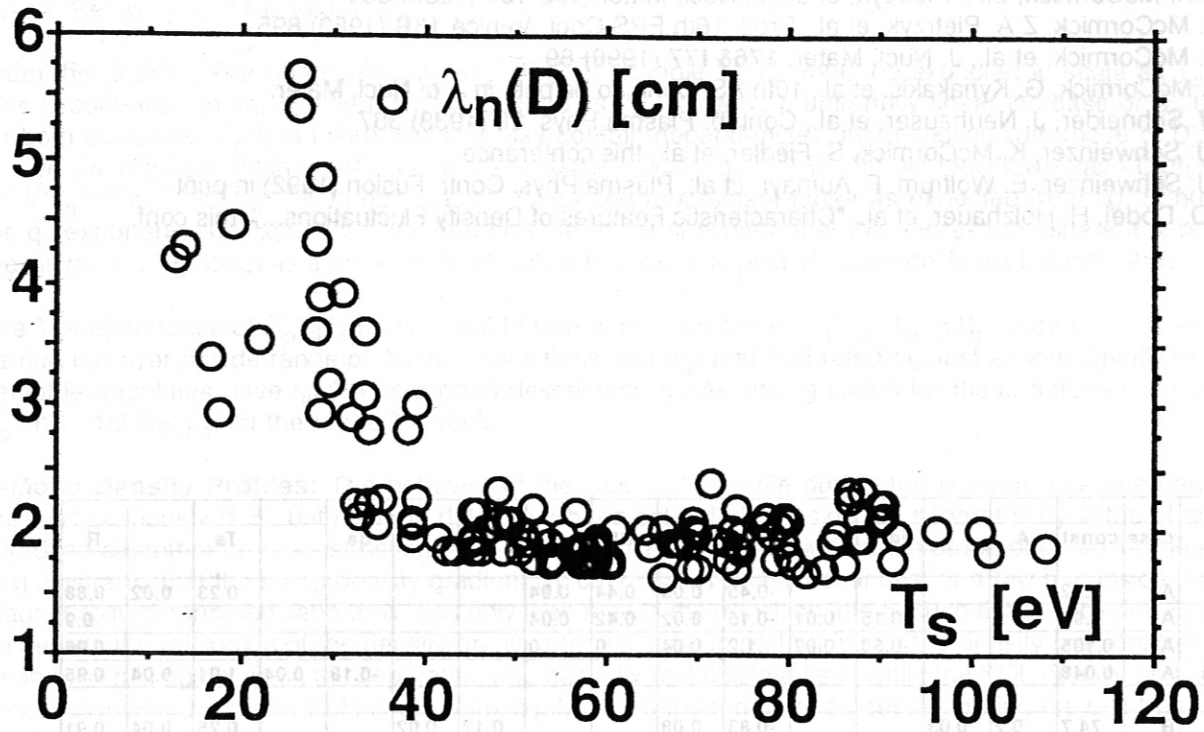


**Fig.1** SOL density falloff lengths for case **A**. Only $D^+$ is shown, but $\lambda_n(D) \sim \lambda_n(H)$.

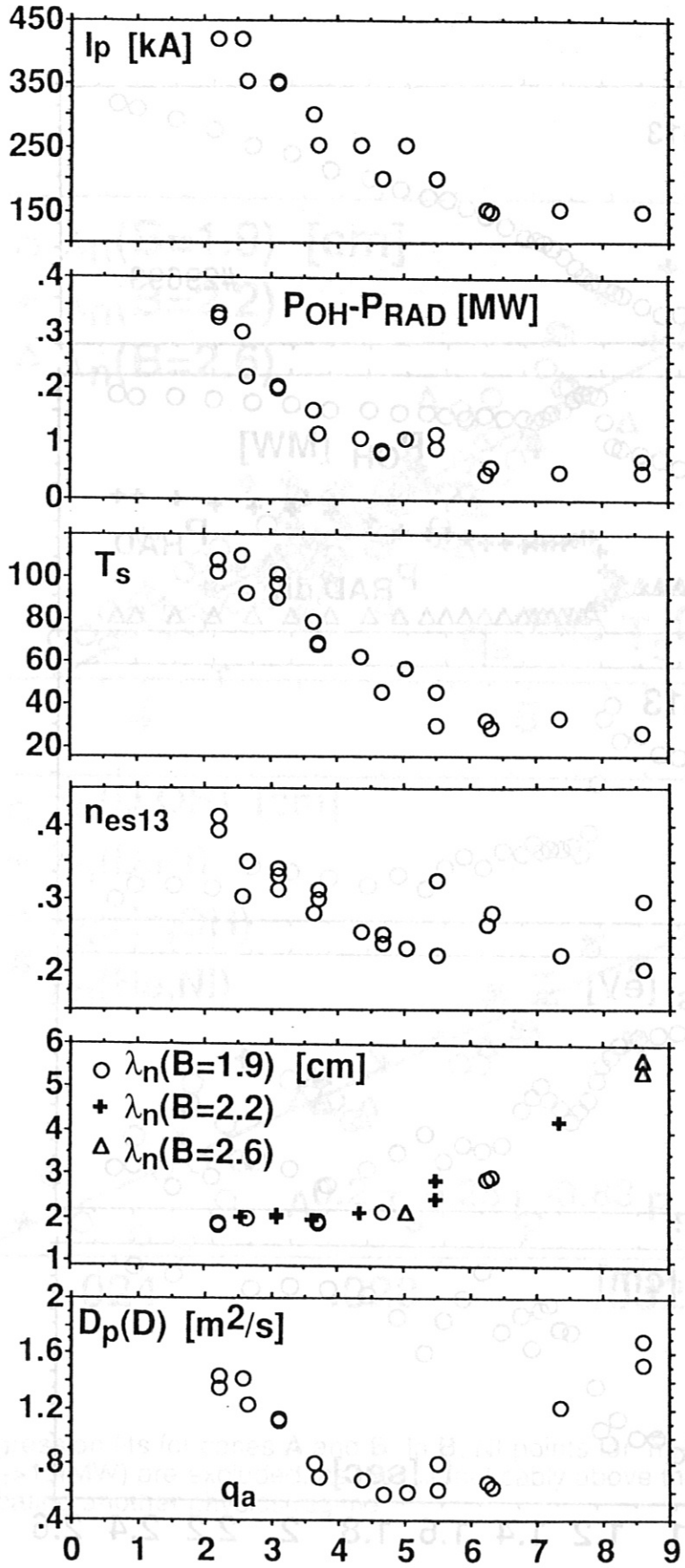


**Fig.2** Variation of characteristic global and edge parameters vs. $q_a$ for $\bar{n}_{e13}$=1.5-1.75, $D^+$.

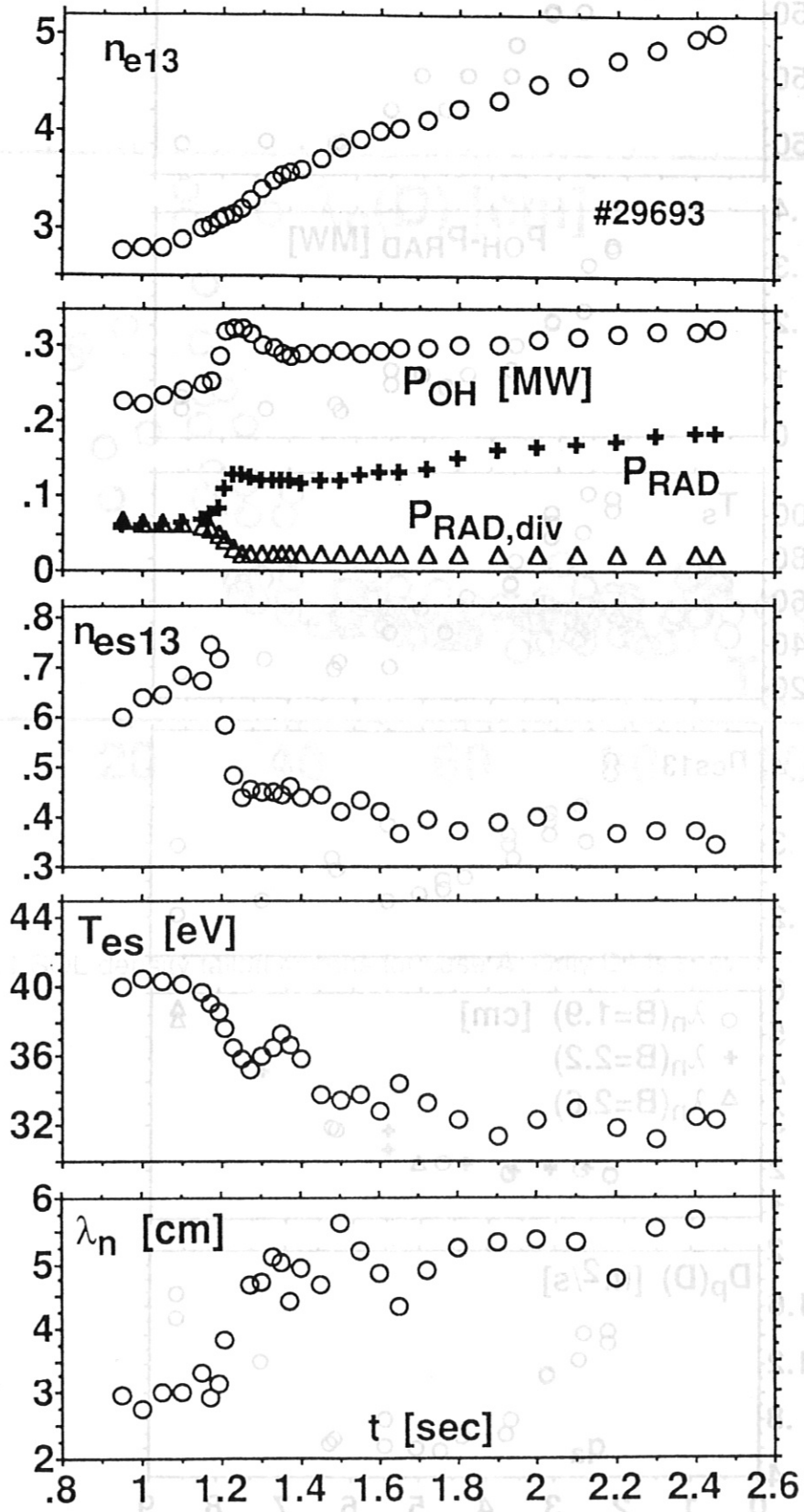


**Fig.3** Time behavior of global and edge parameters during an $n_e$-ramp, which triggers a MARFE at t~1.17 s. $q_a$=5.9

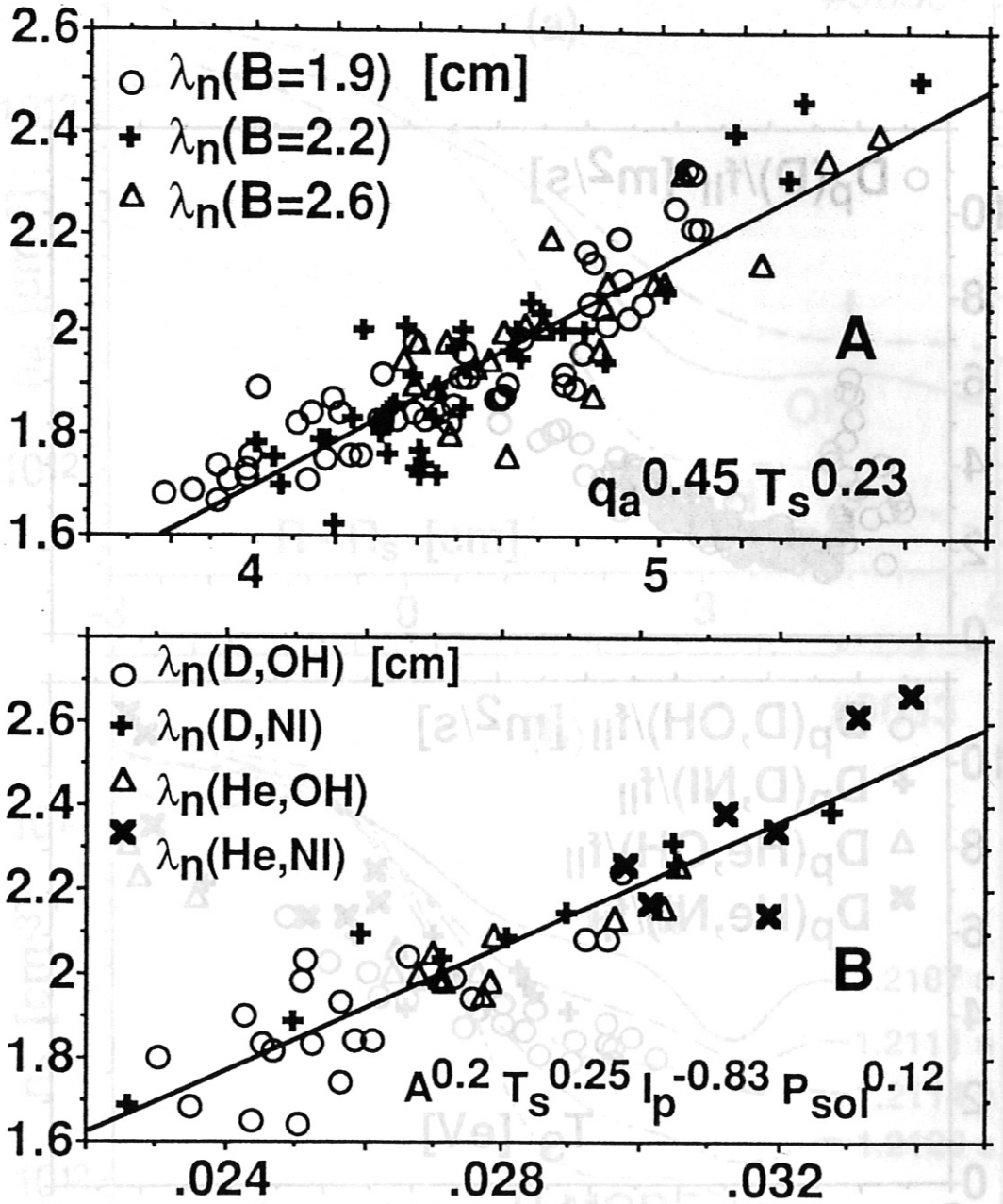


**Fig.4** $\lambda_n$ regression fits for cases **A** and **B**. In **B**, NI-points for $\bar{n}_{e13}<1$, $P_{sol}\geq 1$MW ($P_{tot}>1.4$MW) are excluded, as they lie noticably above the others, possibly indicating another physics regime.

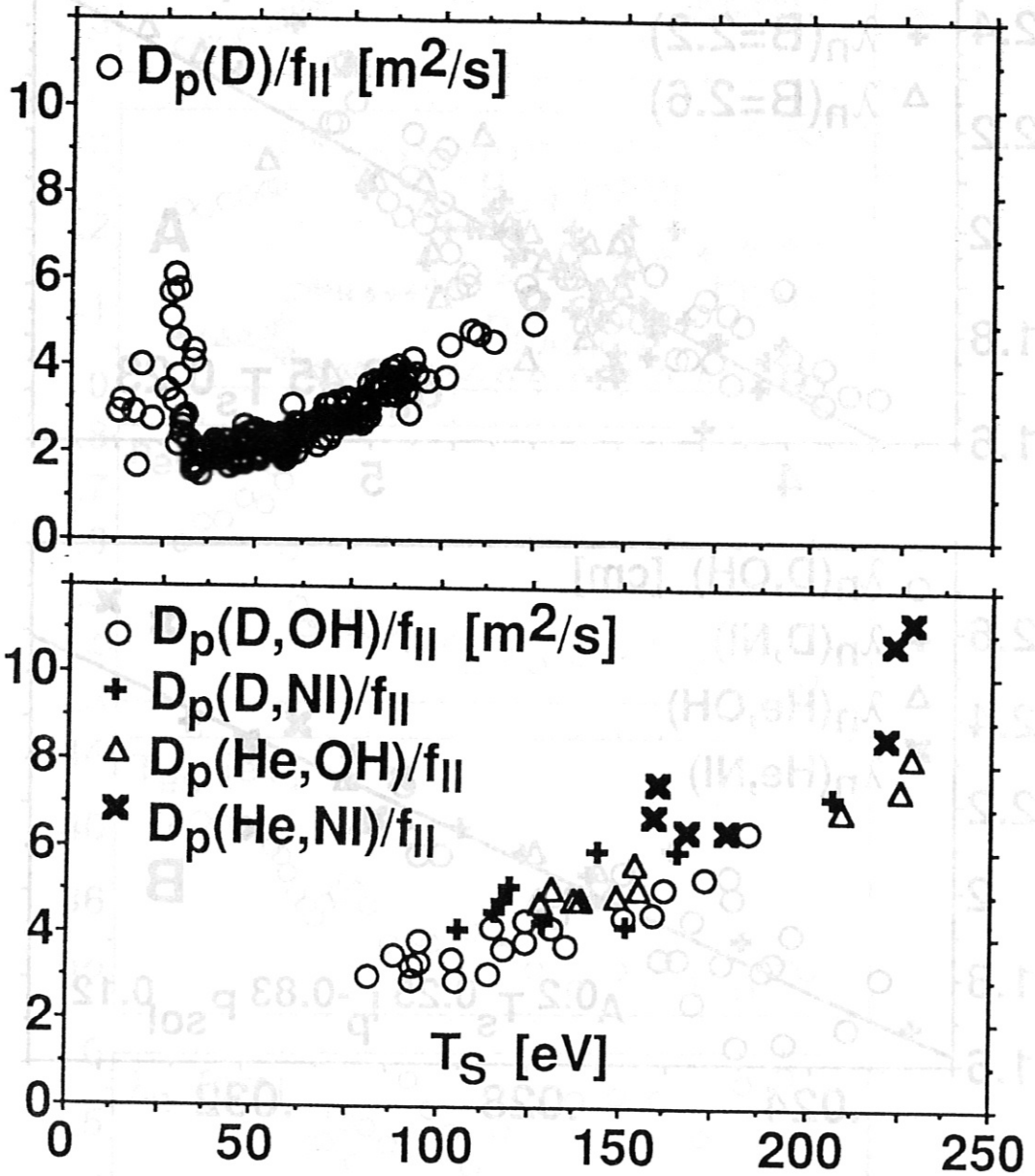


**Fig.5** $D_p/f_{II}$ for **A** and **B**. The (He,NI) points lying above the major grouping are for the lowest density ($\bar{n}_e$=2) and higher power ($P_{sol}$~0.9MW) of this subset.

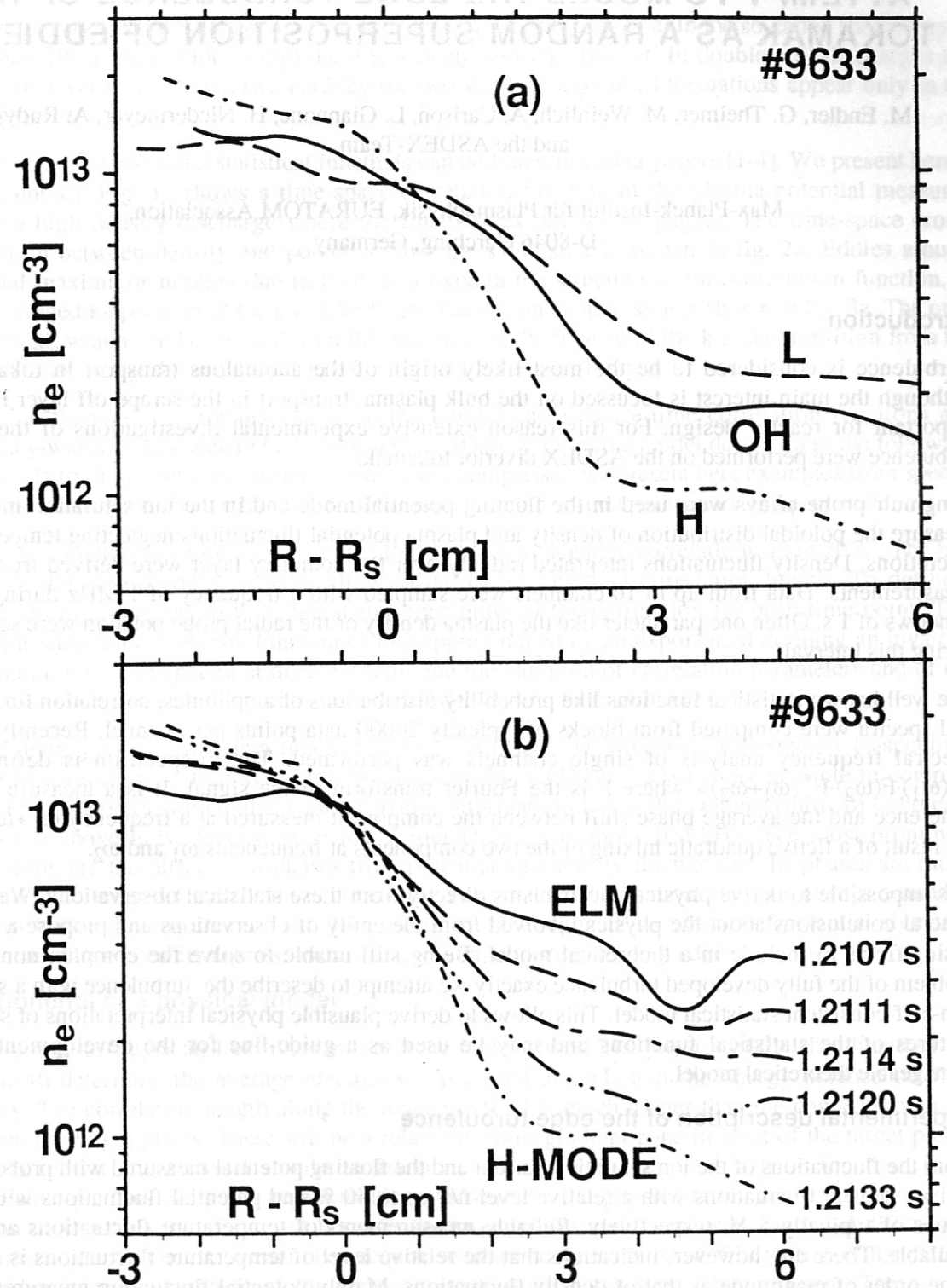


**Fig.6** Edge/SOL $n_e$-profiles: $B_t$=2.17T, $\bar{n}_{e13}$~4, $I_p$=315kA, $P_{NI}(H^o \rightarrow D^+)$2.8MW.
(a): steady-state OH-, L-, H-phases,
(b): during decay phase of ELM.
sample freq.=10kHz, cutoff freq.=4kHz.

# ATTEMPT TO MODEL THE EDGE TURBULENCE OF A TOKAMAK AS A RANDOM SUPERPOSITION OF EDDIES

M. Endler, G. Theimer, M. Weinlich, A. Carlson, L. Giannone, H. Niedermeyer, A. Rudyj
and the ASDEX-Team

Max-Planck-Institut für Plasmaphysik, EURATOM Association,
D-8046 Garching, Germany

## Introduction

Turbulence is considered to be the most likely origin of the anomalous transport in tokamaks. Although the main interest is focussed on the bulk plasma, transport in the scrape-off layer is very important for reactor design. For this reason extensive experimental investigations of the edge turbulence were performed on the ASDEX divertor tokamak.

Langmuir probe arrays were used in the floating potential mode and in the ion saturation mode to measure the poloidal distribution of density and plasma potential fluctuations neglecting temperature fluctutions. Density fluctuations integrated radially over the boundary layer were derived from $H_\alpha$-measurements. Data from up to 16 channels were sampled with a frequency of 1 MHz during time windows of 1 s. Often one parameter like the plasma density or the radial probe position were scanned during this interval.

The well known statistical functions like probability distributions of amplitudes, correlation functions and spectra were computed from blocks of typically 20000 data points per channel. Recently a bi-spectral frequency analysis of single channels was performed. The bi-spectrum is defined as $\langle F(\omega_1)\cdot F(\omega_2)\cdot F^*(\omega_1+\omega_2)\rangle$ where F is the Fourier transform of the signal. It is a measure of the coherence and the average phase shift between the component measured at a frequency $\omega_1+\omega_2$ and the result of a fictive quadratic mixing of the two components at frequencies $\omega_1$ and $\omega_2$.

It is impossible to derive physical mechanisms directly from these statistical observations. We draw general conclusions about the physics involved from the entity of observations and propose a set of basic effects to include in a theoretical model. Being still unable to solve the complex nonlinear problem of the fully developed turbulence exactly we attempt to describe the turbulence with a simple non-self-consistent statistical model. This allows to derive plausible physical interpretations of several features of the statistical functions and may be used as a guide-line for the development of a manageable theoretical model.

## Experimental description of the edge turbulence

From the fluctuations of the ion saturation current and the floating potential measured with probes one derives density fluctuations with a relative level $\tilde{n}/n$ up to 50 % and potential fluctuations with rms values of typically 5 V, respectively. Reliable measurements of temperature fluctuations are not available. There are, however, indications that the relative level of temperature fluctuations is in the same order of magnitude as that of density fluctuations. Mainly potential fluctuation measurements may therefore be disturbed by temperature fluctuations.

The fluctuations show a flute-like (2-d $\perp\vec{B}$) structure. Correlation lengths are typically 1 cm $\perp\ \vec{B}$ and several 10 m along field lines. Poloidal propagation velocities outside the separatrix are a few 100 m/s in the ion diamagnetic drift direction during ohmic medium density discharges. With beam injection the velocity is higher and is influenced by Doppler-shift due to the toroidal plasma rotation. In ohmic high density discharges the velocity goes to zero or even changes sign. Inside the separatrix the

fluctuations always propagate in the electron diamagnetic drift direction. In the so-called shear layer at the separatrix (typical width 1 cm) there is a steep velocity gradient. In double-null discharges the scrape-off layer is divided in two parts by the two stagnation points. Fluctuations appear only in the low-field part.

Details about experimental statistical functions can be found in earlier papers [1-4]. We present here a few examples. Fig. 1a shows a time-space correlation function of the plasma potential measured during a high density discharge where the fluctuations did not propagate. The time-space cross-correlation between density and potential from the same shot is shown in fig. 2a. Eddies around potential maxima or minima due to E×B-drift explain the structure of this correlation function. A time-averaged k-spectrum of the potential fluctuations from another shot is shown in fig. 3a. The only scale length which can be derived from this spectrum is the inverse of the k at the transition from the flat part to the decay. It corresponds to the width of the scrape-off layer.

When the fluctuations propagate (i. e. in the normal case), space-time correlation functions and frequency-wavenumber spectra both show a skewed structure. In the model described in the following section this trivial effect is not included. For easier comparison we present here examples from special discharges with $v = 0$. Generally one should compare only invariant parameters and properties.

Density correlation functions show a typical undershoot to negative correlations up to 20% . The half width or the zero-correlation point allow to define an invariant correlation length. To define a correlation time one has to trace the spatial maximum of the correlation for each time point. This invariant temporal correlation function can be approximated by an exponential defining an invariant correlation time. k-ω-spectra at different radii and the variation of correlation parameters and of the propagation velocity with the plasma current and density can be found in [4].

The frequency bi-spectrum is a function of two variables, the wavenumber-frequency bi-spectrum would be a function of four variables. With reasonable CPU time it was only possible to compute frequency bi-spectra, which also contain spatial information due to the Doppler-shift. Bi-coherence values are above noise level only at low frequencies up to about 100 kHz. The most prominent observation are the different bi-phases from potential and density fluctuations. Bi-phases are rather constant in the range of significant bi-coherence. For potential fluctuations they are always around $\pi$, for density fluctuations around $-\pi/3$. This means that the "typical waveform" of potential signals is symmetric, that of density signals tends to a sawtooth with steep leading edge.

## Components of a physical model

In the scrape-off-layer all field lines intersect the target plates. The physics of the sheath and of the pre-sheath determine the average electrostatic potential along $\vec{B}$ and the energy balance on flux bundles. The correlation length along the magnetic field is much longer than the connection length between the target plates. There will be a relatively short gradient zone in front of the target plates. For this reason a 2-d model should be adequate. Similar considerations can be found in [5,6]. Algebraic equations are good approximations to describe the physics at the target plate, i. e. the relation of variables like $T_e$, $n_e$, $\Phi$ between the target plates and the plateau zone. 2-d differential equations neglecting inertia seem to be adequate to describe the rather slow drift motion of the plasma perpendicular to the magnetic field. An electrostatic fluid model should be sufficient. There is no indication that kinetic effects are important in this collision-dominated plasma nor that electromagnetic effects are significant.

$\Phi$ is determined by the sheath potential (including a resistive part), the thermoelectric force, the parallel electron pressure gradient and a resistive voltage drop due to the parallel current density. In a non-uniform plasma currents $\parallel \vec{B}$ are generally necessary to compensate the divergence of the diamagnetic current density. In the turbulent state the plasma parameters vary in space on a short scale length. Consequently the electrostatic potential varies $\perp\vec{B}$ causing a random E×B-drift motion with a

non-zero average poloidal component in the ion diamagnetic drift direction (due to the strong average inward $T_e$ gradient).

Neglecting classical transport $\perp \vec{B}$ energy and particles on flux bundles are lost to the region near the target plate. Atomic physics processes are important for the particle balance and energy loss. For the energy loss also the finite parallel heat conductivity and the energy transfer to the target plate, which depends on plasma parameters and on the parallel current density, are important.

The curvature of the magnetic field could be an explanation for the in-out asymmetry of fluctuations. Individual terms may be negligible at least in parts of the full parameter range. For example the electrical resistivity of the sheath may be negligible in the high-density low-temperature range where the resistivity of the plasma is large and vice-versa.

## Ad -hoc model as a zero-order description of the turbulence

As an aid for the interpretation of statistical functions and as a guide-line to the development of the self-consistent nonlinear model as outlined above we try to model zero-order effects of the turbulence by a simple random superposition of eddies in a 2-d space with a given non-uniform density distribution. The eddies are generated by spontaneous rotationally symmetric "potential events" with given radial profile and temporal waveform (cosine-bell and 1/cosh, respectively). The diameter of the events is random with a given probability distribution, their life time is statistically coupled to the diameter, the spatial and temporal distributions are uniform.. Density fluctuations evolve due to the E×B-rotation of the non-uniform initial density. The density perturbation is assumed to be damped with a time constant proportional to the life-time of the potential perturbation. For the figures shown (1b, 2b, 3b) the radius of the eddies varies between 2 mm and 2 cm. Zero time shift of the maximum correlation between density and potential perturbations as measured (see fig 2a) is only obtained if the potential amplitude is chosen such that the eddies perform a half-turn in the average. An inverse pendulum with strong viscous damping would perform a motion of this kind. In the plasma damping of the rotation could be caused by interaction with smaller eddies. The density decay is a crude model for a diffusive decay (also due to the interaction with smaller eddies) and losses to the target plate. It was found that the shape of contours of the statistical functions and other features are better modeled if we assume double eddies, i. e. two equal potential "events" with opposite sign at a distance of the radius of one event. Time constants and diameters were chosen to give reasonable agreement with measurements, but a full optimization was not performed. The best choice for the time constant is proportional to the square of the size, i. e. a diffusive time constant. In order to obtain a size-independent density in time and space the probability distribution has to be inversely proportional to the fourth power of the size.

## Conclusions

Rather sophisticated measurements and evaluations were performed on the edge turbulence of ASDEX. Many features of the measured statistical functions may have a rather simple interpretation. The steep probability distribution of the size of eddies necessary in this model indicates some problems to be expected when attempting to obtain a relevant numerical solution of the physical model.

## References


/1/ A. Rudyj, IPP III/160, July 1990.

/2/ G. Theimer, IPP III/169, Dec. 1990.

/3/ A. Rudyj et al., 17th EPS Conference on Controlled Fusion and Plasma Heating, Amsterdam 1990. Europhysics Conference Abstracts Vol. 14B, part III, p. 1464 - 1467.

/4/ H. Niedermeyeret al., 18th EPS Conference on Controlled Fusion and Plasma Physics, Berlin 1991. Europhysics Conference Abstracts Vol. 15C, part I, p. I-301–I-304.

/5/ A. V. Nedospasov, Sov. J. Plasma Phys. **15** (10), 1989, p. 659.

/6/ X. Garbet et al., Nuclear Fusion, Vol 31, No. 5 (1991), p. 967.

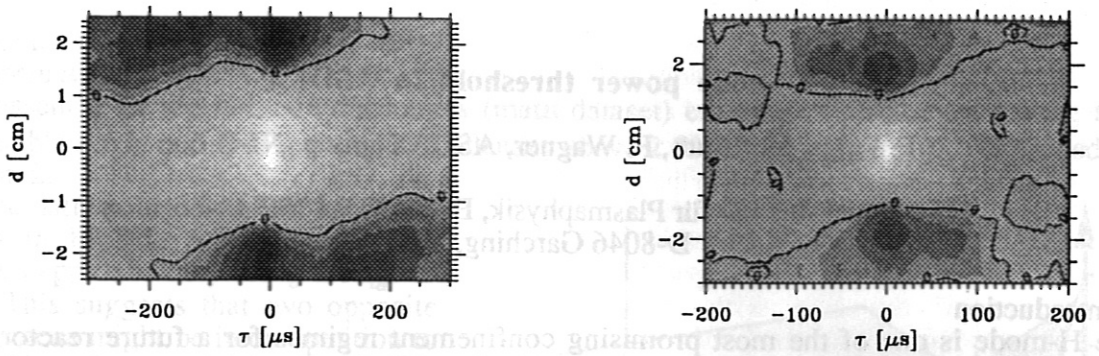


Figs. 1a (left) and 1b (right). Time-space correlation function of plasma potential fluctuations computed from measured (left) and simulated data. For easier comparison with the simulation a discharge with zero propagation velocity was chosen. Dark means negative correlation, light means positive correlation. The zero contour is indicated by a solid line.

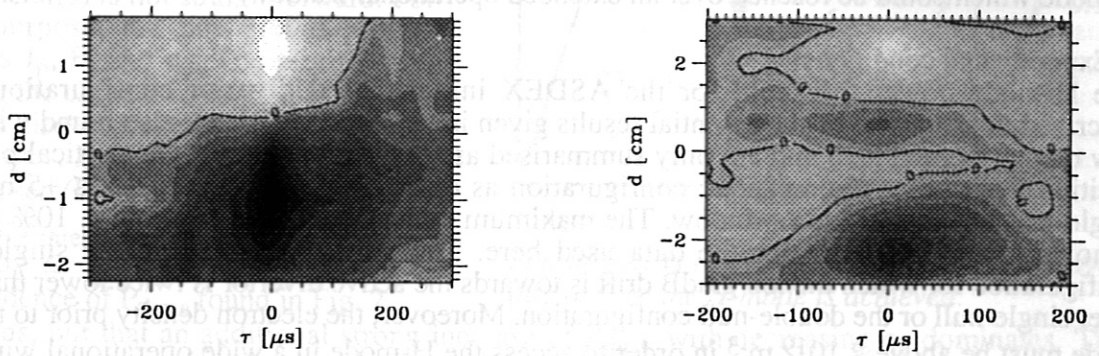


Figs. 2a (left) and 2b (right). Time-space cross-correlation function of density and potential fluctuations from measured (left) and simulated data. Same discharge and simulation, respectively as for fig. 1. These plots show that a positive potential is correlated with high density on one side and low density on the other side consistent with an E×B-motion causing influx of thin plasma on one side and outflux of dense plasma on the other side of the potential "event".

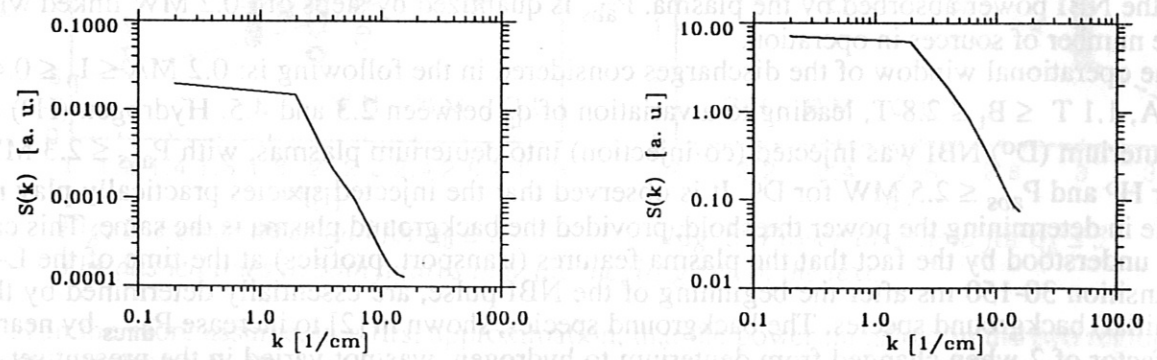


Figs. 3a (left) and 3b (right). Time-averaged wavenumber-spectra of potential fluctuations from measured (left) and simulated data. Different discharge but same simulation as for figs. 1 and 2. The spectra decay $\propto k^{-2.5}$ and $k^{-2.2}$, respectively. Leveling-off at high k due to aliasing.

# H-mode power threshold in ASDEX

F. Ryter, U. Stroth, F. Wagner, ASDEX-group, NI-Group

Max-Planck-Institut für Plasmaphysik, EURATOM-IPP Association
D-8046 Garching, FRG

## 1. Introduction

The H-mode is one of the most promising confinement regimes for a future reactor. It is therefore important to identify the parameters determining the minimum power (power threshold, $P_{thres}$) necessary to reach it. Moreover, the results could give indication about the underlying physics of the L to H-mode transition. Previous studies performed for ASDEX [1] showed that an open divertor configuration (inducing higher neutral density in the main chamber) required more heating power to obtain the H-mode than the initial closed version. In this paper we present new results from data obtained with the latest closed divertor configuration of ASDEX under boronized conditions. These conditions were favourable for the H-mode which could be reached over an extended operational window.

## 2. Experimental conditions

The H-mode power threshold for the ASDEX initial closed divertor configuration was described in [2]. Some of the essential results given in [2], for co-NBI, are also found with the new data presented here and are only summarised as follows. In ASDEX the vertical plasma position determines the magnetic configuration as double-null for $-5 \text{ mm} \leq z \leq +5 \text{ mm}$ or single-null outside of this z-window. The maximum z-displacement is 40 mm i.e. 10% of the minor radius a = 0.4 m, for the data used here. The power threshold in the single-null configuration for which the ion gradB drift is towards the active divertor is twice lower than the other single-null or the double-null configuration. Moreover, the electron density prior to the H-mode must be above $2\ 10^{19}\ m^{-3}$ in order to access the H-mode in a wide operational window. In this paper, we analyse the dependence of the power threshold versus plasma current ($I_p$), magnetic field ($B_t$) and/or edge cylindrical safety factor $q_a$ .

For this purpose, we take all kinds of H-mode discharges (ELMy or ELM-free) into account. The reason for this choice is that we assume the transition physics into the ELMy and ELM-free H-mode regimes to be the same. Discharges showing short H-mode phases after sawtooth crashes are considered to be at the threshold and named marginal (M). These M and the L-mode data are essential to unambiguously determine the power threshold. The power considered here is the total heating power ($P_{tot} = P_{OH} + P_{abs}$) where $P_{OH}$ is the residual Ohmic power and $P_{abs}$ is the NBI power absorbed by the plasma. $P_{abs}$ is quantized by steps of ≈0.2 MW linked with the number of sources in operation.

The operational window of the discharges considered in the following is: $0.2 \text{ MA} \leq I_p \leq 0.46$ MA, $1.1 \text{ T} \leq B_t \leq 2.8$ T, leading to a variation of $q_a$ between 2.3 and 4.5. Hydrogen ($H^o$) or deuterium ($D^o$) NBI was injected (co-injection) into deuterium plasmas, with $P_{abs} \leq 2.3$ MW for $H^o$ and $P_{abs} \leq 2.5$ MW for $D^o$. It is observed that the injected species practically play no role in determining the power threshold, provided the background plasma is the same. This can be understood by the fact that the plasma features (transport, profiles) at the time of the L-H transition 30-150 ms after the beginning of the NBI pulse, are essentially determined by the (initial) background species. The background species, shown in [2] to increase $P_{thres}$ by nearly a factor of 2 when changed from deuterium to hydrogen, was not varied in the present set of data.

In the divertor H-mode, the distance between plasma surface and the next protection limiter, which prevents the occurrence of the H-mode when it is smaller than typically 1 cm, was kept large enough so that the data are not biased by this effect.

3. Results

*3.a. Main dataset*

The essential of the H-mode discharges (main dataset) consists of discharges having the favourable single-null configuration and a density above 2 $10^{19}$ $m^{-3}$ for the reason mentioned in section 2.

A schematic overview of the results is given in Fig. 1. A clear minimum appears approximately along the $q_a = 3$ line. This suggests that two opposite phenomena might be in competition to determine the power threshold. We therefore will separately analyse each side of the minimum to find out whether the power threshold in both regions is governed by different parameters. Due to the linear relation between $I_p$, $B_t$ and $q_a$, the identification of the relevant parameter(s) is not straightforward. For this purpose, the power was plotted versus $I_p$, $B_t$ and $q_a$. The plot (if any) giving the clearest separation between L and H discharges indicates the relevant parameter. For $q_a \geq 3$, $B_t$ clearly has to be chosen (Fig. 2). Fitting the boundary yields: $P_{thres} = 0.5\ B_t^{1.25}$ [MW, T].

For $q_a \leq 3$, it appears that the $B_t$ dependence of $P_{thres}$ found in Fig. 2 remains, but that an additional strong increase of $P_{thres}$ with decreasing $q_a$ dominates. This behaviour is shown in Fig. 3. The fit of the boundary gives: $P_{thres} = 6.64 - 1.97 q_a$ [MW].

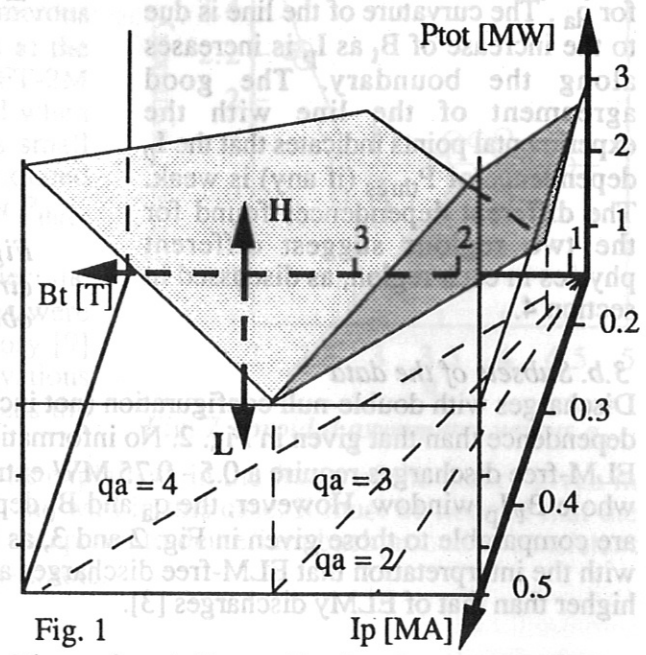


Fig. 1

*The surface is $P_{thres}$. For heating powers above this surface the H-mode is achieved.*

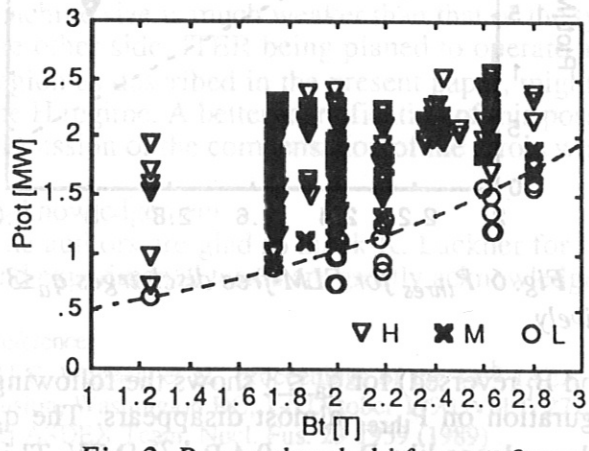


*Fig. 2. Power threshold for $q_a \geq 3$*

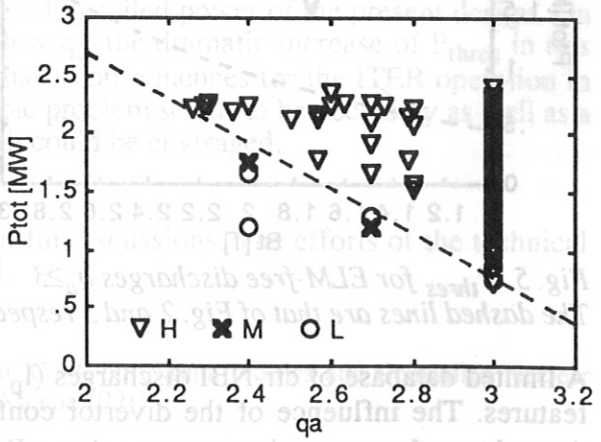


*Fig. 3. Power threshold for $q_a \leq 3$*

*The dashed lines in both figures indicate the fits given in the text.*

We can therefore assume, in a first approximation, that the power threshold in the two regions roughly separated by the $q_a = 3$ line have dependences governed by two different parameters: $q_a$ for $q_a < 3$ and $B_t$ for $q_a \geq 3$. The boundary between both regions was analysed in more detail by looking for the experimental minimum of $P_{thres}$ for each available value of the current.

The results are given in Fig. 4. The line drawn in this figure is the intersection of the surfaces of $P_{thres}$ in both regions ($q_a<3$ and $q_a \geq 3$) determined by the fits given above. It is the minimum of $P_{thres}$ for each value of $I_p$. $I_p$ is introduced by the formula for $q_a$. The curvature of the line is due to the increase of $B_t$ as $I_p$ is increases along the boundary. The good agreement of the line with the experimental points indicates that the $I_p$ dependence of $P_{thres}$ (if any) is weak. The different dependences found for the two regions suggest different physics in each region, as discussed in section 4.

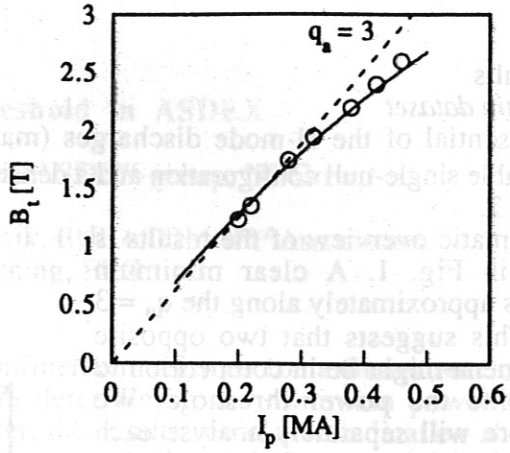


*Fig. 4. Minimum of $P_{thres}$ in the $I_p/B_t$ plan: circles are the experimental data, the line is obtained from the fits as indicated in the text.*

*3.b. Subsets of the data*

Discharges with double-null configuration (not included in the main dataset) show a stronger $B_t$ dependence than that given in Fig. 2. No information is available for $q_a < 3$.

ELM-free discharges require a 0.5 - 0.75 MW extra heating compared to the ELMy ones in the whole $B_t/I_p$ window. However, the $q_a$ and $B_t$ dependences of the ELM-free power threshold are comparable to those given in Fig. 2 and 3, as shown by Fig. 4 and 5. This is in agreement with the interpretation that ELM-free discharges are achieved for an edge electron temperature higher than that of ELMy discharges [3].

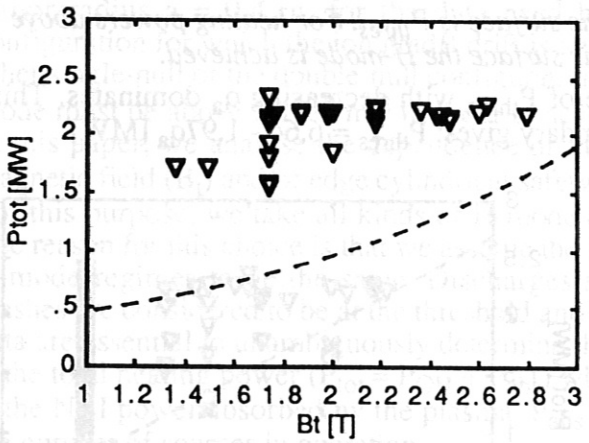


*Fig. 5 $P_{thres}$ for ELM-free discharges $q_a \geq 3$ The dashed lines are that of Fig. 2 and 3 respectively*

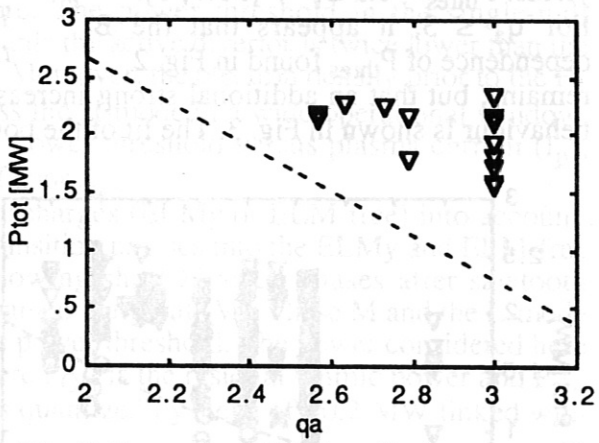


*Fig. 6 $P_{thres}$ for ELM-free discharges $q_a \leq 3$*

A limited database of ctr-NBI discharges ($I_p$ and $B_t$ reversed) for $q_a \leq 3$ shows the following features. The influence of the divertor configuration on $P_{thres}$ almost disappears. The $q_a$ dependence does not exist any more, but a $B_t$ dependence like $P_{thres} = 0.4\ B_t^{1.25}$ [MW, T] is compatible with the data, in the $q_a \leq 3$ region.

4. Discussion

The $q_a$ dependence of $P_{thres}$ for the main data set in the $q_a < 3$ region can be interpreted as follows. In the low $q_a$ operational window, a strong toroidal asymmetry of the power deposition on the divertor neutralization plates was observed in ASDEX [4]. This effect was linked to the creation of magnetic islands (and ergodic regions) by errors fields due to slight

misalignments of the toroidal field coils. The perturbations of the plasma edge associated with these effects increase strongly as the $q_a = 2$ surface approaches the plasma edge. The asymmetry of the toroidal power deposition for representative discharges of the present work plotted versus $q_a$ (Fig. 7) shows a rapid increase for $q_a < 3$ which can be compared to the increase of $P_{thres}$ of Fig. 3. This is in agreement with numerous indications that the L-H transition happens at the plasma edge and with the observations of JFT-2M showing an increase of the power threshold when error fields are applied on purpose [5]. As small coils misalignment cannot be avoided, induced islands and ergodization may be important for $P_{thres}$ in ITER which will operate at low $q_a$.

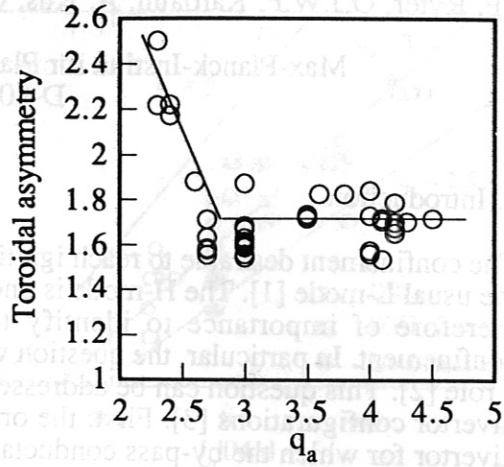

*Fig. 7 Toroidal asymmetry versus $q_a$*

The $B_t$ dependence shown in Fig. 3 might reflect the L-H transition physics. Similar dependences were observed in other tokamaks [6 - 8]. The theory [9] presently meeting best the experimental observations does not predict such a $B_t$ dependence whereas the ones described in [10,11] do.
The observations for ctr-NBI could possibly be explained, in the frame of the theory given in [9], by the large amount of beam ions lost to the wall in this case. It must be noticed that the increase of $P_{thres}$ with hydrogen background compared to deuterium background is consistent with the $B_t$ dependence if the gyro-radius plays a role.

## 5. Conclusion

The H-mode power threshold has a minimum along a line defining two region in the operational window of ASDEX. In the low $q_a$ region, $P_{thres}$ increases with decreasing $q_a$ whereas in the $q_a \geq 3$ region it increases with $B_t$. The possible implications for ITER can be expressed as follows. The $B_t$ dependence does not seem to restrict the future H-mode operation of ITER. In fact, it can be inferred from the present tokamaks [6-8] that the power threshold increase with machine size is much weaker than that of the typical installed power of the present design. On the other side, ITER being planed to operate at low $q_a$, the dramatic increase of $P_{thres}$ in this region as described in the present paper, might have consequences for the ITER operation in the H regime. A better identification of this possible problem seems to be necessary as well as a discussion of the compensation of the errors which could be envisaged.


## Acknowledgement

The authors are glad to thank K. Lackner for fruitful discussions. The efforts of the technical and experimental teams are greatly acknowledged.


## References


[1] F. Wagner, et al., proceedings of the 13th IAEA Int. Conf. on Plasma Physics and Controlled Nuclear Fusion, Washington DC, 1-6 October 1990, Vol.1, 277, (Vienna 1991)
[2] ASDEX Team, Nucl. Fus. **29** 1959 (1989)
[3] H. Zohm, et al. Nucl. Fus. **32** 489 (1992)
[4] J. Neuhauser, et al. proceedings of the 13th IAEA Int. Conf. on Plasma Physics and Controlled Nuclear Fusion, Washington DC, 1-6 October 1990, Vol.1, p. 365, (Vienna 1991)
[5] A. W. Leonard, et al. Nucl. Fus. **31** 1511 (1991)
[6] JFT-2M Group, presented by Y. Miura, proceedings of the 3rd H-Mode workshop,10th-12th June 1990, Vol.1, p 141, ed. by M. Keilhacker, JET.
[7] K. H. Burrell, et al., Plasm. Phys. Contr. Fus. **31**, 1649, (1989)
[8] JET Team, presented by D. J. Campbell, ib.
[9] K. C. Shaing and E. C. Crume Jr., Phys. Rev. Lett. **63**, 2369 (1989).
[10] R. R. Weynants, et al., proc. of the 3rd H-Mode workshop, 1990, Vol.1, p 475, ed. by M. Keilhacker, JET.
[11] A. Rogister, ib. p. 619.

# Influence of divertor geometry and boronization on ELM-free H-mode confinement in ASDEX

F. Ryter, O.J.W.F. Kardaun, A. Kus, O. Vollmer, U. Stroth, F. Wagner, ASDEX-, NI-Teams

Max-Planck-Institut für Plasmaphysik, EURATOM-IPP Association
D-8046 Garching, FRG

## 1. Introduction

The confinement desirable to reach ignition in ITER must be improved by a factor of two above the usual L-mode [1]. The H-mode is one of the most promising regimes to reach this goal. It is therefore of importance to identify the conditions that possibly influence the H-mode confinement. In particular, the question was risen whether the divertor configuration might play a role [2]. This question can be addressed in the ASDEX tokamak which went through 3 main divertor configurations [3]. First: the original divertor ("DV-I",1980-1986) a so-called closed divertor for which the by-pass conductance between divertor chamber and main chamber was comparable to the divertor neck conductance. Secondly: an open divertor ("DV-II open",1987-1989) for which the by-pass conductance was clearly larger than the neck conductance. Thirdly and finally: this divertor DV-II was made tight ("DV-II closed",1989-1990) and the conductance was again of the order of that of the divertor neck. During this last experimental period the vessel was boronized whereas the wall conditions were stainless steel for the two other cases. In the open divertor the neutral gas density in the main chamber was higher than in the closed cases. The influence of the configuration was shown in [3] for ELMy discharges: for the open divertor the confinement of such discharges was on the average 30% lower than in the closed case. This was attributed to an increase of the ELM activity possibly linked with the higher neutral density. In ref [3], was also shown that the power threshold for the open divertor was higher than for the closed ones.
A study of the influence of the divertor configuration on the intrinsic H-mode confinement must be performed with ELM-free (H*) discharges analysed under similar conditions to avoid the non-quantified influence of the ELM activity. This is the aim of the present paper.

## 2. Experimental conditions and analysis

ELM-free discharges in ASDEX required an adequate positioning of the plasma column with respect to the vessel and a heating power above the threshold of ELMy discharges [4]. Under these conditions, ELM-free discharges in ASDEX were fairly reproducible. An example of the type of ELM-free discharges used in the present work is given in Fig.1.

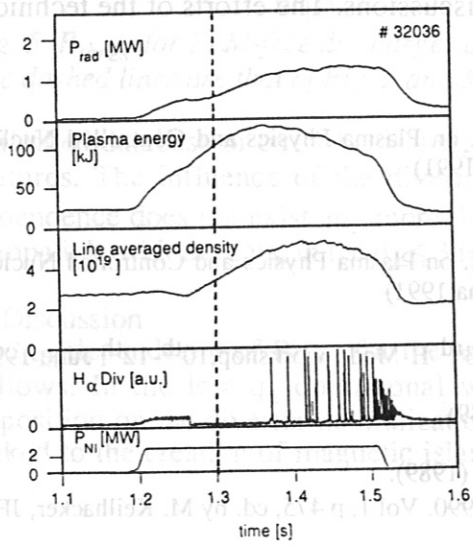


*Fig. 1 Time evolution of some signals for an ELM-free discharge: NBI power, $H_\alpha$ in divertor, line density, plasma energy from the diamagnetic loop, volume integrated radiation. The time of the analysis, as described in the text, is indicated by the vertical line.*

The ELM-free phase is clearly shown by the $H_\alpha$ signal drop in divertor as well as by the increase of the electron density and of the plasma energy.

Fig. 2 gives the Ip/Bt operational window of the H* discharges analyzed for this paper. Due to the higher power threshold for DV-II open [3], the H* operation was.limited during this period. The available datasets for the three divertor configurations only allow the comparison of hydrogen NBI-heated deuterium plasmas. This introduces a small uncertainty on confinement due to the isotope effect. This error remains small because, although the species concentrations in the plasma core are not precisely known, they are probably reproducible for similar discharges under comparable conditions. This should allow a rather fair comparison of the confinement time for the three divertor configurations.

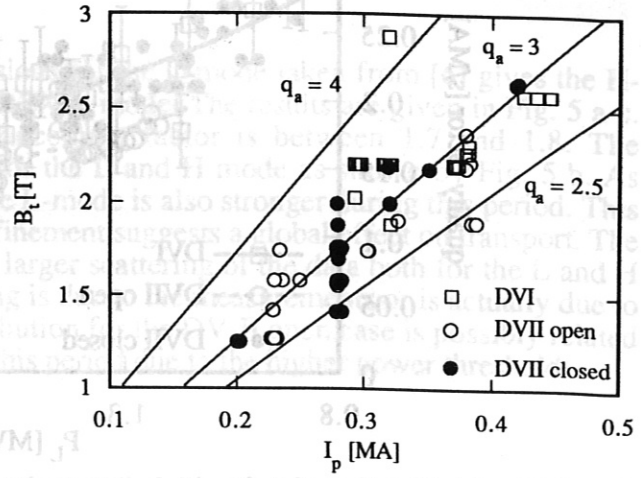


*Fig. 2. Operational window for the 3 configurations*

The confinement time analysis was performed at the time point where $dW/dt = 0.3\ P_{tot}$. W is the plasma energy, $P_{tot}$ is the total heating power $P_{tot} = P_{OH} + P_{abs}$, with $P_{OH}$ residual Ohmic power and $P_{abs}$ NBI power absorbed by the plasma. The reasons for this choice of the analysis time point are that, at this stage of the discharge, the H-mode is well developed but that the radiation in the plasma core is still small compared to the central heating power. Therefore, the confinement time is practically not affected by radiation losses. Moreover, due to this condition, the confinement time is measured well before the discharges reach the beta limit. These two important conditions would not be fulfilled if the analysis were made at the maximum of the plasma energy.

The confinement time is derived from the diamagnetic loop measurement by the expression: $\tau_E = W_{dia} / P_L$ with $P_L = P_{tot} - dW/dt$. The error on the confinement time is estimated to be ±15%. Under the conditions of the discharges considered here (rather high density), this measurement includes a 10% - 15% contribution due to the of fast beam ions.

## 3. Results

To get an impression of the experimental reproducibility for comparisons with the following results, we analyzed one series of 28 boronized H* discharges performed consecutively with identical operational machine parameters. The results are given in Fig. 3 which shows the confinement time normalized to the corresponding L-mode scaling presented in [6]. This distribution has a mean value of 1.76 and a standard deviation of 0.04. This means a relative error of 2.3% which is 6 times narrower than the assumed experimental error on $\tau_E$. This estimate from Fig. 3 is an absolutely lowest value of the experimental error. It does not include any systematical error or changes with plasma and machine conditions from day to day over a long period of time, as it is based on a small number of homogeneous discharges.

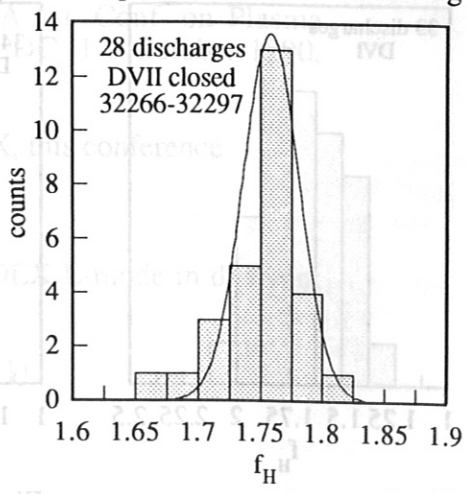


*Fig. 3. Statistical distribution of the normalized confinement time.*

A good visualisation of the influence of the divertor configuration is provided by the confinement quality factor, $\tau_E/I_p$, plotted versus $P_L$ in Fig. 4.

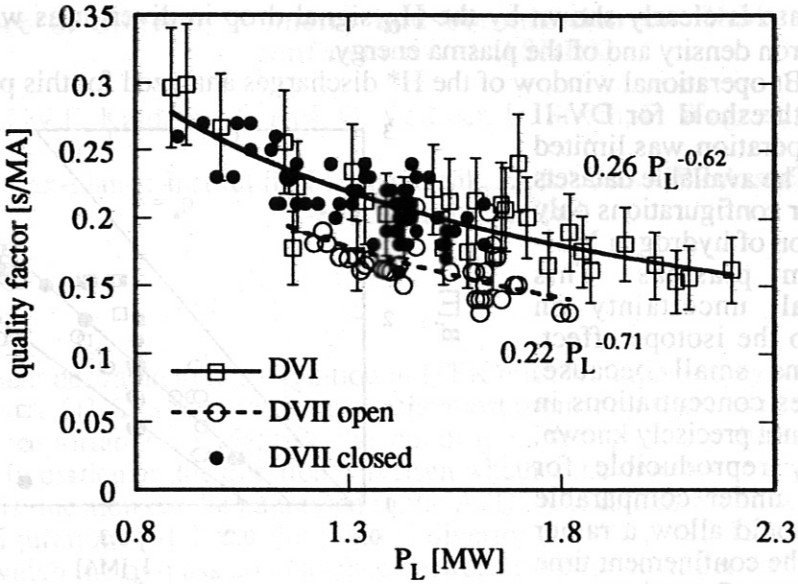


*Fig. 4. Quality factor, $\tau_E/I_p$, for the 3 divertor configurations. The lines indicate the fits versus power. The individual fits for the closed versions are so similar that only that of DV-I is given.*

The two closed versions have the same quality factor and the same power dependence: $\tau_E/Ip = 0.26\ P_L^{-0.62}$. The lack of points with $P_L > 1.7$ for DV-II closed is due to the limited available NBI power during this period. The quality factor for DV-II open is systematically 15-20% lower than the closed versions and has a somewhat stronger power dependence: $\tau_E/Ip = 0.22\ P_L^{-0.71}$. The difference between closed and open configurations is only slightly larger than the measurement errors (±15%). The change due to the open configuration for these ELM-free discharges is however about half of that for the ELMy discharges [3], in agreement with the hypothesis [3] of an increased ELM degradation of confinement with the open divertor. It must be noticed, as shown by Fig. 4, that the boronization (DV-II closed) did not improve the confinement time as it did for DIII-D with the VH-mode [7]. The change of the confinement time with divertor configuration is not a particular feature of the H-mode. In fact the L-mode study described in [6] shows similar effects. Normalizing the H-mode confinement during the

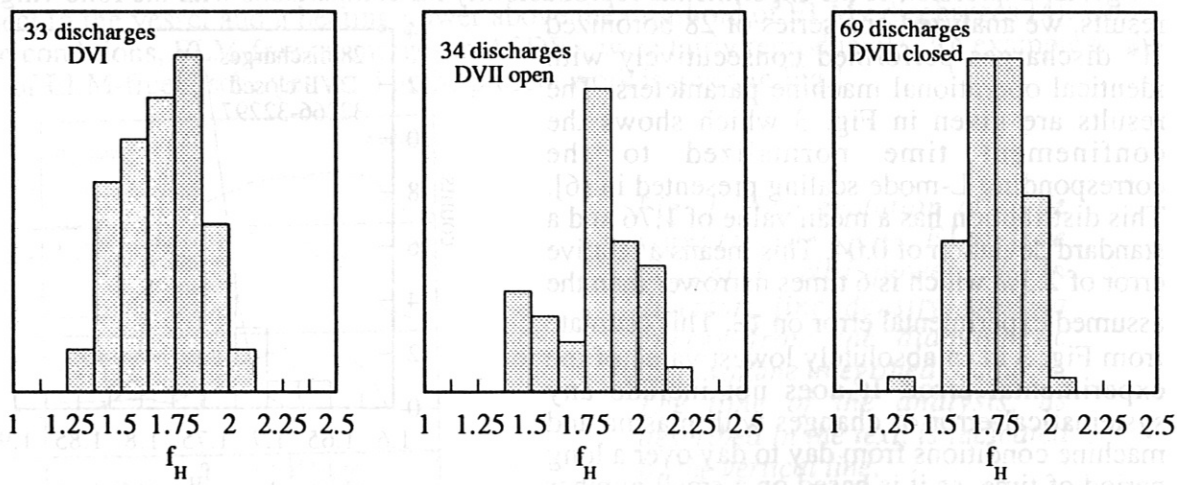


*Fig. 5 a.* *Fig. 5 b.* *Fig. 5 c.*

*Statistical distribution of the normalized confinement time for the 3 configurations.*

three periods with the corresponding expressions for the L-mode taken from [6] gives the H-mode enhancement factor relative to the ASDEX L-mode. The results are given in Fig. 5 a-c. For each of the 3 periods, the mean enhancement factor is between 1.7 and 1.8. The degradation for DV-II open is comparable for the L and H mode as shown by Fig. 5 b. As indicated in [6], the power degradation for the L-mode is also stronger during this period. This common behaviour of the H and L mode confinement suggests a global effect on transport. The broader spectrum found for DV-I is due to a larger scattering of the data both for the L and H mode. It is not yet clear whether this scattering is due to the measurements or is actually due to confinement changes. The shape of the distribution for the DV-II open case is possibly related to the restricted H-mode accessibility during this period due to the higher power threshold.

## 4. Conclusion

The confinement time of ELM-free H-mode phases have been studied for the three different divertor configurations of ASDEX. The results are believed to represent the behaviour of the intrinsic H-mode confinement. They indicate that the open version had a 15% to 20% lower confinement time than the closed ones. This affects both the H and L mode as shown in [6] such that the enhancement factor remains roughly constant.

## Acknowledgement

The efforts of the technical and experimental teams are greatly acknowledged.

## References

[1] D. E. Post, et al., ITER Physics, ITER Documentation Series No. 21, International Atomic Energy Agency, Vienna, 1991.

[2] J. P. Christiansen, et al, Nucl. Fus. **32** 291 (1992)

[3] F. Wagner, et al., proceedings of the 13$^{th}$ IAEA Int. Conf. on Plasma Physics and Controlled Nuclear Fusion, Washington DC, 1-6 October 1990, Vol.1, 277, (Vienna 1991)

[4] F. Ryter, et al., H-mode power threshold in ASDEX, this conference

[5] ASDEX Team, Nucl. Fus. **29** 1959 (1989)

[6] U. Stroth, et al., Confinement scaling for the ASDEX L-mode in different divertor configurations, this conference

[7] G. L. Jackson, et al. Phys. rev. Lett. **67** 3098 (1991)

# ICRF power limitation relation to density limit in ASDEX

F. Ryter, ICRH-group, ASDEX-group

Max-Planck-Institut für Plasmaphysik, EURATOM-IPP Association
D-8046 Garching, FRG

## 1. Introduction

Launching high ICRF power into ASDEX plasmas required good antenna-plasma coupling. This could be achieved by sufficient electron density in front of the antennas i.e. small antenna-plasma distance (1-2 cm) and moderate to high line-averaged electron density compared to the density window in ASDEX. These are conditions eventually close to the density limit. ICRF heated discharges terminated by plasma disruptions caused by the RF pulse limited the maximum RF power which can be injected into the plasma. The disruptions occurring in these cases have clear phenomenological similarities with those observed in density limit discharges. We show in this paper that the ICRF-power limitation by plasma disruptions in ASDEX was due to reaching the density limit.

The density limit phenomena in OH and NBI heated discharges of ASDEX were studied in detail and summarised in [1]. The plasma evolution causing a density limit disruption can be described as follows. As the line averaged density is linearly increased by gas puffing, the edge and divertor electron density increases and the electron temperature in these regions decreases. Above a line averaged density of the order of 3-4 $10^{19}$ $m^{-3}$, a poloidal asymmetry of the plasma edge radiation gradually develops. This asymmetry is seen by the bolometer camera as an up-down asymmetry and its sign depends on the plasma configuration and on the ion drift direction. When the divertor temperature reaches 7-5 eV a Marfe appears on the side of higher radiation and moves to the high field equatorial part of the machine. A plasma disruption, caused by the m=2 mode destabilization, occurs after a time delay depending on the edge q value. The density limit is interpreted as an edge density limit: the occurrence of the disruption is determined by the divertor temperature reaching very low values ($\approx$ 5 eV). Due to the relation of electron density and temperature with power balance in the separatrix and divertor regions, the density limit is determined by the edge density and by the power balance.

## 2. ICRF induced disruptions

The ICRF heated discharges were usually performed with density feedback programmed for constant density. In most of the discharges no disruption occurred. Under unfavourable conditions, however, the maximum ICRF power which could be launched into the plasma was limited by ICRF-induced disruptions. They can be classified into two types: "early disruptions" occurring within 100 ms after the beginning of the RF pulse and linked to the turn-on of the RF, "later disruptions" happening clearly later in the RF-pulse and related to a slow evolution of the plasma under RF conditions.

### *2.1. Early disruptions*

Fig.1 a and b show some time traces for one discharge without disruption and one with an early disruption. The rather old boronisation still reduced the oxygen and metallic impurity concentrations by a factor of the order of 2 compared with a situation without coating at all. The common features of both discharges are the edge and divertor density increase, the divertor cooling, the quick increase of the edge radiation as well as that of its asymmetry, just after the RF turn-on. In Fig.1.a. the divertor temperature recovers after 100 ms and enters a quasi-stationary phase, in Fig.1.b a disruption occurs. Discharge #27984 was a repetition of #27983 except that #27984 was pushed closer to the antenna by 5 mm. This somewhat changed the plasma edge in such a way that the marfe (1.25s) which did not fully develop in #27983 did extend in #27984 and the disruption occurred. The universal feature of the early disruptions is

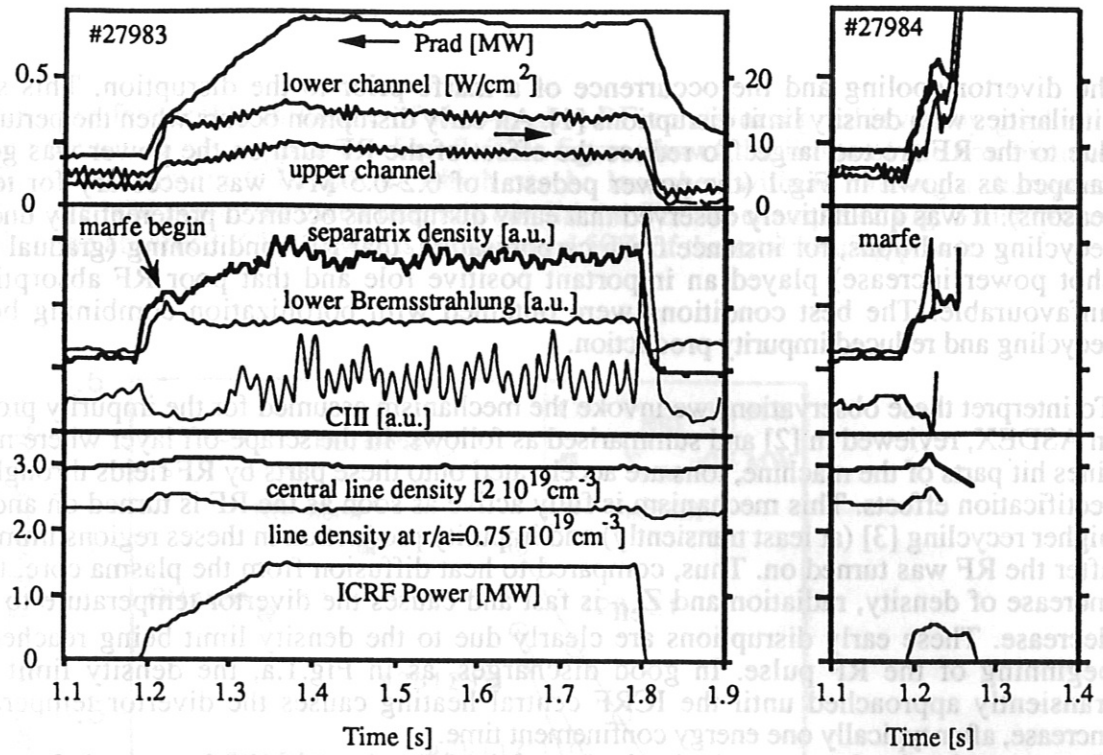


Fig. 1 a (#27983) and b (#27984). Time evolution of some signals (boronized before #27602). Prad is the volume integrated radiation power. The upper and lower channels are the line integrated radiation fluxes of two chords of the bolometer camera looking at z = +38 cm and z = -38 cm respectively. The lower bremsstrahlung is the line integrated visible bremsstrahlung intensity (~ ne2 Zeff Te-0.5) viewing at z = -38.5 cm. This signal is a clear monitor for marfes. CIII is the intensity of the CIII line in divertor and is proportional to the electron temperature in divertor. The separatrix density is given by the lithium beam diagnostic (here not calibrated) in the low field side equatorial plane.

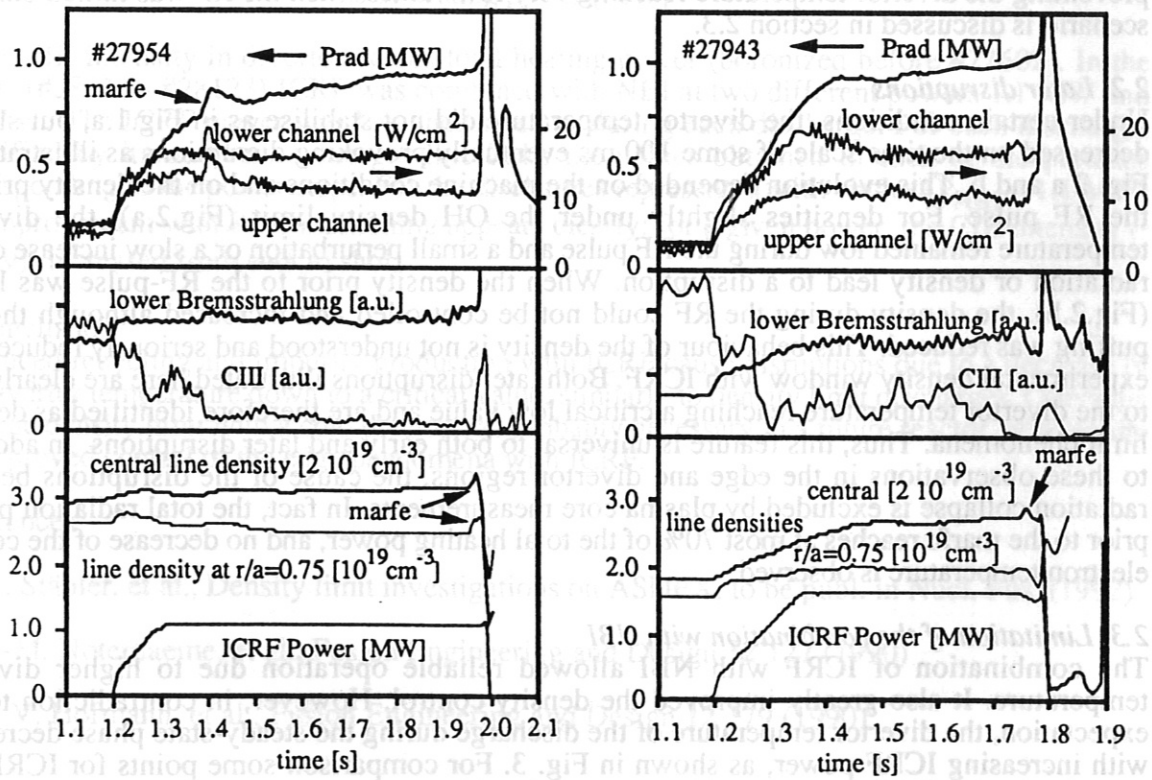


Fig. 2 a (#27954) and b (#27943). Time evolution of some traces for later disruptions. Same signals and conditions as in Fig. 1.

the divertor cooling and the occurrence of a marfe prior to the disruption. This suggests similarities with density limit disruptions [1]. An early disruption occurs when the perturbations due to the RF are too large. To reduce the effect of the RF turn on the power was generally ramped as shown in Fig.1 (the power pedestal of 0.2-0.5 MW was necessary for technical reasons). It was qualitatively observed that early disruptions occurred preferentially under high recycling conditions, for instance fresh carbonisation, that RF-conditioning (gradual shot-to-shot power increase) played an important positive role and that poor RF absorption was unfavourable. The best conditions were obtained with boronization combining both low recycling and reduced impurity production.

To interpret these observations we invoke the mechanism assumed for the impurity production in ASDEX, reviewed in [2] and summarised as follows. In the scrape-off layer where magnetic lines hit parts of the machine, ions are accelerated onto these parts by RF fields through sheath rectification effects. This mechanism is fully active as soon as the RF is turned on and causes higher recycling [3] (at least transiently) and impurity production in theses regions immediately after the RF was turned on. Thus, compared to heat diffusion from the plasma core, the edge increase of density, radiation and $Z_{eff}$ is fast and causes the divertor temperature to quickly decrease. These early disruptions are clearly due to the density limit being reached at the beginning of the RF pulse. In good discharges, as in Fig.1.a, the density limit is only transiently approached until the ICRF central heating causes the divertor temperature to increase, after typically one energy confinement time.
Consequently, the density at the beginning of the RF-pulse must be far enough from the OH density limit to avoid early disruptions. For example, at $q_a = 3$, in the best cases, a maximum value of the Murakami parameter of $M = 4.3$ is tolerable before the RF pulse, compared to $M = 5.5$ reached at Ohmic density limit with the same parameters and wall conditions. It will be shown in the next section, however, that starting at low density leads to other difficulties. A very reliable method to avoid the early disruptions was to preheat the plasma with NBI preventing the divertor temperature reaching very low values when the RF was turned on. This scenario is discussed in section 2.3.

*2.2. Later disruptions*
Under certain conditions, the divertor temperature did not stabilise as in Fig.1.a, but slowly decreased on the time scale of some 100 ms eventually provoking disruptions as illustrated in Fig. 2 a and b. This evolution depended on the machine conditions and on the density prior to the RF pulse. For densities slightly under the OH density limit (Fig.2.a), the divertor temperature remained low during the RF pulse and a small perturbation or a slow increase of the radiation or density lead to a disruption. When the density prior to the RF-pulse was lower (Fig.2.b), the density during the RF could not be controlled and increased although the gas puffing was reduced. This behaviour of the density is not understood and seriously reduced the experimental density window with ICRF. Both later disruptions illustrated here are clearly due to the divertor temperature reaching a critical low value and are therefore identified as density limit phenomena. Thus, this feature is universal to both early and later disruptions. In addition to these observations in the edge and divertor regions, the cause of the disruptions being a radiation collapse is excluded by plasma core measurements. In fact, the total radiation power prior to the marfe reaches at most 70% of the total heating power, and no decrease of the central electron temperature is observed.

*2.3. Limitation of the combination with NBI*
The combination of ICRF with NBI allowed reliable operation due to higher divertor temperature. It also greatly improved the density control. However, in contradiction to the expectation, the divertor temperature of the discharge during the steady-state phase decreased with increasing ICRF power, as shown in Fig. 3. For comparison some points for ICRF not combined with NBI are given. The reasons for this temperature decrease are not clearly identified but are possibly linked with edge and divertor effects (recycling, impurity production and/or radiation) increasing faster with ICRF power than the heating power flux across the

separatrix. The favourable influence of shot-to-shot RF conditioning achieved by gradually increasing the power also appears in Fig. 3. This figure shows the limits of the combination with NBI: the maximum ICRF power which can be launched without causing a disruption depends on the NBI power for given machine conditions. For the example of Fig. 3 disruptions occur when the absorbed ICRF power is only around 50% of the total heating power.

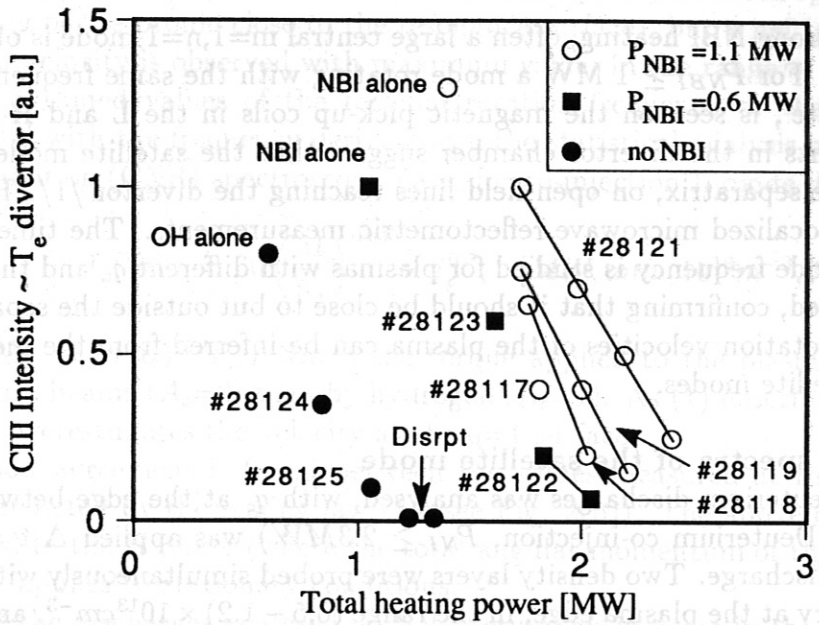


Fig. 3 CIII intensity in divertor versus total heating power (boronized before #27602). In the series (#28117 - #28123) ICRF was combined with NBI at two different powers 1.1 MW and 0.6 MW. The ICRF power was launched in steps during each discharge. For each discharge, identified by its number, a straight line links the values obtained in each of the plateaus corresponding to the power steps. For the discharges represented with circles ($P_{NBI}$ = 1.1 MW) the improvement with RF conditioning appears clearly: for a given power, the CIII intensity (~ $T_e$(div)) increased from shot to shot.

## 3. Conclusion

Enhanced recycling and impurity production with ICRF cause disruptions due to a decrease of the divertor temperature down to a critical value, similarly to density limit discharges. Operating near the density limit with a cold divertor, as probably necessary in a future reactor, will require an improved control of the edge phenomena with ICRF.

## References

[1] A. Stäbler, et al., Density limit investigations on ASDEX, to be publ. in Nucl. Fus. (1992)

[2] J.-M. Noterdaeme, et al., Fusion Engineering and Design **12** 127 (1990)

[3] J. V. Hofmann, et al., Fusion Engineering and Design **12** 179 (1990)

# Reflectometry measurements of the m=1 satellite mode in L- and H-mode plasmas in ASDEX

F. Serra, M. E. Manso, A. Silva, J. Matias, F. Wagner[1], H. Zohm[1], A. Kallenbach[1] and P. Varela

Centro de Fusao Nuclear, EURATOM/IST Association, 1096 Lisboa Codex, Portugal

[1]Max-Planck Institut fur Plasmaphysik, EURATOM/IPP Association, Garching

## 1 - Introduction

In ASDEX, with strong NBI heating, often a large central m=1,n=1 mode is observed on the SXR emission. For $P_{NBI} \geq 1$ MW a mode rotating with the same frequency, the so-called 'm=1 satellite', is seen on the magnetic pick-up coils in the L and H-phases. Magnetic measurements in the divertor chamber suggest that the satellite mode might be located outside the separatrix, on open field lines reaching the divertor /1/. Here we present results from localized microwave reflectometric measurements. The time evolution of the satellite mode frequency is studied for plasmas with different $q_a$ and the mode localization is estimated, confirming that it should be close to but outside the separatrix. The central toroidal rotation velocities of the plasma can be inferred from the measured frequencies of the satellite modes.

## 2 - Local frequency spectra of the satellite mode

A set of H-mode deuterium discharges was analysed, with $q_a$ at the edge between 2.6 and 3.8, where NBI (Deuterium co-injection, $P_{NI} \geq 2.3MW$) was applied $\Delta$ t = 1.2 s after the start of the discharge. Two density layers were probed simultaneously with fixed frequency reflectometry at the plasma edge, in the range $(0.5 - 1.2) \times 10^{13} cm^{-3}$, and local power spectra of density fluctuations were obtained.

As an example, the frequency distribution of the fluctuations detected during # 32225 is shown, as contour plots, in Fig. 1 (a) for $n_e = 0.6 \times 10^{13} cm^{-3}$. The $H_\alpha$ trace (Fig.1(b)) is also presented. A short ELM-free H-mode is observed where the fluctuations are supressed. At the second L-H transition, fluctuations again drop drastically and a coherent (satellite) mode coupled with central m=1, n=1 is clearly detected. Its frequency increases from $f_{L-H} \sim 18$ kHz at the end of the L-phase to a maximum $f_m \sim 24$kHz just before the occurence of the single ELM. The frequencies of the mode agree with Mirnov coil measurements that detect the mode during the L and H-phase, although with lower amplitude in the L-phase. As the layers probed by reflectometry in the L-phase are inside the separatrix but the mode location is outside (as it will be discussed later) the mode is hardly seen by reflectometry before the L-H transition; the high level of turbulence makes it difficult to detect a coherent structure of low amplitude.

As shown in Fig.2(a), the frequencies of the satellite mode grow during the H-phase, from $f_{L-H}$ up to maximum observed values $f_m$. The highest value of the frequency represents a stationary level of the toroidal rotation velocity of the plasma. In some cases, before the saturation is reached, the (1,1) mode may be supressed due to sawtooth events. In these cases the maximum observed value is below the saturated value. The minimum temporal rate of change of the frequency is observed at plasmas with $q_a \sim 3.3$ and the maximum for $q_a \sim 3.8$; in the example of # 32230 ($q_a = 3.8$) a late transition occurs ($\sim$ 80 ms after NBI) and the maximum observed frequency (30 kHz) is reached soon after ($\sim$ 10 ms), when the mode is supressed.

## 3 - Relation of satellite frequency and plasma central toroidal rotation

As the magnetic field perturbation $\tilde{B}$ is expected to be frozen into the plasma, the measured frequency (f) of the satellite mode can give an estimate of the central toroidal rotation ($f_\phi$) of the plasma. The existence of a pressure gradient in the plasma contributes locally with the diamagnetic electron drift frequency, which can be expressed as a purely toroidal contribution ($f_d$) to the mode frequency /1/. The central toroidal rotation velocity of the plasma can thus be roughly given (for co-injection) by $v_\phi = 2\pi R(f + f_d)$ , where R is the plasma major radius and $f_d$ is evaluated at the q=1 surface. In all the cases analysed there is a decrease in the drift frequency between $t_{L-H}$ and $t_s$ (due to the flattening of the profile close to the resonance surface), but a net increase of the toroidal rotation velocity is observed with maximum values in the range $\sim$ 250 - 350 km/s.

The obtained values of the toroidal rotation frequency at the L-H transition were compared with the frequency derived from the statistical analysis of the charge exchange recombination (CXR) spectroscopy data, for co-injection L-mode discharges /2/:

$$f_\phi[kHz] = 30\left(\frac{M}{\bar{n}_e}\right)^{0.61} \times I_p^{0.3}, \quad [MW, amu, 10^{19}m^{-3}, MA], \tag{1}$$

where M $\sim 1.2(A_b)^{1/2}P_{NI}$ Nm is the torque applied to the plasma, which is higher by deuterium beams ($A_b$=2) than by hydrogen ($A_b$=1). As (1) describes the central speed it slightly overestimates the velocity at the q=1 surface.

A good agreement is found between the values measured at the L-H transition and those predicted by the scaling law (1) (see Fig. 2(b)). The above comparison cannot be extended to the H-phase (where the total angular momentum of the plasma changes), as (1) only applies to stationary conditions.

In all the discharges analysed with deuterium an increase in the toroidal velocity during the H-phase is observed . This behaviour corresponds to early L-H transitions ($\sim$ 35 to 80 ms after beam injection), so the speeding up of the plasma may still last during the H phase. In contrast, in discharges with hydrogen injection the values measured for the satellite mode are constant and typically $\sim$ 17 kHz. This is due to the fact that the transition L-H usually occurs later than in deuterium discharges (some 200 ms after the neutral beams start), so the rotation velocity of the plasma is already saturated at the beginning of the H-phase. These results confirm that for the same set of plasma parameters the speed attained with deuterium injection is higher than with hydrogen.

## 4 - Localization of the m=1 satellite mode

The effect of the coherent fluctuations induced by the satellite mode on the wave propagation can be described using the geometric optics approximation. Fluctuations (with frequency $\Omega$) cause mainly Doppler shifts of the phase $\varphi$ due to the propagation in the plasma, $\varphi(t) = \varphi_c + \Delta\varphi sin(\Omega t + \delta)$, leading to phase modulations of the detected reflectometric signals (V(t)):

$$V(t) \sim \frac{1}{2} + \frac{A^2 J_0(\Delta\varphi)}{2} + AJ_0(\Delta\varphi)cos\varphi + \\ + \sum_{n=1}^{\infty} 2AJ_{2n}(\Delta\varphi)cos2n\Omega t cos\varphi - \sum_{n=0}^{\infty} 2AJ_{2n+1}(\Delta\varphi)sin(2n+1)\Omega t sin\varphi + ... \tag{2}$$

where $J_n(\Delta\varphi)$ is the Bessel function of the first kind, and of order n. The phase modulation $\Delta\varphi$ can be obtained from the relative amplitude of the harmonics (odd or even) of

the frequency ($\Omega$) /3/. The amplitude of the fluctuations ($\delta n_e/n_e$ at the reflecting layer ($x_c$) can be related with $\Delta\varphi$ by:

$$\frac{\delta n_e}{n_e} = \frac{3c}{8\pi f}(\frac{\nabla n}{n})_{x_c}\Delta\varphi \qquad (3)$$

Fig. 4 shows the frequency spectra of fluctuations, (# 32225) , (a) immediately after the L-H transition and (b) 10 ms after L-H, at two plasma layers: (I) $n_e = 0.6 \times 10^{13} cm^{-3}$ and (II)$n_e = 0.98 \times 10^{13} cm^{-3}$. Three harmonics are observed in the spectra due to the modulating frequency of the pertubation ($\Omega/2\pi \sim 18$ kHz). From the ratio between the first and third harmonic, $J_1(\Delta\varphi)$ ./$J_3(\Delta\varphi)$, the values of the amplitude $\Delta\varphi$ were estimated. The temporal evolution of the plasma density profile was modelled from O-mode broadband reflectometry for similar discharges /4/. During the L-phase, with low density gradient ($\sim 0.15 \times 10^{13} cm^{-4}$), the probed layers are located at $r \leq 40cm$ (see Fig.5), inside the magnetic separatrix. Immediately after the transition the gradient at the edge steepens reaching $\sim 0.4 \times 10^{13} cm^{-4}$) at $\sim 10ms$ after L-H; by that time the position of the layers probed at fixed density is estimated to be at (I) r$\sim$ 43 cm and (II)r$\sim$ 42 cm.

From the above study it can be concluded that at the inner layer , (II), the rate of fluctuations decreases during $\Delta t_{L-H} \sim 10$ ms from $\sim 11.3\%$ to $\sim 6.7\%$; for the same time interval, the rate of fluctuations at the outer layer,(I), increases from $\sim 10.8\%$ to a maximum $\sim 31.8\%$. The localization of the mode is therefore shifted outwards from a region around 42 cm, to $r \geq 43$ cm. This is consistent with a mode location close to and outside the magnetic separatrix and a movement outwards during the H-phase by $\geq 1cm$. The spectral analysis shows a subsequent decrease in the rate of fluctuations at both layers. As the probed layers are now roughly at fixed radial positions (the build up of the density gradient at the edge is completed $\sim 20ms$ after L-H), the decrease of the fluctuations suggests therefore that the mode is being displaced further outwards following the displacement of the magnetic separatrix.

## 5 - Conclusions

The temporal evolution of the so-called "m=1 satellite mode" (coupled to the central m=1,n=1 activity) is studied with microwave reflectometry in H-mode plasmas with $q_a$ between 2.6 and 3.8. The central toroidal velocities of the plasma are inferred from the measured mode frequencies, which increase during the H-phase for the deuterium co-injection discharges; a maximum temporal rate of change of the velocity is obtained for plasmas with $q_a \sim 3.8$, and a minimum for $q_a \sim 3.3$. The localization of the mode is obtained from density profile reflectometry measurements and from the analysis of the local frequency spectra. Results show that the mode should be localized close to and outside the magnetic separatrix, giving further evidence to the previous estimates based on magnetic measurements /1/. During the H-phase the maximum amplitude of the mode is observed to shift outward by $\geq 1$ cm, suggesting that the mode is radially moving outward together with the magnetic separatrix.

## References


/1/ O. Klüber et al., Nuclear Fusion, Vol. 31, No. 5, 907 (1991).

/2/ A. Kallenbach et al., Nuclear Fusion, Vol. 30, No. 4 (1990).

/3/ E. Mazzucato , Report MATT 1151, Plasma Phys. Lab., Princeton (1975).

/4/ M. E. Manso et al., 18th Eur. Conf. Berlin, Vol. 15C, I-393 (1991).

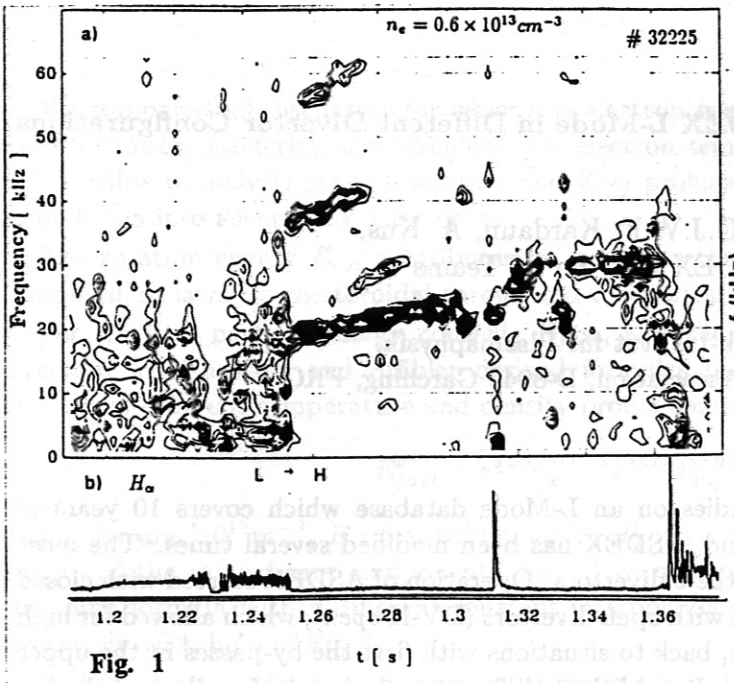


Fig. 1

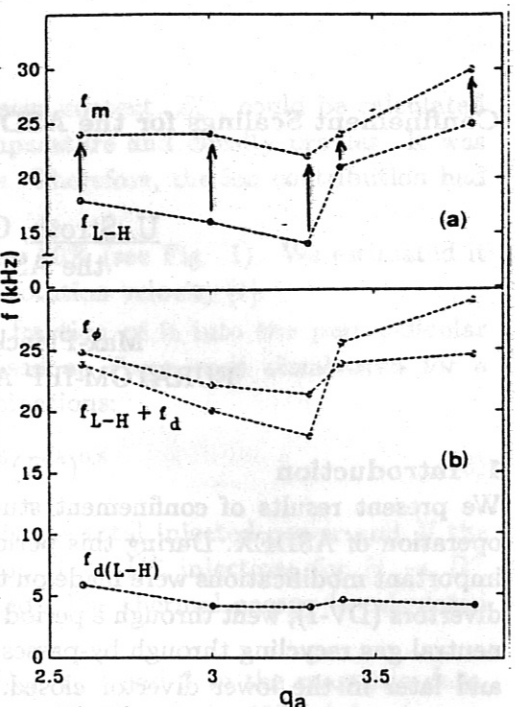


Fig. 2

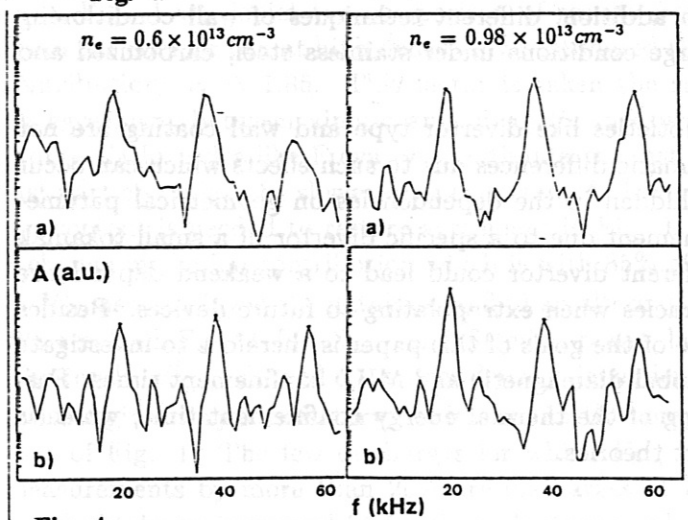


Fig. 4

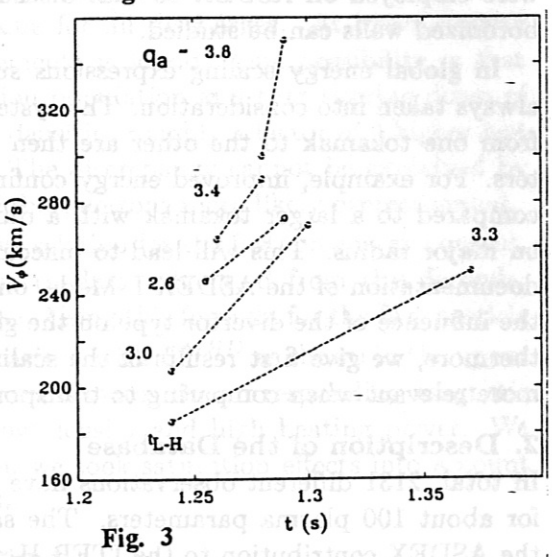


Fig. 3

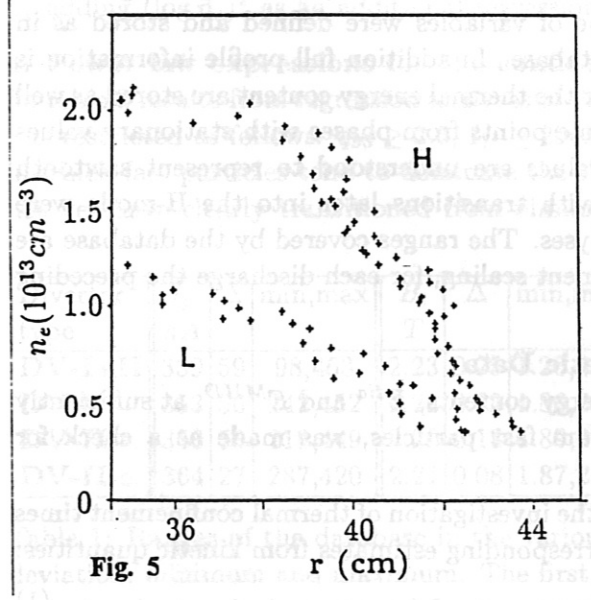


Fig. 5

**Fig. 1** a) Contour plot of the power spectrum at $n_e$=0.6x10$^{13}$cm$^{-3}$, b) $H_\alpha$ at the divertor, for #32225.

**Fig. 2** a) Frequencies of the satellite mode at the transition, ($f_{L-H}$), and maximum values ($f_m$) measured by reflectometry during the H-phase, b) Comparison between $f_\phi$ and $f_{L-H} + f_d$, for different $q_a$ plasmas.

**Fig. 3** Estimate of the central toroidal rotation $V_\phi$ showing its increase from the transition ($t_{L-H}$) to a maximum in the H-phase.

**Fig. 4** Power spectrum of density fluctuations for a) $\Delta t$=1254 - 56 ms, b) $\Delta t$=1264 - 66 ms, for #32225.

**Fig. 5** Density profiles from reflectometry for the L-phase, and for ~10 ms after the L-H transition.

# Confinement Scalings for the ASDEX L-Mode in Different Divertor Configurations

U. Stroth, O.J.W.F. Kardaun, A. Kus,
the ASDEX and the NI Teams

Max-Planck-Institut für Plasmaphysik,
EURATOM-IPP Association, D-8046 Garching, FRG

## 1. Introduction

We present results of confinement studies on an L-Mode database which covers 10 years of operation of ASDEX. During this period, ASDEX has been modified several times. The most important modifications were made on the 2 divertors. Operation of ASDEX started with closed divertors (DV-I), went through a period with open divertors (DV-II *open*), which allowed for high neutral gas recycling through by-passes, back to situations with first the by-passes in the upper and later in the lower divertor closed. In addition, different techniques of wall conditioning were employed on ASDEX so that discharge conditions under stainless steel, carbonized and boronized walls can be studied.

In global energy scaling expressions subtleties like divertor type and wall coating are not always taken into consideration. The systematic differences due to such effects which can occur from one tokamak to the other are then hidden in the dependencies on geometrical parameters. For example, improved energy confinement due to a specific divertor of a small tokamak compared to a larger tokamak with a different divertor could lead to a weakend dependence on major radius. This will lead to inaccuracies when extrapolating to future devices. Besides documentation of the ASDEX L-Mode, one of the goals of this paper is therefore to investigate the influence of the divertor type on the global diamagnetic and MHD confinement times. Furthermore, we give first results of the scaling of the thermal energy confinement time, which is more relevant when comparing to transport theories.

## 2. Description of the Database

In total, 2131 different observations have been stored in the database, each consisting of data for about 100 plasma parameters. The same type of variables were defined and stored as in the ASDEX contribution to the ITER H-mode database. In addition full profile information is available for 1096 validated cases. Kinetic values for the thermal energy content are stored as well as the estimated contribution of fast ions. Only time points from phases with stationary values of the plasma parameters were included. The values are understood to represent sawtooth averages. Sawtooth-free discharges and others, with transitions later into the H-mode were labeled as subsets and not yet included in the analyses. The ranges covered by the database are listed in Tab. 1. For comparison to ohmic confinement scaling, for each discharge the preceding ohmic phase has been stored.

## 3. Energy Content from Magnetic and Kinetic Data

A comparison of diamagnetic and MHD plasma energy contents, $E^{dia}$ and $E^{MHD}$, at sufficiently high density, to avoid dominant contributions from fast particles, was made as a check for systematic measurement errors.

Another important check and a prerequisite for the investigation of thermal confinement times is to compare both energy measurements to the corresponding estimates from kinetic quantities:

$$E_{kin}^{dia} = c_i E_e^{th} + 1.5\alpha E_{fast} \quad (1)$$

$$E_{kin}^{MHD} = c_i E_e^{th} + (1.5 - 0.75\alpha) E_{fast} + 1.5 E_{rot}. \quad (2)$$

We compared all discharges for which the electron energy content, $E_e^{th}$, could be calculated from Thomson scattering measurements for electron temperature and density profiles. It was not possible to include ion temperature and $Z_{eff}$ profiles. Therefore, the ion contribution had to be taken into account by a factor $c_i$.

The rotation energy $E_{rot}$ contributes by not more than 10% (see Fig. 1). We estimated it using scaling laws for the toroidal torque and the central rotation velocity [1].

For the fast particle energy content, $E_{fast}$, and the fraction of it into the perpendicular direction, $\alpha$, Kardaun and Stäbler derived formulas based on Freya code simulations for a number of different temperature and density profile combinations:

$$E^a_{fast} = e^{5.36} \bar{n}_e^{-1.25} E^{0.75} P_{inj}^{0.95} (E^{th})^{0.5}. \tag{3}$$

The units are $[10^{19} m^{-3}, E : 5 \times 10^4 eV, MW, J]$. $P_{inj}$ is the total injected power and $E$ the energy of the main beam component. Eq. 3 is valid for $D \rightarrow D^+$ injection; for $H \rightarrow D^+$ the same formula with a different constant was postulated. The thermal energy is calculated iteratively with help of Eq. 1.

In Fig. 1 we depict the comparison of results from Eq. 1, 2 and 3 to the magnetic data. From the comparison at high densities we estimated the ion contribute to be 85% of the electron contribution: $c_i = 1.85$. This factor is taken the same for all discharges. At lower density no agreement between kinetic and magnetic measurements is found. One possibility is that Monte-Carlo codes like Freya underestimate the fast ion population and that slowing down of fast particles might be slower than expected. At lower densities roughly a factor of 2 higher fast ion content is needed to restore agreement in Fig. 1. The discrepancy cannot be explained by a change in the ion contribution which is with 85% of the electrons more likely overestimated.

We also employed the database to find an alternative relation for the fast ion energy content. We resolved Eq. 1 for $E_{fast}$ and fitted a power law to data calculated from this formula. The result, $E^b_{fast}$, showed a stronger density dependence. Using this formula for the fast particle content gives very satisfactory results also for the comparison with $E^{MHD}$ as shown in the upper part of Fig. 1. The few discharges for which $E_{kin}$ overestimates the corresponding magnetic measurements by more than 20% are discharges at low density and high heating power. We could obtain an improved fit for these discharges when we took saturation effects into account by adding $(\log \bar{n}_e)^2$ as an additional regression variable.

## 4. Power law expressions for the confinement time

In table 2 results from regression analyses of the energy confinement time are listed. The data set was restricted as follows: $q_{95} \geq 2.5$, $I_P \geq 200kA$ and $B_t \geq 2T$; in order to single out discharges in which fast particles tend to dominate the thermal ion energy content and those which might not yet have clearly transitioned from ohmic to L-mode conditions, $\bar{n}_e \geq 1.5 \times 10^{19} m^{-3}$ and

| Divertor type | $I_p$ $kA$ | $\Delta$ | min,max | $B_t$ $T$ | $\Delta$ | min,max | $P_{tot}$ $MW$ | $\Delta$ | min,max | $\bar{n}_e$ $10^{19} m^{-3}$ | $\Delta$ | min,max |
|---|---|---|---|---|---|---|---|---|---|---|---|---|
| **DV-I+II** | 359 | 59 | 98,463 | 2.23 | 0.25 | 1.26,2.82 | 1.59 | 0.58 | 0.52,3.99 | 3.57 | 1.47 | 0.77,12.7 |
| **DV-I** | 353 | 56 | 242,452 | 2.28 | 0.22 | 1.86,2.82 | 1.58 | 0.57 | 0.72,3.60 | 3.32 | 1.18 | 1.59,8.86 |
| **DV-II** *c.* | 350 | 58 | 218,449 | 2.26 | 0.18 | 1.89,2.80 | 1.57 | 0.50 | 0.74,2.83 | 3.37 | 1.37 | 1.51,12.7 |
| **DV-II** *o.* | 364 | 27 | 287,420 | 2.21 | 0.08 | 1.87,2.45 | 1.74 | 0.59 | 0.93,2.97 | 3.79 | 1.21 | 1.92,10.5 |

Table 1: Ranges of the database in the various divertor configurations: Mean values, standard deviation, minimum and maximum. The first row represent the entire database, the other rows various subsets which were used for the regression analyses.

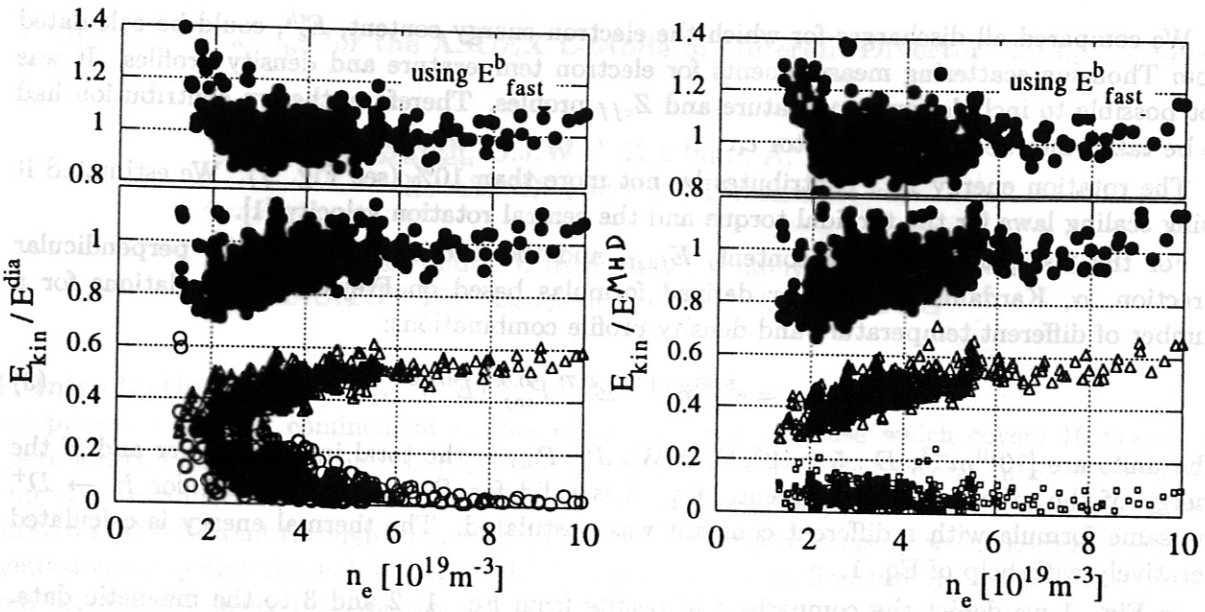


Figure 1: The different contributions to $E_{kin}^{dia}$ and $E_{kin}^{MHD}$ normalized to $E^{dia}$ and $E^{MHD}$, respectively. Left hand side: $1.5E_{fast}^{a}$ (○), $E_{e}^{th}$ (△) and the sum $E_{kin}^{dia}$ (•) according to Eq. 1. Right hand side: $1.5E_{rot}$ (□) and the sum $E_{kin}^{MHD}$ (•) according to Eq. 2. In the upper part the alternative expression $E_{fast}^{b}$ is used.

| Selection | $e$ | $I_P$ | $P_{tot}$ | $m_P$ | $\bar{n}_e$ | $B_t$ | $\tau_E^a$ | $\tau_E^b$ | Obs. | *rmse* |
|---|---|---|---|---|---|---|---|---|---|---|
| **L-Mode scaling for $\tau_E^{dia}$** | | | | | | | | | | |
| **DV-I+II** | -7.9±.1 | .75±.02 | -.52±.01 | .35±.01 | .10±.01 | .08±.03 | .032 | .038 | 1473 | 10.5 |
| **DV-I** | -7.4±.2 | .65±.03 | -.44±.02 | .31±.03 | .12±.02 | .24±.07 | .035 | .041 | 406 | 10.2 |
| **DV-II** | -8.1±.1 | .78±.02 | -.56±.01 | .33±.01 | .14±.01 | .07±.03 | .032 | .039 | 1067 | 9.2 |
| *closed* | -7.6±.1 | .68±.02 | -.43±.01 | .29±.02 | .17±.01 | .09±.04 | .032 | .037 | 319 | 7.4 |
| *open* | -11.1±.5 | 1.24±.08 | -.74±.02 | .20±.02 | .17±.02 | .58±.15 | .028 | .039 | 236 | 9.0 |
| **L-Mode scaling for $\tau_E^{MHD}$** | | | | | | | | | | |
| **DV-I** | -7.1±.3 | .64±.04 | -.33±.02 | .39±.03 | .03±.02 | .18±.09 | .043 | .051 | 406 | 12.5 |
| **DV-II** *c.* | -7.5±.1 | .70±.02 | -.35±.01 | .28±.02 | .05±.01 | .08±.04 | .036 | .043 | 319 | 6.2 |
| **DV-II** *o.* | -10.7±.6 | 1.22±.1 | -.66±.02 | .18±.03 | .09±.03 | .41±.19 | .031 | .042 | 238 | 11.3 |
| **L-Mode scaling for $\tau_E^{th}$** | | | | | | | | | | |
| **DV-I** | -7.1±.2 | .55±.04 | -.66±.02 | .25±.03 | .47±.02 | .07±.07 | .026 | .030 | 406 | 10.5 |
| **DV-II** *c.* | -7.5±.3 | .55±.04 | -.73±.02 | .21±.04 | .65±.02 | .00±.07 | .020 | .023 | 319 | 13.1 |
| **DV-II** *o.* | -10.8±.4 | 1.08±.1 | -.82±.02 | .17±.02 | .48±.03 | .63±.12 | .020 | .026 | 236 | 7.3 |
| **Combined OH and L-Mode scaling for $\tau_E^{dia}$** | | | | | | | | | | |
| **DV-I+II** | -7.7±.1 | .71±.02 | -.60±.01 | .37±.01 | .15±.01 | .06±.03 | .031 | .038 | 1942 | 12.1 |

Table 2: Power law scaling coefficients for $\tau_E^{dia}$, $\tau_E^{MHD}$ and $\tau_E^{th}$ for different divertor configurations: DV-I: both divertors closed; DV-II periods with *closed* and *open* divertors. Number of included observations, root mean square error and $\tau_E$ values in s for two typical discharges ($I_P = 350[kA]$ ($^a$) and $I_P = 450[kA]$ ($^b$), $P_{tot} = 2[MW]$, $m_p = 2$, $\bar{n}_e = 3[10^{19}m^{-3}]$, $B_t = 2[T]$) are given.

$P_{abs} \geq 0.5MW$ were used as additional restrictions. Relaxing any of the constraints does not substantially alter the results.

We calculate the energy confinement time from both, diamagnetic ($\tau_E^{dia}$) and MHD equilibrium ($\tau_E^{MHD}$) measurements. As input power we use the sum of ohmic and neutral beam heating, corrected for shine through losses: $P_{tot} = P_{OH} + P_{abs}$

The agreement of the scaling laws for $\tau_E^{dia}$ and $\tau_E^{MHD}$ as well as the agreement of the scalings for DV-I and DV-II *closed* are satisfactory. The most remarkable result is a substantial change of the current dependence when going from a closed to an open divertor. Discharges in the open divertor configuration show a much stronger dependence on current than discharges done in closed divertor configurations. The difference in $B_t$ scaling, although statistically significant, should be taken with some caution, since it relies only on about 10% of the discharges. Omitting $B_t$ as a regression variable in DV-II *open* does not notably change the dependence on the other variables. The rmse increases only by 0.2%. In Ref. [2], related results were reported for the H-mode.

The current dependence in DV-II *open* could not be estimated with the same accuracy as in the other cases, because there are only very few discharges at higher $I_P$ in this subset. Nevertheless, the difference to the scaling of closed divertor discharges is significant and could be a key to the different scalings one finds for other tokamaks with open divertors Ref. [3].

The power degradation is weaker for $\tau^{MHD}$ than for $\tau^{dia}$ because $E^{MHD}$ is more sensitive to the fast ions which are better confined and of increasing importance with increasing power. In addition one finds a worse degradation for discharges done in the open divertor configuration.

The isotope effect is present in all scaling expressions. It is weaker in the open divertor configuration. In ASDEX, ohmic deuterium discharges at moderate $q$-values have more peaked density profiles than hydrogen discharges. One could speculate, that enhanced recycling in DV-II *open* lowers the capabilities of the density profile to peak and that a similar reason might be responsible, that open divertor tokamaks have less clear signs of the isotope dependence of confinement.

If the data from the ohmic phases are included in the regression (s. Tab. 2) the scaling does not alter substantially. The power dependence is somewhat stronger but the current scaling remains the same within one standard error.

For the thermal confinement time we used the diamagnetic measurement for the total energy content and subtracted the fast ion contribution according to our alternative formula for $E_{fast}^b$. The scaling laws for the thermal confinement time show the same trends as discussed above. But they show different aspects like a stronger dependence on density and a worse degradation with power. Further work is in progress to better elucidate the density and $B_t$ scalings and to explore the link between ohmic and L-mode scaling.

**Acknowledgement**: We would like to thank M. Porbadnik, E. Speth and O. Vollmer for the support in extracting the database.

[1] A. KALLENBACH et al., Plasma Phys. Controlled Fusion **33** (1991) 595.

[2] F. RYTER et al., Influence of divertor geometry and boronization on ELM-free H-mode confinement in ASDEX, *this conference.*

[3] K. S. RIEDEL and S. M KAYE, Nucl. Fusion **30** (1990) 731.

*K. McCormick-10th PSI Conference, Monterey, USA, 30.3-3.4.92*

# Particle and Energy Transport Scalings in the ASDEX Scrape-Off Layer

K.McCormick, G.Kyriakakis*, J.Neuhauser, E.Kakoulidis*,J.Schweinzer, and N.Tsois*
Max-Planck-Institut für Plasmaphysik, EURATOM Association, 8046 Garching, Germany
*NCSR - "Demokritos", Athens, Greece

Key words: ASDEX, scrape-off layer, divertor, edge physics

## Abstract

Parametric dependencies of the scrape-off layer (SOL) diffusion coefficient $D_p$ in the outer midplane, and the effective power flux profile width $\Delta_p$ in the upper, outer divertor chamber for ohmically- and NI-heated (L-mode) ASDEX discharges are presented. $D_p$, derived from SOL density profile measurements (under the supposition of a very simple edge model, $D_p=\lambda_n^2 \nu_{ll}/L_c$, which remains to be verified in detail), exhibits a linear dependence with $T_s$ for $T_s \geq 40$eV, where $T_s$ is the electron temperature slightly inside the separatrix. In magnitude, $D_p$ is about 1/3 - 1/2 $D_{Bohm}$, but is not found to vary with $B_t$. For $T_s<40$eV, in an operational regime where MARFES are favored to appear, $\lambda_n$ -and thus $D_p$- increases dramatically with $q_a$ and with decreasing $T_s$. For the isotopes H and D, $D_p(D) \sim 2/3 D_p(H)$ is found, assuming $Z_{eff}=1$; inclusion of impurities in the model reduces this difference. $\Delta_p$, measured with a reciprocating langmuir probe, scales as $q_a^{0.45} T_s^{-0.86}$, is independent of isotope, and ranges over 1-3cm.

## 1.Introduction

The understanding of particle and energy transport in the scrape-off layer (SOL) of toroidal confinement devices is important for physics interpretation of ongoing experiments, and is vital for the successful engineering of any next-step configuration, where the target plate power loading is predicted to be a major concern. Two common approaches to modeling the problem are: to assume only convective perpendicular transport via Bohm diffusion /1/, since some support exists that $D_p$ is "Bohm-like" /2,3/; or to define a constant ratio between $\chi_e$ and $D_p$, assume they have no spatial dependence and then perform parameter scans with an SOL code to arrive at scaling laws for the relevant divertor quantities /4/. A convincing experimental validation of the transport coefficients and the codes themselves is obviously called for, but is hampered by the generally incomplete characterization of the SOL of present-day tokamaks.

On ASDEX, comprehensive parameter scans in $\bar{n}_e$, $I_p$, $B_t$, and injected neutral power have been carried out, permitting the response of the SOL to be studied in detail. The diagnostic tools used in the present study were the lithium beam probe in the outer midplane to measure the SOL density profile, the YAG Thomson scattering system yielding electron density and temperature at a point slightly inside the separatrix at the lower plasma boundary, and the fast reciprocating

langmuir probe in the upper, outer divertor, which delivers profiles of the power flux $q_{||}$. In section 2, the e-folding lengths $\lambda_n$ of the SOL density profile are presented, from which diffusion coefficients are deduced. In section 3 the power flux profiles are discussed.

## 2.Particle Diffusion Coefficients

Three SOL data sets are considered: **(A)** Divertor configuration DV II /5/, freshly carbonized walls, both divertor bypasses open; OH; H, D; $\bar{n}_e = 0.8 - 5.5 \times 10^{13}$ cm-3, $I_p$ = 150- 420kA, $B_t$ = 1.9, 2.17, 2.55 T. This scan is complete in that the parameter space is fairly uniformily occupied. Scalings for $T_e$ and $n_e$ near the separatrix are given in /5/ for $\bar{n}_{e13}>2.6$. **(B)** DV II, boronized walls, both bypasses reduced; OH,NI($H^o$->$D^+$); D; $\bar{n}_e = 1\text{-}5 \times 10^{13}$ $cm^{-3}$, $I_p$ = 320, 420kA, $B_t$=2.17 T. $P_{NI}$= 0.55 MW **(C)** DV I, stainless steel walls; OH, NI($H^o$->$D^+$,->$He^{2+}$); D, He; $\bar{n}_e = 1\text{-}5 \times 10^{13}$, $I_p$ = 270-420kA (He, only 420kA), $B_t$=2.17 T. $P_{NI}$ = 0.4-1.7 MW. Further details are given in /6/. These scans allow study of $n_e(r)$ in the SOL for the entire spectrum of wall conditioning procedures on ASDEX, as well as divertor configurational changes, permitting a check on the universality of the derived diffusion coefficients and identification of possible systematic errors associated with the assumptions used to derive $D_p$.

### 2.1 Characterization of the SOL density profile

Only data points from the steady-state phase of double-null diverted discharges are considered. All discharges are fueled by gas puffing, with the gas valve positioned well away from the point of measurement. (Gas puffing in the observation sector can lead to a slight increase in the exponential fall-off length $\lambda_n$ for density.) Fig. 1 provides an illustration of typical density profiles. Two effects are evident: With decreasing plasma current (equivalent to increasing $q_a$, along with decreasing heating power), (a) the density profile becomes progressively flatter, and (b) a density shoulder for $R\text{-}R_s \geq 2$cm becomes more evident ($R_s$ is the separatrix position).The break in the shoulder around $R\text{-}R_s \geq 5.5$cm is to be identified with the transition point where field lines no longer enter the divertor due to intersection of material surfaces in the main chamber.

$\lambda_n$ is derived by fitting an exponential to the region $R\text{-}R_s \leq 2$cm. For Fig. 1, this adequately characterizes the density profile for small to moderate $q_a$ ($q_a$=2-4), and again at large $q_a$, but does not give the complete picture for values in between. In practice, this maledy does not seriously affect results in the normal operational regime of ASDEX.

$\lambda_n$ values for data base **A** are presented in Fig. 2 as a function of $T_s$, the electron temperature near the separatrix, which is a useful quantity to order the data. $T_s$ is obtained by assuming temperature profile invariance in order to extrapolate $T_e$ values measured by YAG Thomson scattering at the minor radius of r=18cm to the edge position of the outermost YAG point at z=-39.4 cm /7/. For the range of $T_e$ ($T_e$>40eV) where the YAG detection system functions, the agreement between $T_{e39.4}$ and $T_s$ is quite good. $T_s$ is used to obtain an estimate of $T_{e39.4}$ for values below 40 eV, and also for situations where this information essentially is not available (data set **C**). The temperature at the magnetically determined separatrix may be derived

by extrapolating from the two outermost YAG points, with the result that $T_s(mag) \sim 0.6\text{-}0.7 T_s$.

Examination of Fig. 2 reveals that $\lambda_n(H) \sim \lambda_n(D)$, as substantiated by regression analysis. More prominently, there is a rather abrupt change in behavior around $T_s \sim 40eV$: For $T_s > 40eV$, the points scatter about a line roughly given by $\lambda_n \sim 1.9cm$, whereas for $T_s < 40eV$ there is a dramatic increase in $\lambda_n$ with decreasing $T_s$. This is the operational regime ($q_a \geq 5$, low edge temperature) favorable to the formation of MARFES, and thus may represent a new topological situation at the plasma edge where, for example, temperature gradients parallel to the magnetic field can already occur along flux surfaces inside the separatrix; but this aspect will not be explored here.

The data set of Fig.2 encompasses a wide range of edge densities and temperatures, so that the question of different collisionality regimes becomes relevant. Applying the criterion for collisionality in the SOL of /3/

$$Z_{eff}(SOL) L_c n_s / T_s(mag)^2 \geq 10^{17} / m^2 eV, \qquad (1)$$

the value of $Z_{eff}(min)$ may be derived which must prevail in the SOL to satisfy eq.(1),

$$Z_{eff}(min) \geq 10^{17} T_s(mag)^2 / n_s L_c, \qquad (2)$$

where $L_c$ is the connection length from the midplane to the target plates. Fig. 3 depicts the experimental situation for a subset of **A** ($I_p$=350kA), showing that collisionality may be expected for $\bar{n}_e \geq 3 \times 10^{13}$ cm$^{-3}$. However, on ASDEX it is observed that $Z_{eff}$ rises towards the edge in a fashion commensurate with a constant impurity concentration level /8/. Thus $Z_{eff}$(edge) can easily be a factor of 3 higher than $Z_{eff}(0)$, implying that the SOL can be marginally collisional even for the lower densities. (Note that for DV II ASDEX has copper target plates.)

Fig. 4 summarizes the parametrical dependencies of $\lambda_n$ for data sets **A**, **B** and **C**. One finds $\lambda_n \sim A^{\varepsilon} q_a^{\alpha} T_s^{\beta} P_{sol}^{\delta}$, with $\alpha$=0.45-0.78, $\beta$=0.23-0.41. $\lambda_n(H) \sim \lambda_n(D)$ (i.e. $\varepsilon = 0$). In comparing $D^+$ and $He^{2+}$, the scaling is $A^{0.22}$, meaning that for the limited data set of **C**, $\lambda_n(He) \sim 1.16 \lambda_n(D)$, if all else is the same. Three regressions are listed for **C**: With and without $P_{sol}$ to underline the robustness of the regression coefficients for A, $T_s$ and $q_a$, and also only for the OH subset to demonstrate the closer similarity to **A**. ($\lambda_n$ values where $P_{sol} > 1MW$ have been excluded, as they lay clearly above the other points - possibly the manifestation of another physics regime.) Note that for **C**, $B_t$ is held constant, i.e. $q_a$ is varied through $I_p$ alone. Since **A** has the most extensive $q_a$-scan and the smallest deviation associated with the exponent (see table I), $\alpha \sim 0.45$ is the favored candidate for a general scaling law - about what is expected ($\alpha \sim 0.5$) from connection length arguments within the framework of simple 1-D SOL theory /3/. In the regime $T_s < 40$ eV of **A**, $\lambda_n$ may be described as $q_a^{1.96 \pm 0.16} \bar{n}_e^{0.66 \pm 0.09}$ (Reg. coefficient R=0.93), where the density dependence is probably a hidden temperature dependence in the sense $T_e \sim n_e^{-1}$ /5/ ($T_s$ tends to scatter too much here, not yielding as clean a regression as $\bar{n}_e$.).

Of interest is that for all data sets $\lambda_n$ varies only over the range 1.6-2.5 cm, for $T_s$>40eV.The systematic uncertainty associated with the experimental determination of $\lambda_n$ is about ±1mm, corresponding closely to the vertical spread of points in fig. 4.

## 2.2 Derivation of diffusion coefficients

To arrive at an estimate of the diffusion coefficient the relationship

$$D_p = \lambda_n^2 \nu_{ll}/L_c = \lambda_n^2 f_{ll} C_s/L_c = \lambda_n^2 f_{ll} (eT_e(\gamma_i + Z_i\gamma_e)/m_i)^{0.5}/L_c \qquad (3)$$

will be used, which assumes a source-free SOL, no inward drift, no influence of electric fields, $T_e = T_i$, only one ion species with charge $Z_i$, and a global streaming velocity $v_{ll} = f_{ll}C_s$ (averaged over the midplane/divertor-plate distance $L_c = q_a L_o$; $L_o$=3.33 m on ASDEX) where $C_s$ is the sound speed. $f_{ll}$ is taken as 0.3 in accordance with 1d SOL code calculations /9/ carried out over a wide range of ASDEX operational conditions in conjunction with simultaneous code fittings of some experimentally observable quantities. $\gamma_i = \gamma_e = 1$ is assumed in the following.

From the relationship $\lambda_n \sim q_a^{0.5} T_s^{0.25}$ above, it is immediately apparent that $D_p$ would be expected to scale as $T_s$, which is confirmed. As depicted in fig. 5, $D_p$ uniformly increases linearly with $T_s$ for all three data sets when $T_s \geq 40$eV. The major difference lies in the temperature ranges; this is effected via auxiliary heating, higher heat flux to the edge as a result of better wall-conditioning techniques (boronization) leading to lower global radiated power, and isotope effects. In particular, $He^{2+}$ discharges characteristically exhibit lower edge densitites than $D^+$ for the same line density, and have higher edge temperatures.

In **A** the scaling is $D_p \sim A^{-0.6} T_s^{1.08}$. The mass dependence enters primarily via eq.(3), since there is no significant isotope dependence for $\lambda_n$. That is, the data are consistent with a higher diffusion coefficient for hydrogen being balanced by a higher sound speed, yielding $\lambda_n(H) \sim \lambda_n(D)$. However, inclusion of impurities in an altered form of eq.(3) weakens the indicated mass dependence: For the supposition that $C^{4+}$ ions cause $Z_{eff}$=3 in the SOL, the scaling reduces to $D_p \sim A^{-0.2}$. Further, assuming $Z_{eff}$=2.5, instead of 3, for the $H^+$ discharges ($Z_{eff}$ is generally observed to be lower for $H^+$) yields $D_p \sim A^{-0.37}$. In the case of **C**, we have $D_p(D^+,He^{2+}) \sim A^{0.18} T_s^{0.98} q_a^{0.6} P_{sol}^{0.19}$, which reduces to $A^{0.18} T_s^{0.8}$ for OH conditions. Again, as an example, the impact of $Z_{eff}$=3 from $C^{4+}$ ions in the SOL is to augment the scaling from $A^{0.18}$ to $A^{0.4}$. Considering that the impurity content for the $He^{2+}$ discharges is less than for $D^+$, the scaling becomes more like $A^{0.3}$. It is also quite plausible that $f_{ll}$ in eq.(3) is different for $He^{2+}$ (no code runs exist), again directly influencing the scaling: Taking $f_{ll}$=0.26 instead of 0.3 completely removes the original $A^{0.18}$ relationship!

In fig.6 $D_p$ is compared to $D_{Bohm} = T_s/16B_t$ for the three data sets. One finds $D_p \sim 1/3\text{-}1/2\ D_{Bohm}$. Notwithstanding, for data set **A** where $B_t$ was varied between 1.9 and 2.55T, absolutely no $B_t$ component was found for $D_p$ by regression analysis. Comparison of figures 6 and 7 for **A**

reveals that the data points in fig.7 have been pulled apart, visually demonstrating that a forced $B_t$ dependence of $D_p$ leads to a poorer grouping of the data. The latent consequence of impurities on the absolute value of $D_p$ is benign: $Z_{eff}$=3 from $C^{4+}$ ions lowers the calculated $D_p(D^+)$ by only 25%. Conversely, taking $\gamma_{i,e}$=5/3 enhances $D_p(D^+)$ by 29%.

### 3.Power Flux Widths in the Divertor

Two SOL data sets are considered: DV II, boronized walls, both bypasses reduced (**D**) OH; He; $\bar{n}_e$ = 5-6.6x$10^{13}$ $cm^{-3}$, $q_a$ scan with $I_p$=180-450kA and $B_t$=1.8-2.8T varied such as to effect $q_a$ = 1.9->7.9 in small steps; (**E**) OH, NI($H^o$->$D^+$); D, $\bar{n}_e$=2.2, 3.5, 5.5x$10^{13}$ $cm^{-3}$, $I_p$=320kA, $B_t$=2.17T, $q_a$=3.3, $P_{NI}$=0.25-1.8MW in five discrete steps. Some additional edge information for this series is contained in /5/.

The power flux is derived from triple-langmuir-probe measurements whereby the product of ion saturation current and $T_e$ are modified according to Stangeby's formula for a floating surface under the assumption of $T_e$=$T_i$. The probe is situated about 1.25m (along field lines) from the target plates when $q_a$=3.

Power flux profiles from data set **D** for four $q_a$-values are presented in fig.7. Independent of $q_a$, all profiles are characterized by a steep falloff on the left hand side which is in the private flux region. On the right hand side, with increasing $q_a$ the profile progresses from almost exponential in nature to being very flat as a result of the decrease of the peak near the separatrix and the emergence of a dominating shoulder at larger radii. Phenomenologically, the development of the $q_{||}$ profile with $q_a$ parallels that of the $n_e(r)$ profile in the midplane shown in fig.1.

Although the $q_{||}$ profiles are less plagued with noise problems than $n_e(r)$ or $T_e(r)$, it is generally still difficult to describe the profile in terms of an exponential falloff length - both because of scatter and the two-dimensional change in profile form illustrated in fig.7. More appropriate and robust is the effective power channel width $\Delta_p$, defined as the area under the $q_{||}$ curve divided by the peak value. In this case, the level of uncertainty is around ±1mm.

Plots of $\Delta_p$ vs. $T_{ed}$ for **D** and **E** are given in fig. 8. In both cases, $\Delta_p$ increases smoothly with decreasing $T_{ed}$. For **D**, $\Delta_p$ varies over 1->3cm; and for **E** the change is 1->2cm. A regression on data set **D** alone yields $\Delta_p \sim q_a$ since $q_a$ and $T_{ed}$ are extremely colinear, and $q_a$ exhibits less scatter thereby leading to a better fit. (Higher $q_a$ is achieved by lowering $I_p$, thereby lowering the power input and thus $T_{ed}$.) For **E** the $T_{ed}$ scan is effected by application of five distinct neutral injection power levels for each of three discrete densities while $q_a$ is held constant. Although the relative variation of $\Delta_p$ with $T_{ed}$ is similar between **D** and **E**, some absolute differences do exist at a given $T_{ed}$. This may be ascribed to a $q_a$-scaling also inherent in the data in addition to the strong $T_{ed}$ dependence. A regression on the combined set of **D** and **E** reveals $\Delta_p = 9.2\ q_a^{0.45\pm0.07}\ T_{ed}^{-0.85\pm0.06} - 0.18$ [cm,eV], with R=0.93 (fig.9, bottom). Similar trends emerge if a regression is made over a much larger data base, of which **D** and **E** are subsets. No isotope effect is found.

## 4. Discussion and Conclusions

Using the edge temperature $T_s$ in combination with $q_a$ leads to a good description of $\lambda_n$. Had a regression been performed on global quantities then the result would represent a hidden fit to $T_s$, making interpretation of the result less transparent. Previous descriptions of $\lambda_n$ for ASDEX /6/ are to be understood within this context.

As a reference, $T_s$ has been taken to collate $\lambda_n$ and $D_p$, with the implicit assumption that $D_p$ is invariant for the first few cm outside the separatrix, depending only on a characteristic temperature which describes this region. (It should be kept in mind that $T_s$ is a temperature about 30-40% higher than the temperature at the magnetically determined separatrix.) Since $T_{ed}$ is intimately related to $T_s$, it cannot be excluded per se that $T_{ed}$ is the primordial quantity governing the behavior of $D_p$, and will be checked in the future. Assumption of a radial dependence of $D_p$ with $T_e$ is clearly not consistent with the appearance of the density shoulder at larger radii where $T_e$ is low. One might speculate that the dramatic increase in $\lambda_n$ observed for $T_s$<40eV has its sequel in the range R-$R_s$>2cm, where $D_p > D_{Bohm}$. Another aspect is that the fluctuation spectrum also undergoes a qualitative change in this region /11/, but no definitive conclusions concerning the nature of transport can be advanced at the present time. In any case, the density shoulder in the midplane has its counterpart in the shoulder of $q_{||}$ (and $T_e$, $n_e$) in the divertor.

Within the framework of the model used to deduce $D_p$ from the experimentally measured $\lambda_n$, there is strong evidence that $D_p$ scales with the edge temperature as predicted by Bohm diffusion. Nevertheless, $D_p$ is not found to be sensitive to $B_t$, even though this is within the resolution capabilites of the diagnostic method measuring $\lambda_n$. $D_p$ has been estimated assuming $v_{||} = 0.3C_s$ as suggested by 1d calculations calibrated by fitting other experimental results.This number has been verified recently in a small number of 2d runs /10/. It remains to be seen in future code work if the forefactor for $C_s$ exhibits a systematic variation with the connection length ($L_c \sim B_t$) such as to mask a complete Bohm-like scaling in the present approach.The fact that $D_p(D^+)$ of fig.5 varies in a more-or-less continuous fashion from one data set to another, where the divertor configuration and wall conditioning techniques were changed, indirectly supports the code result that $f_{||}$ does not underlie strong modifications. Apriori, exactly the opposite might be conjectured: $f_{||}$ depends on details of the divertor recycling conditions ($T_e$, $n_e$, flow reversal?, divertor geometry, ...) and these can be expected to vary widely over the range of conditions present in the experiment.

The absolute $D_p$ values are 1/3-1/2 $D_{Bohm}$. This relationship is also a direct consequence of the choice of forefactor for $C_s$, although the error here is probably acceptably small considering the discussion of sec.2.2. For lack of other information, no inwards drift has been assumed in computing $D_p$. If an inwards drift becomes necessary in order to match code predictions with the experimental $n_e(r)$, $q_{||}(r)$ profiles, this will lead to an increase in the estimate of $D_p$.

Regarding the effect of isotopes, both $\lambda_n$ and $\Delta_p$ share a relative invariance with isotope insofar as local temperatures are employed. $D_p(H^+) \leq 1.5 D_p(D^+)$ is derived, with the differences between $H^+$ and $D^+$ becoming less when the influence of impurites in the SOL is included (see discussion in sec.2.2). The indicated scaling tends in the same direction as the isotopic dependence, $D_p \sim A^{-(0.5\text{-}1.0)}$, found in the the main plasma /12/. In like manner, the main plasma experience, $D_p(D^+) \sim D_p(He^{2+})$ /12/, agrees with the SOL result - with the strong caveat that the assumptions to derive $D_p(He^{2+},SOL)$ are less solidly founded than for $H^+$ or $D^+$.

The scaling of $\Delta_p \sim q_a^{0.45} T_{ed}^{-0.86}$ is interesting from a number of standpoints. First of all, the leading factors ($q_a$, $T_{ed}$)which describe $\Delta_p$ are not entirely surprising. As a first approximation, the magnitude of $\Delta_p$ reflects the competition between parallel and perpendicular heat transport: Qualitatively, it is to be expected that $\Delta_p$ increases with $q_a$ in some way, since as the connection length to the target plates (proportional to $q_a$) becomes longer, classical heat conductivity along field lines is predicted to decrease somewhat, allowing perpendicular transport to make itself more evident. Classically, $q_{||}$ also decreases with $T_{ed}$, so that once again the $q_{||}$ profile should broaden if perpendicular transport is not reduced to the same extent.

From a practical standpoint, to reduce target damage due to sputtering in any next step device, it is desireable to operate at low divertor temperatures, i.e. near the density limit. If the physics responsible for the present scaling of $\Delta_p$ prevails, then operation near the density limit will also bring the advantage of an augmented equivalent power flux channel, thus alleviating the specific heat load: At a given density, $\Delta_p$ is predicted to decrease moderately with heating power if $T_{ed}$ is large (>15eV). Referring to fig.8(E), operating in the region of low $T_{ed}$, a change in $T_{ed}$ from 11 to 15eV causes the equivalent heat flux profile to constrict by almost a factor of two from 1.9 to 1.1 cm, which not only excerbates local sputtering, but also the peak heat load. Thus, conditions at the target plate depend quite sensitively on the $T_{ed}$ operational characteristic.

The scaling of $\Delta_p$ with $q_a$ and $T_{ed}$ implies that in a typical ASDEX density limit scan, where $q_a$ is altered from shot-to-shot to obtain a Hugill-type diagram, the increase of $q_a$ (decrease of $T_{ed}$ through decrease of $I_p$) leads to a rapid broadening of the heat flux channel. This is in contrast to the simple Ansatz that the heat flux increases with $q_a$ due to geometric effects, and has the potential of allowing a rather simple MARFE-based SOL model to describe the density limit /13/.

Comparing with other experiments, the divertor plate heat deposition profile half-width in JT-60 has demonstrated no $q_a$-scaling, with the caveat that the profile form changed shape thereby rendering a description of the profile in terms of half-widths to be possibly inadequate /14/. JT-60U has reported a "heat profile peaking factor" (directly related to the inverse of $\Delta_p$), varying as $P_{heat}^{0.49} n_e^{-0.45} q_{eff}^{-0.67}$ /15/. The exponents of $P_{heat}$ and $n_e$ are similar to ASDEX scalings for $T_s$ for NI-heated plasmas ($T_s \sim n_e^{-(0.6\text{-}0.8)} P_{sol}^{0.5}$), such that the JT-60U peaking factor and $\Delta_p^{-1}$ power laws may be quite similar. Finally, recent code calculations for a next-step device predict the "peaking factor" to scale as $q_{eff}^{-0.5} T_{ed}^{0.33}$ /4/.

The data presented in this paper will now serve as a partial target for 2d SOL model validation work using the B2-Eirene code/10/, thus permitting a consistency check on the assumptions used to derive $D_p$ in this paper, as well as possibly new scalings for $D_p$, $\chi_e$ and other quantities.

**References**

/1/ K. Borrass, Nuclear Fusion **31** (1991) 1035

/2/ S. K. Erents, et al., Nuclear Fusion **28** (1988) 1209

/3/ P.C. Stangeby, G.M McCracken, Nuclear Fusion **7** (1990)

/4/ H. Pacher, et al.; 1992 PSI Conference, paper A:34; J. Nucl. Mat., this issue

/5/ K. McCormick, et al., J. Nucl. Mater. **176&177** (1990) 89

/6/ K. McCormick, Z.A. Pietrzyk, et al., J. Nucl. Mater. **162&164** (1989) 264

/7/ H. Murmann, et al., in Proc. 13th EPS Conf. on Controlled Fusion and Plasma Physics, Schliersee **10c** (1986) 216

/8/ K.-H. Steuer, H. Röhr and B. Kurzan, Rev. Sci. Instrum. **61** (1990) 3084

/9/ W. Schneider, J. Neuhauser, G. Haas, K. McCormick, N. Tsois, R. Wunderlich, Contrib. Plasma Phys. **28** (1988) 387

/10/ R. Schneider, et al.; 1992 PSI Conference, paper C:20; J. Nucl. Mat., this issue

/11/ J. Neuhauser, et al., Plasma Physics and Controlled Fusion **31** (1989) 1551

/12/ O. Gehre, K.W. Gentle, in Proc. 18th EPS Conf. on Controlled Fusion and Plasma Physics, Berlin **15C** (1991) 97

/13/ A. Stäbler, et al., "Density Limit Investigations on ASDEX", submitted to Nuclear Fusion

/14/ K. Itami, et al., J. Nucl. Mater. **176&177** (1990) 504

/15/ K. Itami, et al.; 1992 PSI Conference "Characteristics of Divertor Plasma and Scrape-off Layer in JT-60U"; J. Nucl. Mat., this issue

**Figure Captions**

Fig.1 SOL density profiles for an $I_p$ scan. $\bar{n}_e \sim 2.5x10^{13}$ cm$^{-3}$, $B_t = 2.2T$, $q_a = 2.6, 4.35, 5.5, 7.34$. $R-R_s$ is the distance from the separatrix.

Fig.2 SOL exponential falloff lengths for data set **A**. Only a subset ($\bar{n}_e \leq 3.1x10^{13}$ cm$^{-3}$) is considered in order to allow the intermingled $H^+$ points to remain visible.

Fig.3 Comparison of the $Z_{eff}$(min) necessary to maintain collisionality in the SOL with $Z_{eff}(0)$ measured in the plasma center for a subset of data set **A** ($I_p = 350$kA).

Fig 4 $\lambda_n$ regression fits for the data sets **A**(top), **B**(middle) and **C**(bottom). The fit for **A** is restricted to $T_s > 40$eV. Note that $\lambda_n$ varies only over the range 1.6-2.5cm, in spite of the wide variety of conditions.

Fig.5 The diffusion coefficient $D_p$ vs. $T_s$ for the data sets **A** (only $D^+$), **B**, and **C**, derived using eq.(3) under the premise of no impurities.

Fig.6 $D_p$ vs. $D_{Bohm} = T_s/16B_t$ for data sets **A**, **B**, and **C**.

Fig.7 Power flux profiles in the upper, outer divertor measured with a reciprocating langmuir probe for a subset of data set (**D**). $\bar{n}_e = 5\text{-}6x10^{13}$ cm$^{-3}$. The separatrix is situated slightly to the left of the $q_{||}$ peak. The steep gradient on the left hand side is in the private flux region. The double traces correspond to the inwards and outwards probe movement during one radial scan.

Fig.8 Equivalent power flux channel widths $\Delta_p$ vs. divertor temperature $T_{ed}$ for data sets **D**(top) ($He^{2+}$) and **E**(middle) ($D^+$).$T_{ed}$ is varied through an OH $q_a$-scan in **D**, and an $n_e$-, $P_{NI}$ -scan in **E**. The bottom plot shows the regression fit for the combined two sets.

Table 1: Parametrical dependence of $\lambda_n$. Exponents are given for regression fits of the form: const.x $A^{\alpha}T_s^{\beta}q_a^{\gamma}P_{sol}^{\delta}$. $\lambda_n$[cm], A[ion mass], $T_s$[eV], $P_{sol}$[MW]. The standard error is in the adjacent column. R is the regression coefficient. Blank spaces indicate that the parameter was not included in the regression.

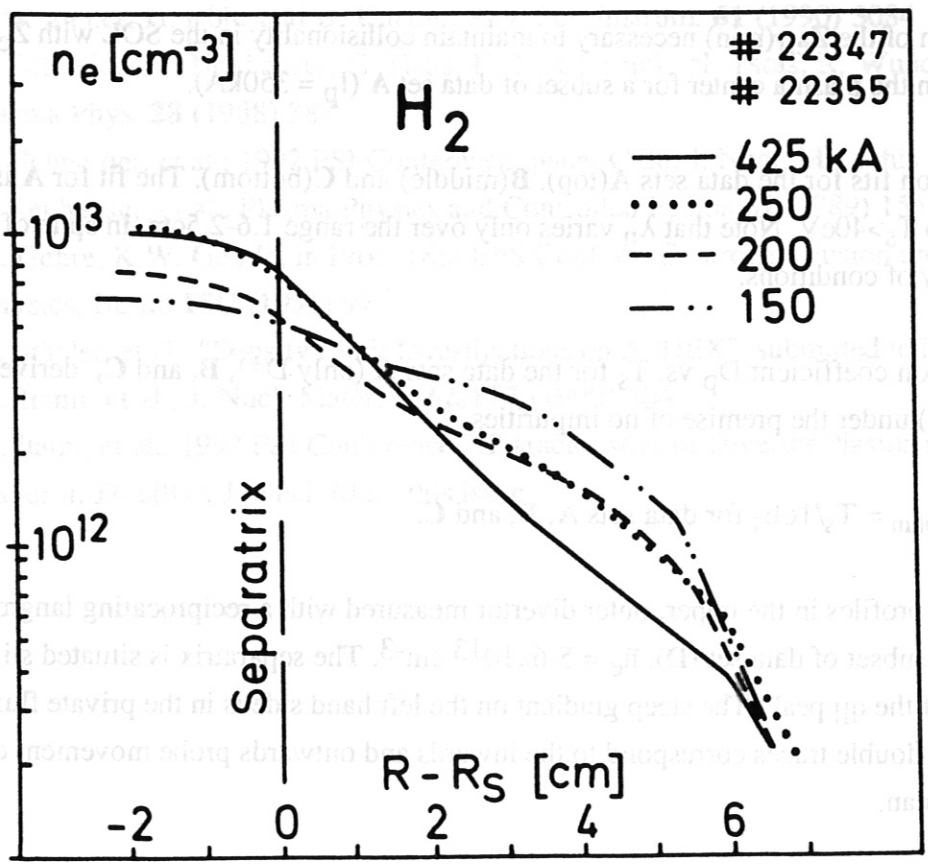


Fig.1

*K. McCormick-10th PSI, Monterey*

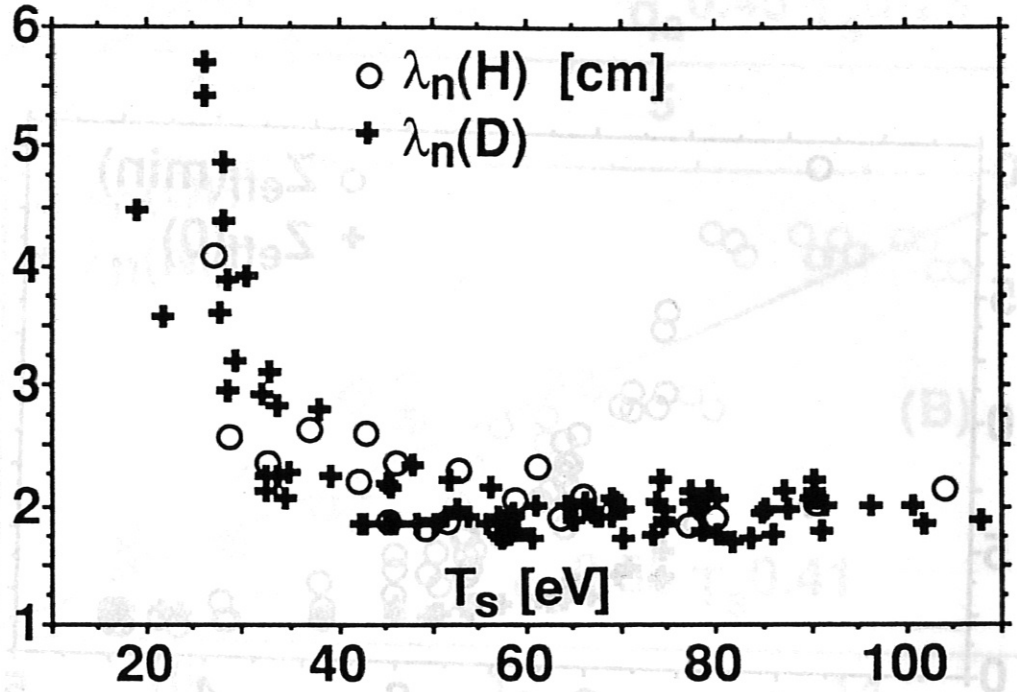


**Fig.2**

*K. McCormick-10th PSI, Monterey*

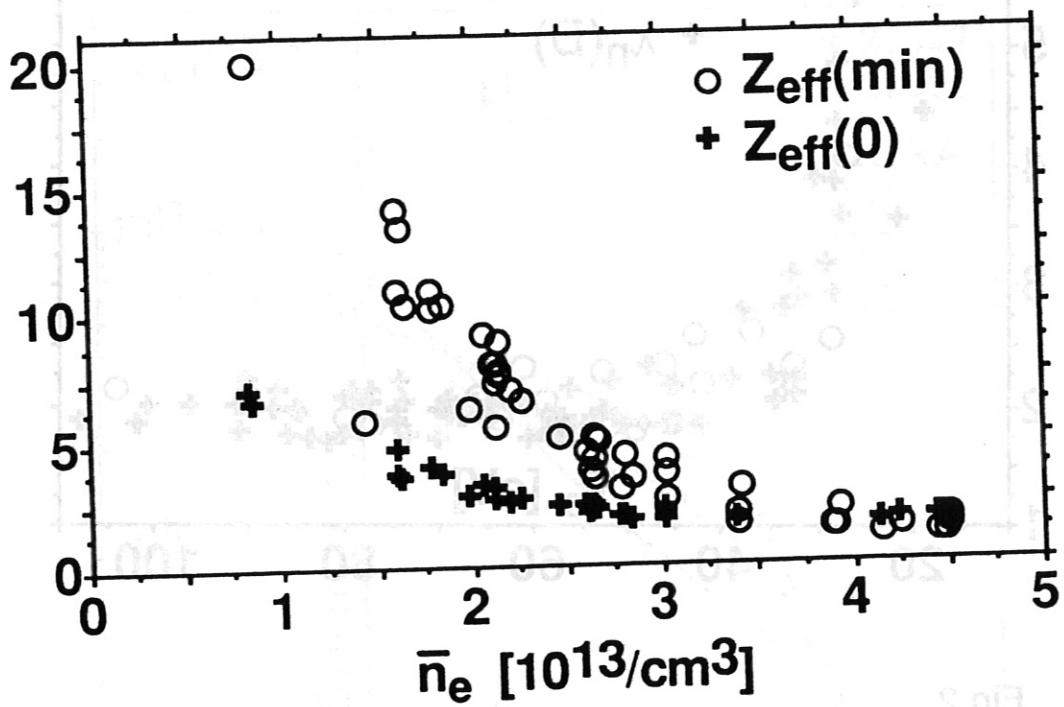


**Fig.3**

*K. McCormick-10th PSI, Monterey*

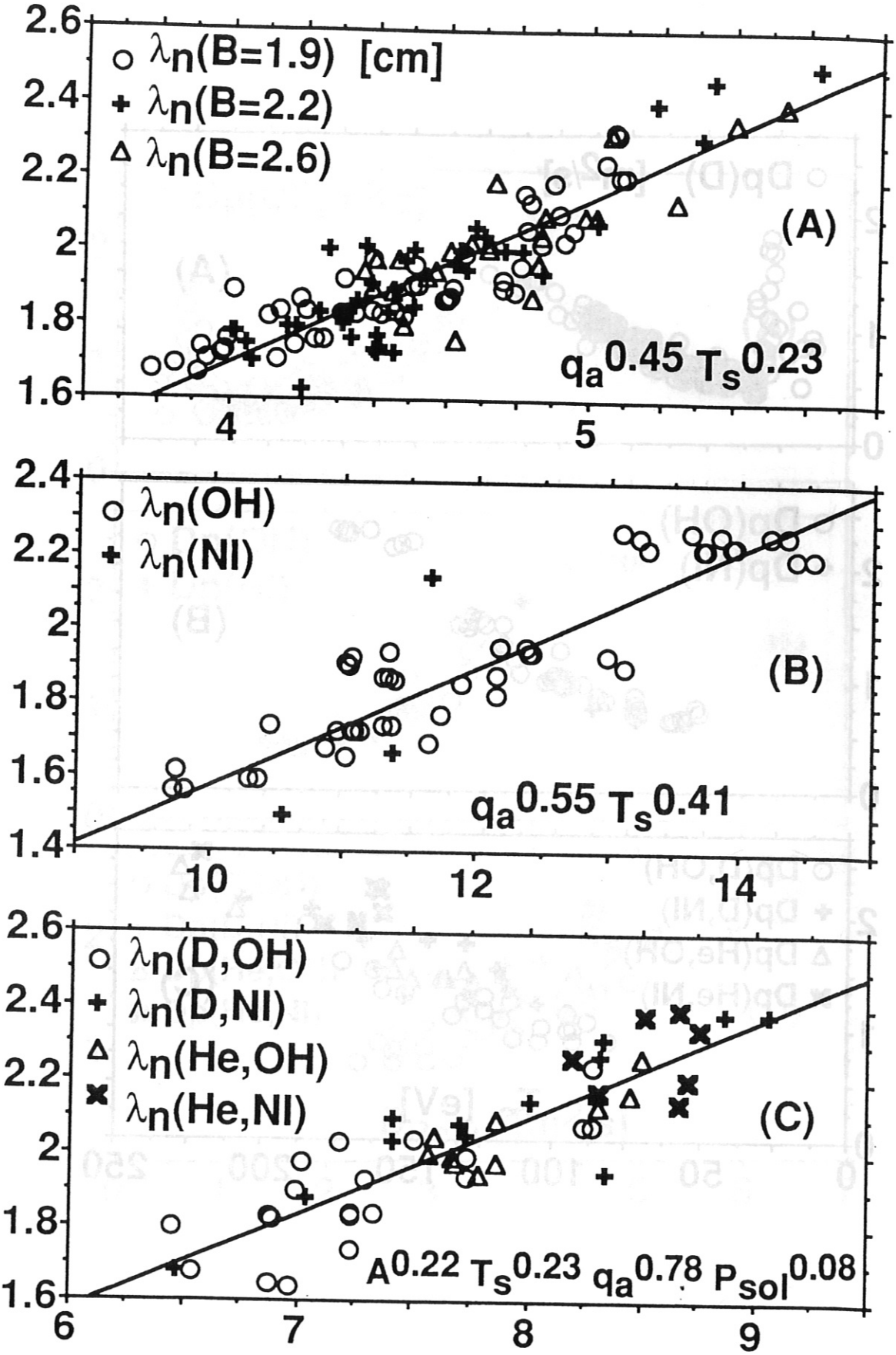


Fig.4

*K. McCormick-10th PSI, Monterey*

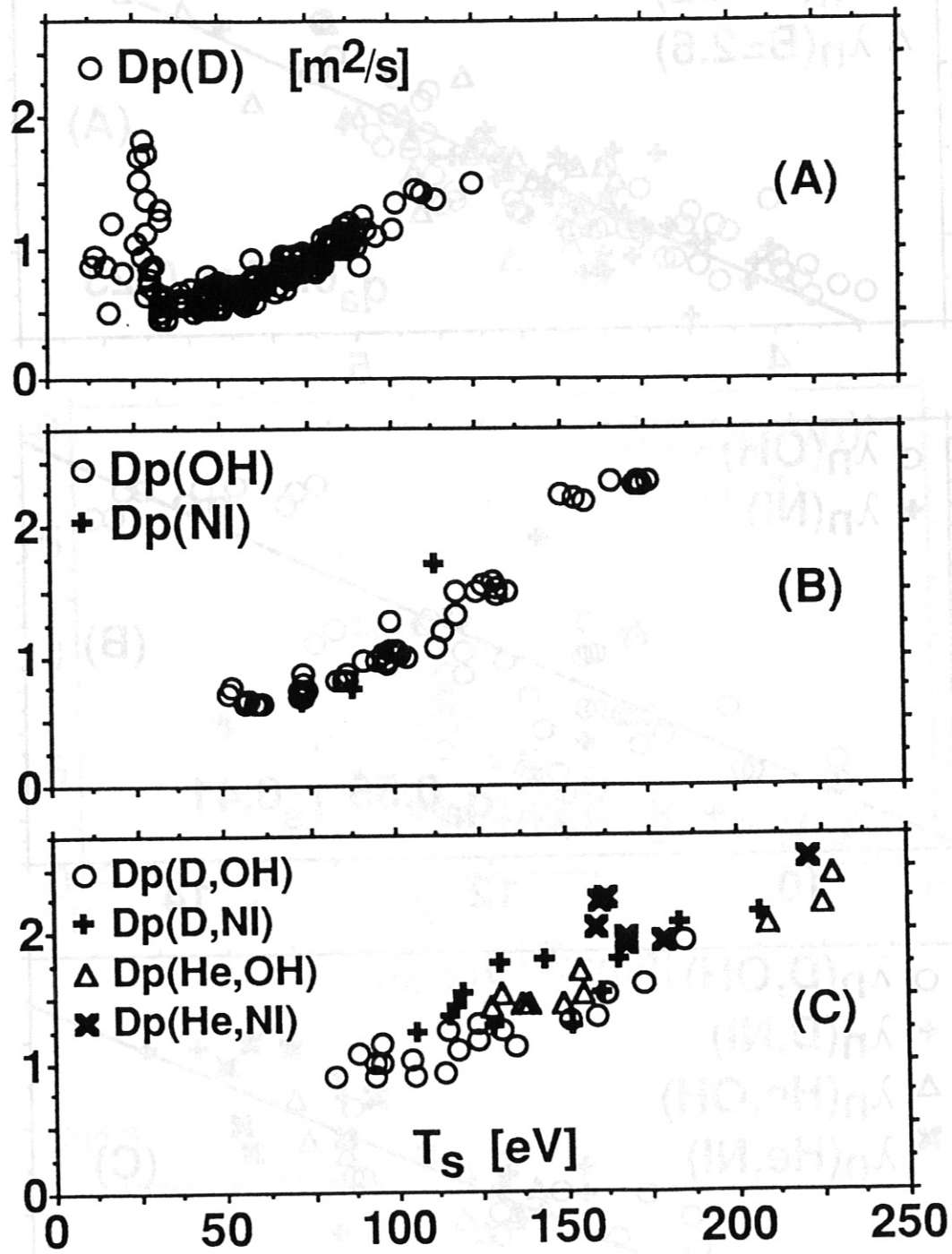


Fig.5

*K. McCormick-10th PSI, Monterey*

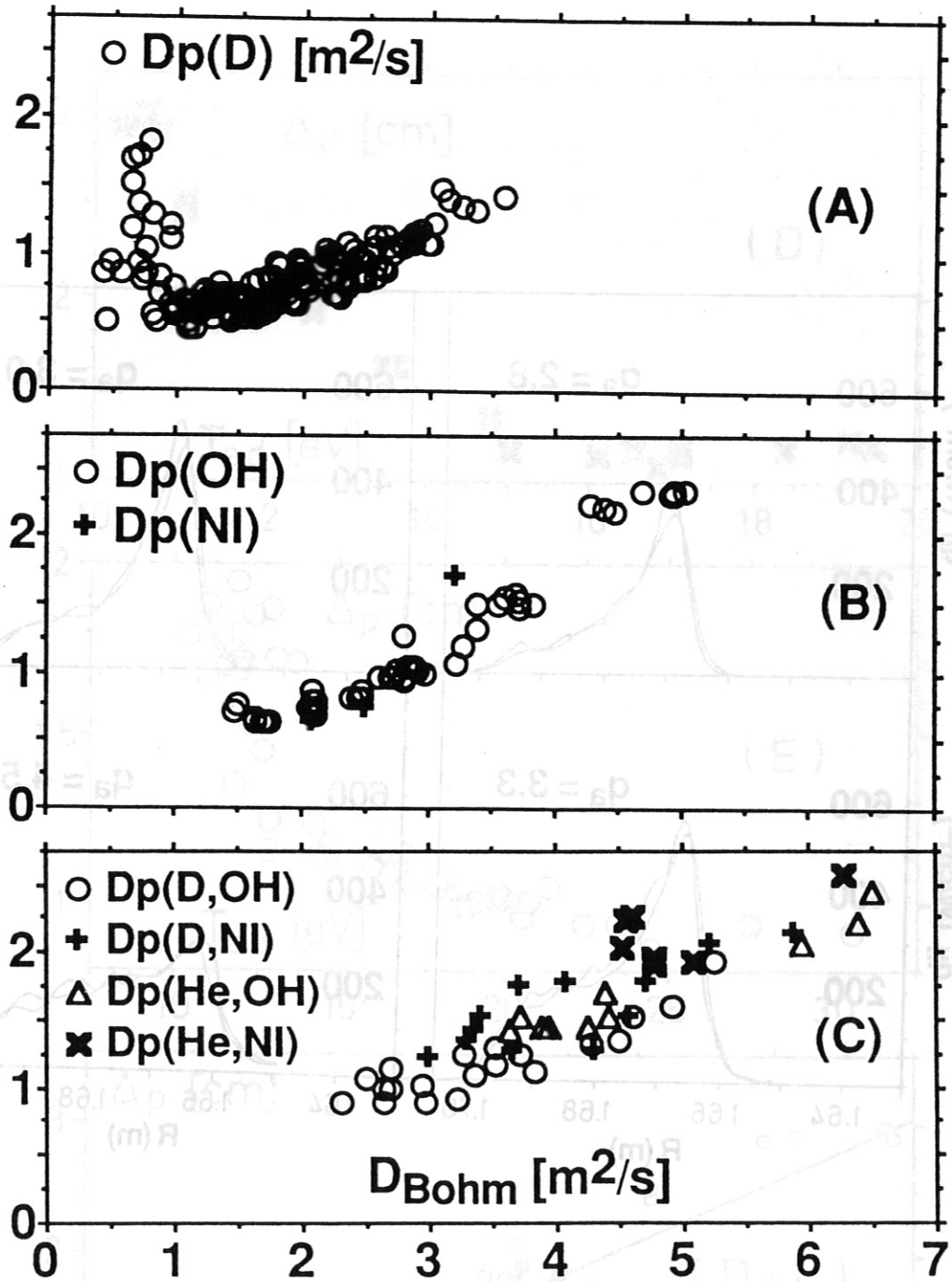


Fig.6

*K. McCormick-10th PSI, Monterey*

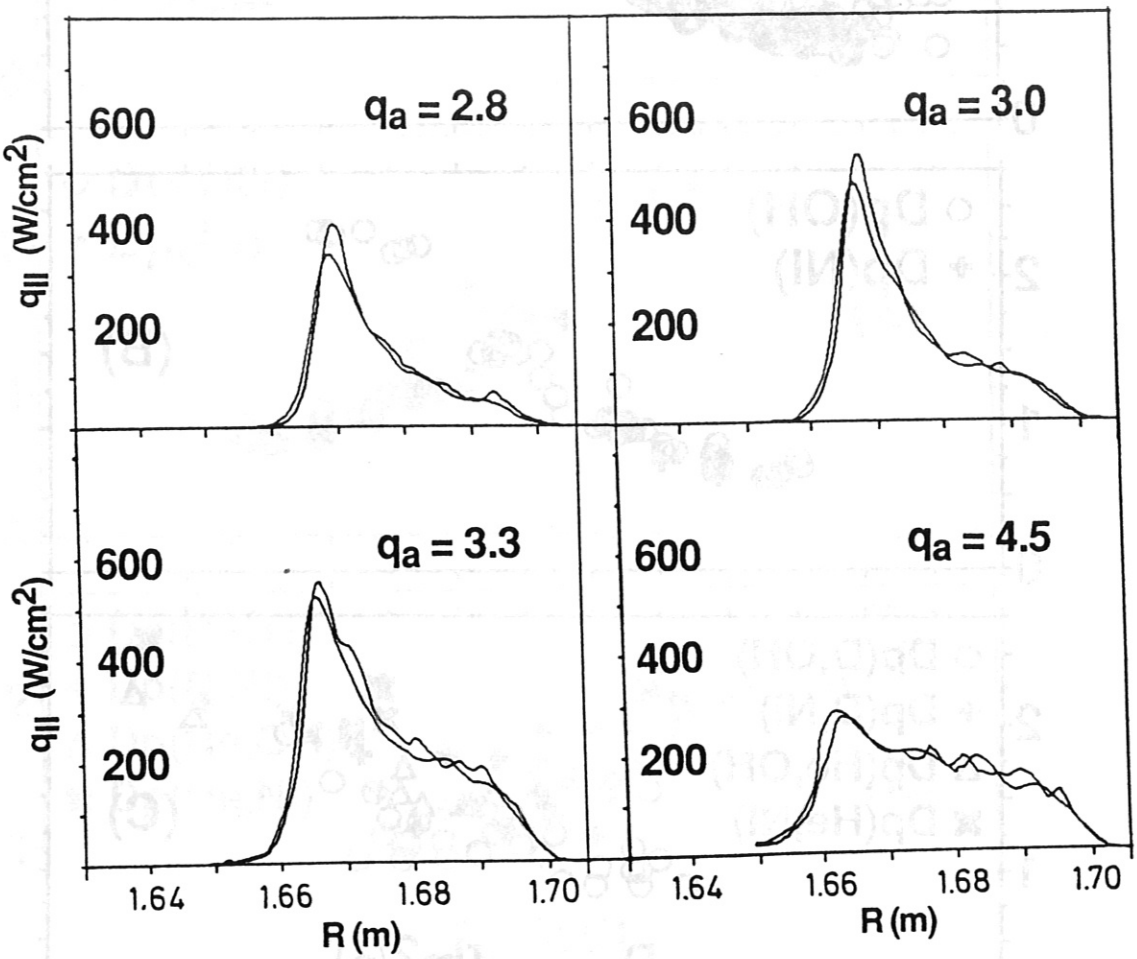


Fig.7

*K. McCormick-10th PSI, Monterey*

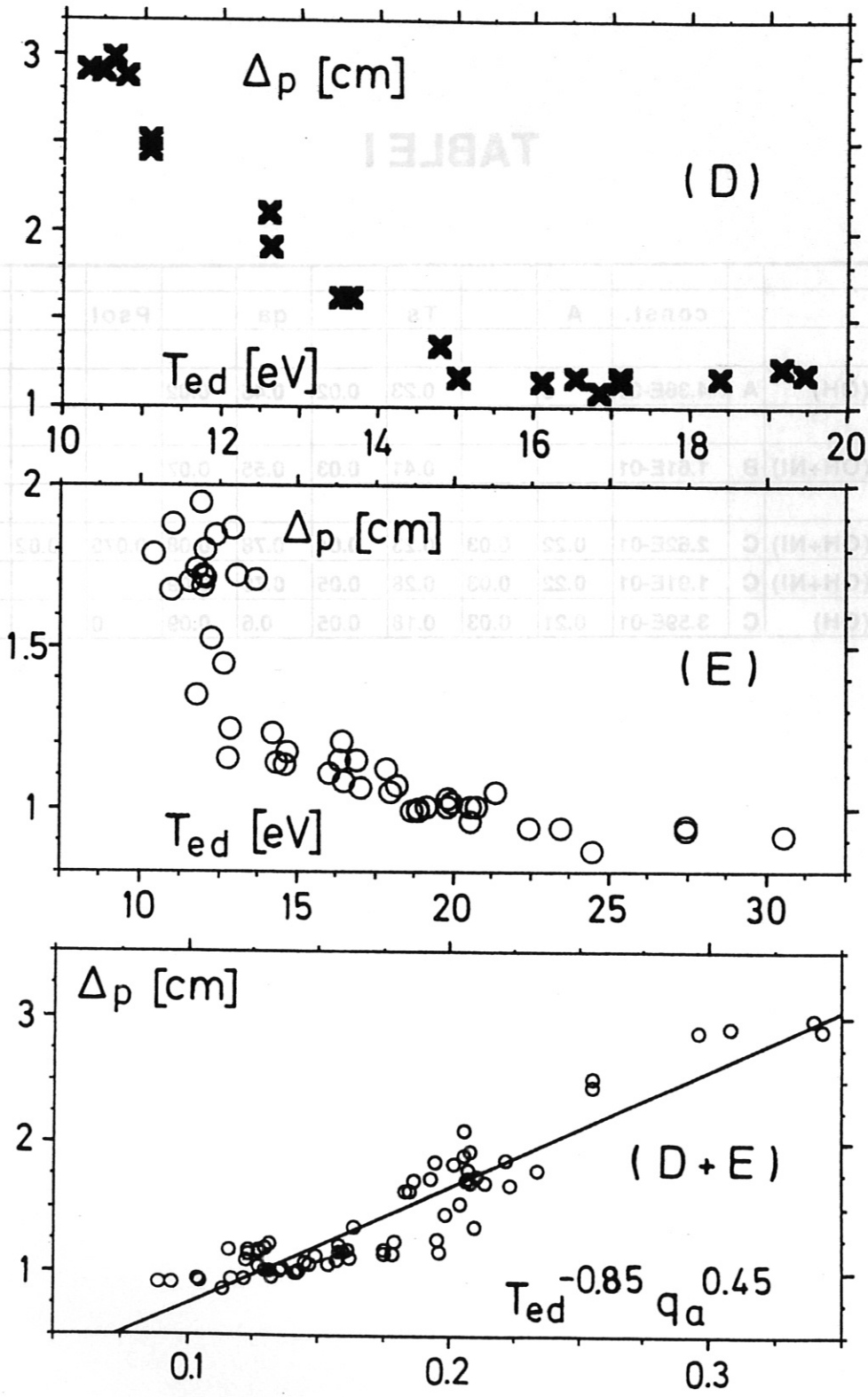


Fig.8

# TABLE I

| | | const. | A | | Ts | | qa | | Psol | | R |
|---|---|---|---|---|---|---|---|---|---|---|---|
| lam(OH) | A | 4.36E-01 | 0 | | 0.23 | 0.02 | 0.45 | 0.02 | | | 0.88 |
| lam(OH+NI) | B | 1.61E-01 | | | 0.41 | 0.03 | 0.55 | 0.07 | | | 0.91 |
| lam(OH+NI) | C | 2.62E-01 | 0.22 | 0.03 | 0.23 | 0.04 | 0.78 | 0.08 | 0.075 | 0.02 | 0.89 |
| lam(OH+NI) | C | 1.91E-01 | 0.22 | 0.03 | 0.28 | 0.05 | 0.76 | 0.09 | | | 0.81 |
| lam(OH) | C | 3.59E-01 | 0.21 | 0.03 | 0.18 | 0.05 | 0.6 | 0.09 | 0 | | 0.86 |